Doctorate in Science and Technology of Chemistry and Materials
Curriculum: Drug Discovery and Nanobiotechnologies

XXXIII Cycle
Università degli studi Genova

Colorimetric nanodiagnostics for Point-Of-Care applications: detection of salivary biomarkers and environmental contaminants

---

Supervisors:
Dr. Pier Paolo Pompa
Prof. Marco Grotti

Ph.D. Student:
Donati Paolo

Contents

Abstract

Nanomaterials offer many unique opportunities for the development of effective and rapid point-of-care (POC) devices to be exploited in many fields, including early diagnosis, health monitoring, and pollutant detection. In particular, gold nanoparticles (AuNPs) exhibit tuneable catalytic and plasmonic properties, which are key enabling tools to design and develop innovative detection schemes in several sensing applications. The aim of this PhD project was the development of AuNPs-based colorimetric POCs to detect heavy metal ion contaminations and specific biomarkers in non-invasive biological fluids. First, we developed a novel strategy that exploits the combination of the plasmonic and catalytic properties of AuNPs to achieve an ultrafast (1 min) and sensitive colorimetric sensor for highly toxic methyl mercury. Taking advantage of the AuNP nanocatalyst to promote the rapid reduction of methyl mercury with nucleation on the particle surface and consequent aggregation-induced plasmonic shift, we were able to detect by naked-eye mercury contaminations as low as 20 ppb, which is relevant for food contaminations or biological fluid assessment. Moreover, an innovative and versatile platform, based on multibranched AuNPs, was developed for the detection of salivary biomarkers. Coupling etching and growing reactions in a reshaping process onto the nanostars surface, we created a customizable platform with boosted colour change readout for fast detection of salivary glucose at low concentrations. The nanosensor performance was validated on samples from patients with diabetes, proving its potential as a novel non-invasive tool for frequent monitoring of glycaemia. As side project we also investigated the platinum nanoparticles enzymatic activity in a colorimetric sensor for mercury contamination monitoring in water sources.

1 Introduction

1.1 In vitro diagnostics

Over last years, laboratory testing has been subjected to a continuous paradigm evolution to meet the increasing demand for high-qualitative healthcare and patient self-advocacy. The diagnostic concept is evolving rapidly, drawing the attention of both research and industry. We are witnessing the rapid development of next-generation in vitro diagnostic (IVD) devices, as result of an increasing competition between companies dragged by the rapid expansion of the global market (see **Figure 1.1**). The Food and Drug Administration (FDA) defined IVD products as "[...] those reagents, instruments, and systems intended for use in diagnosis of disease or other conditions, including a determination of the state of health, in order to cure, mitigate, treat, or prevent disease or its sequelae"[1]. Government agencies like FDA, or commissions, such as the European Commission (EC), drafted legislation to regulate the market, and, more importantly, to define and identify these new tools as a quality and safety standard for in vitro diagnostic medical devices[2].

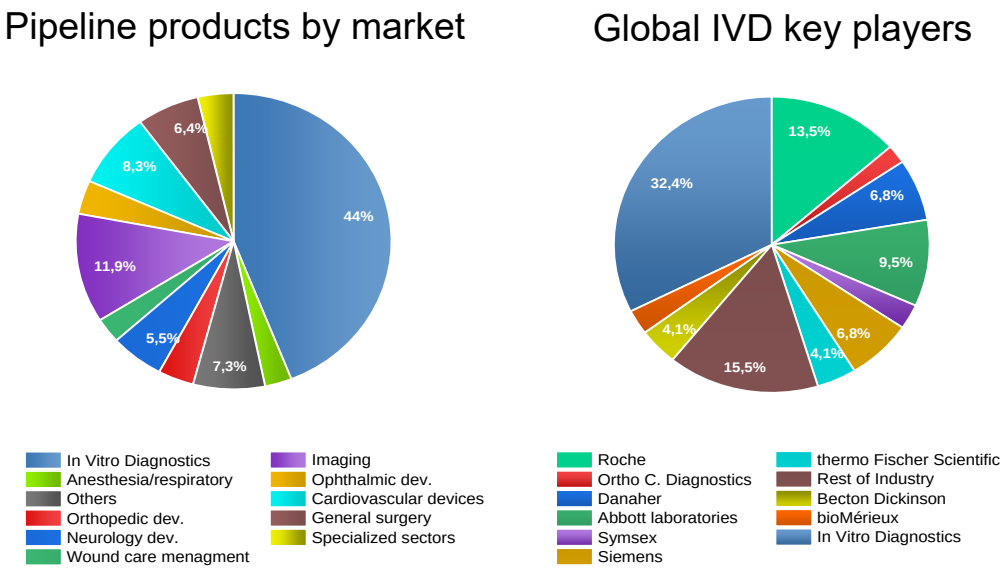

Figure 1.1 Pipeline products (left) and global IVD industry-key players (right) (ref. 3).

In vitro diagnostics provides useful solutions for analytical grade, qualitative and quantitative assessment of analytes in biological fluids or other complex samples. The detection of physio- and pathological biomarkers, like small molecules, steroids, and oligonucleotides, as well as food and environmental contaminants is the main purpose of IVD applications.

Traditional IVD techniques, generally, require several operational steps, such as sample collection, delivery and treatment, target extraction and purification, which lead up the detection step. All these laborious and time-consuming procedures often necessitate specialized laboratories, costly reagents and instrumentations, and skilled personnel. Moreover, in certain circumstances, a self-sampling is required, thus compelling unprepared users to invasive and painful sampling procedures. Due to these drawbacks, traditional diagnostics is becoming sub-optional.

1.2 From IVDs to Point-Of-Care diagnostics

The ageing population and the increasing incidence of chronic diseases necessitate high-quality healthcare, rapid and easy-to-use original solutions. Moreover, as recent events connected to pandemia have highlighted, the access to treatment and services has proved to be more and more complicated. Most of the people have experienced a challenged healthcare system with overcrowded hospital and long waiting time. Thus, early clinical diagnostics is becoming an active part of medical evaluations and disease management[3] from risk assessment to disease monitoring (see **Figure 1.2)**. In this framework, point-of-care (POC) testing plays a key role to deliver care to patients, outside the hospital.

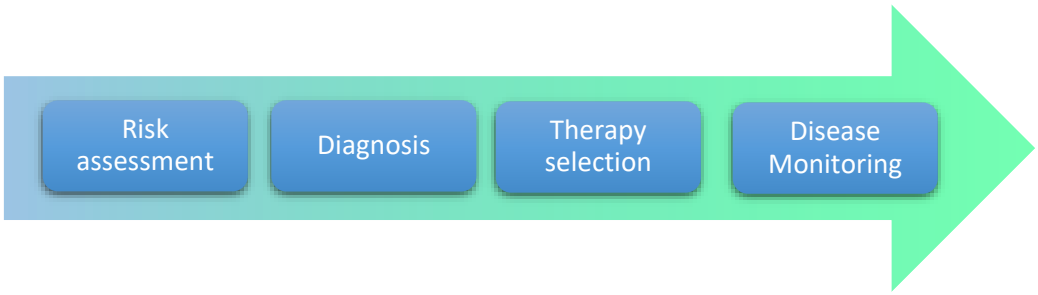

Figure 1.2 The application of in vitro diagnostics in the delivery of healthcare (ref. 4).

Accurate and fast results can considerably reduce the preanalytical treatment errors, enabling rapid triage, allowing clinicians to gain more control on medical decisions with a remarkable improvement of patients' quality of life[4], and also preventing critical patient disability and death[5,6]. Indeed, POC testing provide lab-quality outcomes within minutes, accelerating clinical decisions. It has been calculated that POC diagnosis could lead to a reduction of 44% in hospitalization length and a consequent decrease of related risk of both adverse complications and healthcare associated infections[7,8]. In addition, it has been estimated a total laboratory cost savings of 8-20% for those organizations that implement POC testing[9]. Waiting time can be reduced by 46 minutes, saving €148 per patient[10,11]. All these benefits are promoting the POC testing deployment. Indeed, in 2019, the global market size of POCT was evaluated for $28.5 billion and it was expected to reach USD 46.7 billion by 2024 (CAGR of 10.4%)[12,13]. Beyond bedside benefits, POCT shows several advantages when compared with traditional IVDs.

The World Health Organization (WHO) issued some guidelines for developing efficient POCT known as ASSURED that is the acronym for affordable, sensitive, specific, user-friendly, rapid/robust, equipment-free or minimal, and delivered to the greatest need[14]. POC devices can be defined as larger bench-top devices or small hand-held.

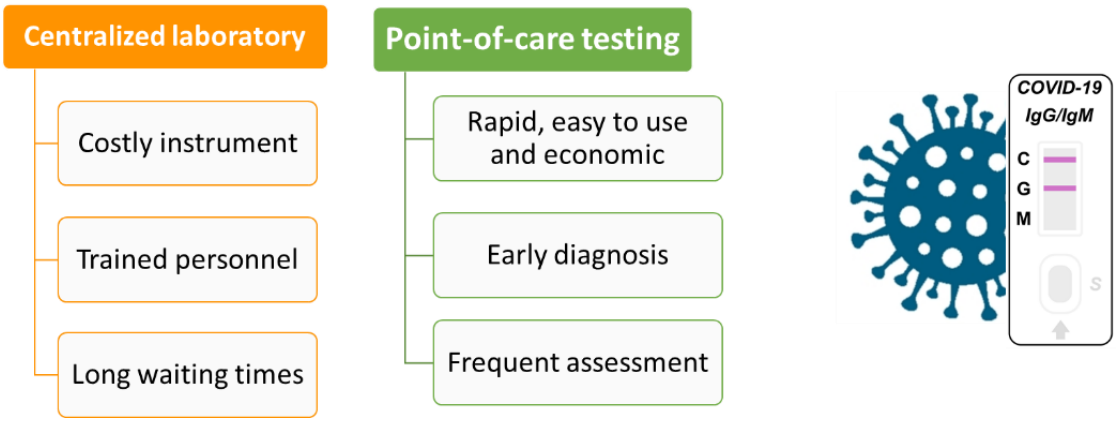

Figure 1.3 Comparison between centralized laboratory and POCT characteristics.

POC diagnostics does not require complex instrumentation or equipped rooms; it allows fast and in situ detection of biological/chemical contaminants or health state assessment anytime and anywhere, drastically facilitating the access to healthcare. Thus, POC testing offers an efficient tool for routine analysis and preliminary checks, accelerating the early diagnosis with a related notable improving of the quality of life (see **Figure 1.3**). Today, in a scenario of global pandemics, the value of a fast, effective POC testing for large-scale screening on the fight of virus spreading is undeniable. Alternative diagnostic methods are urgently required to alleviate the laboratory workload during SARS-CoV-2 outbreak[15,16].

POC-device portability is a distinctive feature, and it is closely related with the sensing strategy and relative device design adopted. Colorimetric visual detection-based strategies are the most exploited, since the test outcome consists in a colour change in terms of hue or saturation and does not need for any instrumentation to be recognised in both threshold and quantitative assessment. Nanomaterials offer a clear edge on the design of a new generation of effective POC devices, thanks to a variety of features exploitable to set up miniaturized, automated, colorimetric nanobiosensor. Nanotechnology is recently sustained by and combined with microfluids that provide different solutions for sample handling or reagent mixing, using microchannels and material science to manipulate from micro- to picolitres of solutions in a reduced space. Lateral flow devices (see **Figure 1.4**) represent a great example in which microfluidic principles

combined with immune/chemical assays technology and nanoplasmonic results in on-site platform capable of accurate results[17,18].

By virtue of its versatile nature, lateral flow assays (LFAs) are widely employed in a number of sectors from food and environmental testing to pharma and animal and plant health. Moreover, LFAs are recently implemented in multiplexing to detect simultaneously the presence of multiple food contaminants or to carry out the diagnosis of several significant biomarkers, useful in case of small sample volume availability[18,19].

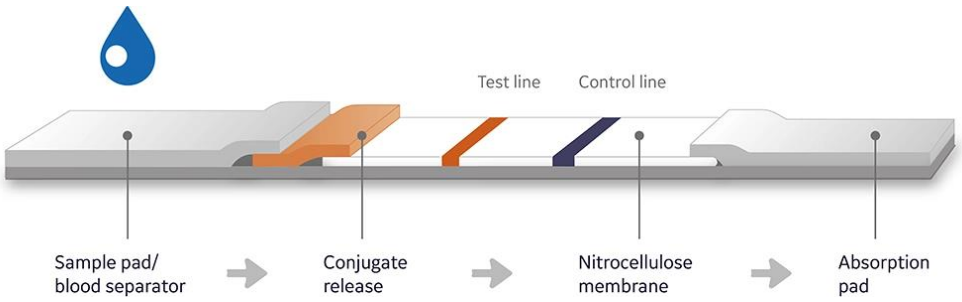

Figure 1.4 Typical lateral flow device for POC testing.

Simultaneously, the *mHealth* (abbreviation for mobile health) is rapidly gaining ground as a sub-segment of *eHealth*[20] (see **Figure 1.5**). Information and communication technologies (ICT) are revolutionizing the healthcare system transforming common electronic devices, such as smartphones, into medical devices to acquire, store and analyse data. The main *mHealth* advantages include: remote data collection and monitoring for improved diagnosis and patients follow up, disease and epidemic outbreak tracking, effective data driven approach to personalized medicine[21–23]. Several companies recently market products using smartphones as included component or provided by the final user.

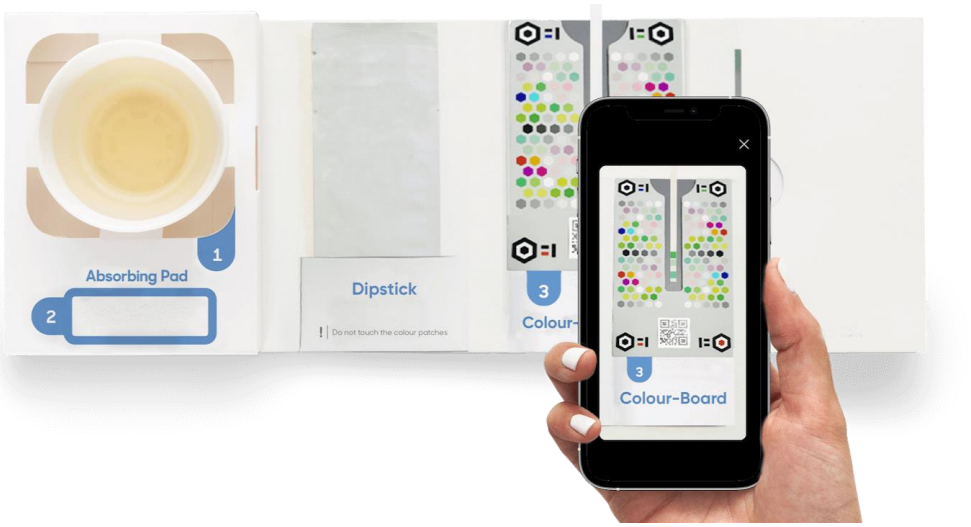

Figure 1.5 Example of mHealth smartphone based on colorimetric detection.

1.3 Nanobiosensors

A biosensor is a full-fledged analytical measurement system specifically designed for the assessment of biochemicals as oligonucleotides, proteins or other biomarkers. Such analytes are recognized by a bioreceptor, which is a biological system (such as antibody, cell parts, enzymes, oligonucleotide) that selectively interacts with the target, thus resulting in a biological signalling. Afterwards, the transducer element converts the bioanalyte-receptor interaction into a measurable electrochemical, optical, pyroelectric, or piezoelectric signal. Such signal is then processed and/or amplified by an amplifier/detector[24,25] (see **Figure 1.6**). An example of this system is the Bio-FET, a biosensor based on MOSFET (metal-oxide-semiconductor field-effect transistor, or MOS transistor) that is widely applied to assess various biochemicals and environmental parameters[26].

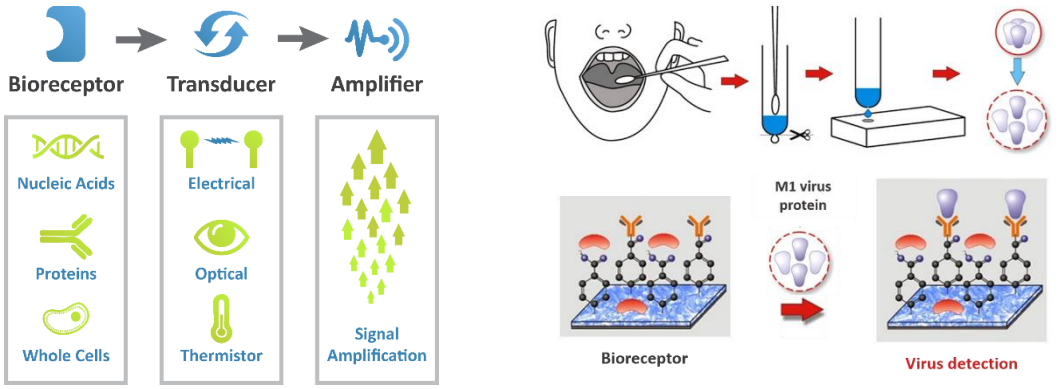

Figure 1.6 Nanobiensor operation principle (left), and an example of application of viral protein detection (ref. 27).

A biosensor must meet some important requirements that include sensitivity, selectivity, reproducibility and stability. The biosensor selectivity is the capacity to recognize specific targets in a complex sample matrix rich in interfering components. The sensitivity refers to the ability of the biosensor to produce a signal for small variations of analyte concentration. The reproducibility is the property to generate the same response to replicated experimental setup, and it is closely related to the stability that quantifies how much the environment perturbations, such as variations of temperature and/or pH, can affect the result. About the outcome, the indicators that define the analytical performance of a biosensor are the Limit-Of-Detection (LOD), Limit-Of-Quantification (LOQ) and the Limit-Of-blank (LOB). The LOB describes the highest noise (apparent analyte concentration) expected to be found in the replicated blank samples. The LOD indicates the minimum threshold value of analyte concentration detectable, and the LOQ "is the highest *apparent* analyte concentration expected to be found when replicates of a blank sample containing no analyte are tested."[28]. These are the main features and performance indicators to define an impactful and effective biosensor.

1.4 Nanotechnology for biosensing applications

The early diagnosis and the health condition monitoring, as well as the environmental pollutants detection are attracting growing attention from both industry and research. Although there is still a need for suitable tools to be applied in such fields, a new generation of biosensors have been designed for POC testing[29], due to the gained knowledge and expertise in the field of nanotechnologies and to the possibility to synthesize smart nanomaterials with unique properties. Indeed, nanomaterial-based sensors have been shown to be a suitable choice for instrument-free and on-site diagnostic applications[30,31].

European Commission defines a nanomaterial as "a natural, incidental or manufactured material containing particles, in an unbound state or as an aggregate or as an agglomerate and where, for 50 % or more of the particles in the number size distribution, one or more external dimensions is in the size range 1 nm - 100 nm"[32] (see **Figure 1.7**). At the nanometric size, the particles show peculiar physical and chemical behaviours owed to the predominant quantum confinement phenomena and surface effects[33,34].

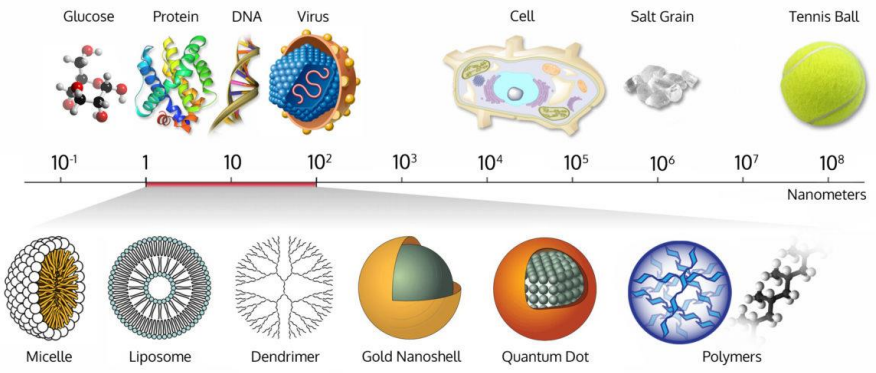

Figure 1.7 Length scale of the biological components and the nanomaterials (comparison).

The quantum confinement effect refers to the energy levels and relative electronic distribution in the nanomaterial. At this size, the material relative band gap decreases while energy levels become discrete, unlike the bulk dimensions of the

same material[35]. The electron mobility is reduced at certain discontinuous energy states, phenomenon known as "quantum confinement"[36]. Therefore, the band gap shrinks or widens, following the nanoparticles size, with a relative increase or decrease of energy levels density (see **Figure 1.8**). Such renewed electronic configuration, typical of the nano-size, lends new properties to the particles as the way of interaction with light radiation, resulting in size and shape-dependent absorption and luminescence phenomena[37,38].

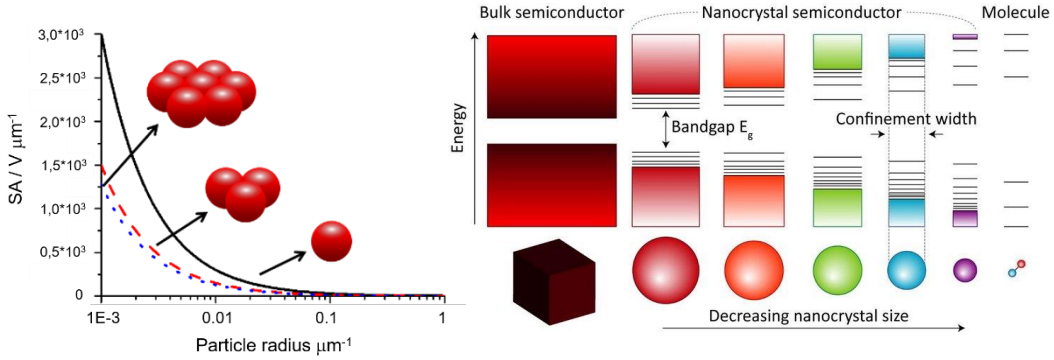

Figure 1.8 On the left graph of size to volume ratio correlation, on the right energy band gap in the nanocrystal semiconductor.

Another important parameter influencing the nanomaterial surface properties is the high surface-to-volume ratio, which increases with the lowering of size[39] (see **Figure 1.8**). Considering a generic sphere of radius *r*, its surface scale with the square of *r* while its volume with the cube of *r,* therefore, the ratio increases the particles size reduction. Paired the mass (in terms of the number of atoms), the exposed surface grows extraordinarily. Even the surface reactivity is conditionated by the size. Given that the surface atoms are characterized by lower coordination number, resulting less stable than the more coordinated interior ones, the nanosized materials show a high surface energy[40]. The latest developments in biosensor design have benefited from the size-dependent nanostructures properties to improve both the biorecognition interaction and the transducing reaction. On one hand, the high surface-to-volume ratio allows high reactivity to functionalization of the nanomaterial surface with bioreceptors, thus increasing

the specific target recognition reactions[41,42]. On the other, the catalytic properties of nanomaterials and their interaction with light can enhance the transducing process, enabling sensitive and colorimetric readout. Several nanomaterials have been exploited in hybrid nanosensors like carbon nanotubes, magnetic nanoparticles, silicon nanowires and nanostructured metallic particles (such as silver, gold, platinum, palladium and iron oxide). In particular, metallic nanoparticles exhibited high potentiality in several detection mechanisms[43]. These nanomaterials can be easily obtained following different chemical methodologies that enable an accurate control of size- and shape-dependent optical, electrical and catalytic properties[44–46].

1.5 Gold Nanoparticles POC Applications

Among the metal nanomaterials, AuNPs present a series of peculiar features, which will be discussed in detail in the following paragraph, that make them particularly suitable for the development of colorimetric methods for POC applications in several fields, from environmental control to healthcare.

1.5.1 Environmental pollutant assessment

Most of the heavy metal ions are known to be highly toxic and in some cases carcinogens, and are considered as environmental health hazards to the extent of being ranked in the hazardous substances top ten[47,48]. In particular, mercury and organic mercury pollution is a global health threat given its well-documented toxic effect on living organisms and its widespread presence in the environment. The main sources of mercury contamination are coal power plants and metal mining that release more than one thousand metric tons per year[49]. Following this anthropogenic high emission, mercury is highly present in seawater and in soil, accumulate in aquatic species and enter the human food chain[50]. In the environment, mercury further reacts forming methylmercury through three

different ways, i.e. abiotic methylation, methylation by microorganism and photo methylation[51](see **Figure 1.9**). Once ingested in the human gastrointestinal system, mercury and methylmercury (CH_3Hg^+) get adsorbed and have a half-life of 70 days.

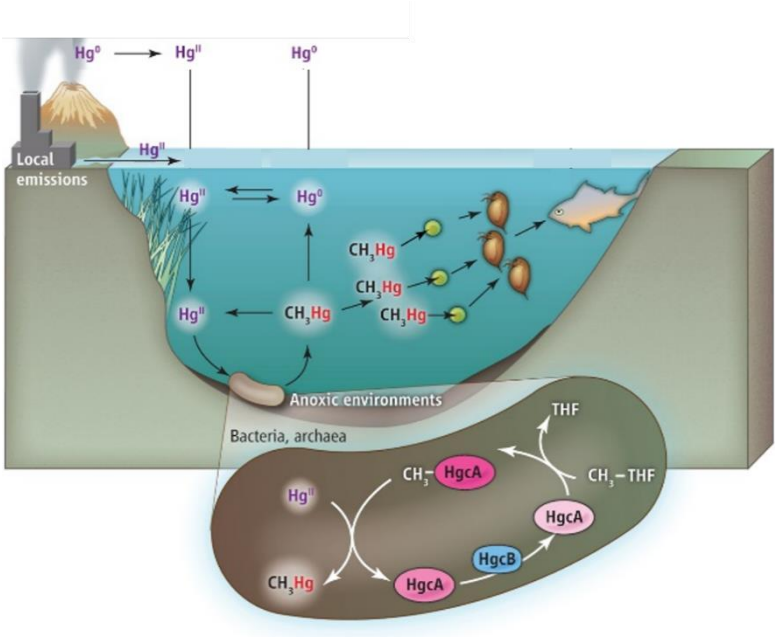

Figure 1.9 Mercury is methylated in anoxic environments by microorganisms (illustration in the inset). The toxic methylmercury accumulates in aquatic species (bioaccumulation), and its concentrations increase with each trophic level (biomagnification) (ref. 51).

CH_3Hg^+ is known to be much more toxic than inorganic one (Hg^{2+}), as, due to its reactivity with the sulfhydryl group, it forms a glutathione conjugate that reaches different cell biochemical mechanism, causing DNA toxicity as a consequence of increased global and gene-specific methylation. Moreover, it can pass the blood-brain barrier thanks to its lipophilicity and, there, CH_3Hg^+ strongly inhibits astrocytic glutamate uptake. CH_3Hg^+ causes mitochondrial dysfunction and activation of cell death pathways, overactivating (NMDA) receptors, and, thus, increasing the Ca^{2+} influx into postsynaptic neurons. In addition, CH_3Hg^+ determines elevated ROS species generation (which increases the oxidative stress) and lipid peroxidation and, hence, the impairment of the activity of neurotransmitter and neuromodulator receptors[52–55](see **Figure 1.10**). The systemic poisoning leads to hypertension, pulmonary toxicity and nephrotoxicity[56].

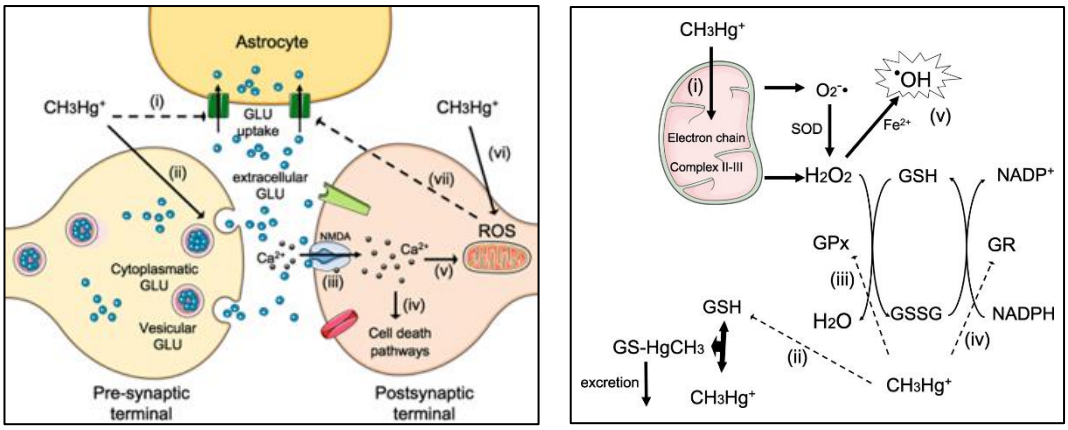

Figure 1.10 On the left the CH_3Hg^+ induced oxidative stress and Ca^{2+} and glutamate dishonesties, on the right CH_3Hg^+ effects on the GSH antioxidant system (ref. 55).

In the human body, the major source of both organic and inorganic mercury is the consumption of contaminated food, in particular shellfish and large-size fish, like tuna and swordfish[57–61]. Considering the high risks involved with mercury contaminated food consumption, American and European authorities have set out rigid limits for methyl mercury concentration in food and water[62]. FAO and WHO organizations have established that the maximum levels of CH_3Hg^+ allowed in fish could not exceed 1.0 μg/g for predatory fish and 0.5 μg/g for other fishery products, calculated on the basis of wet weight[63,64]. To date, the detection and quantification of mercury species (Hg^{2+}, CH_3Hg^+) are performed by a plethora of complex and costly laboratory-based methods[65-69]. Therefore, there is a strong need for portable and easy-to-use devices for the simple and rapid home testing of these threating pollutants. Harvesting the potential recently opened by the application of nanoparticles to analytic issues, several colorimetric nanosensors have been recently proposed for naked-eye detection of mercury[70,71]. However, the sensitivity and reliability are still a major challenge for routine monitoring application. Moreover, only few reports deal with the detection of organic mercury[72,73], which is the most abundant and dangerous species in fish flesh.

1.5.2 Early diagnostic and health conditions monitoring

The National Institutes of Health (NIH) defines a biomarker as an "objectively measured and evaluated indicator of normal biologic processes, pathogenic processes, or pharmacologic responses to therapeutic intervention"[74]. Biomarkers are biological molecules able to supply information concerning the physiologic state of a living organism. Variations of biomarker concentration, structure, and function can identify a progression or regression of a specific disorder or demonstrate how the body responds to it. Evaluation and profiling of a biomarker is a useful tool to the health conditions monitoring, risk assessment and early diagnostic[75].

1.6 Saliva as diagnostic fluid

Nowadays, different biological fluids like blood (gold standard), serum, urine, cerebrospinal fluid, sperm etc. are used as diagnostic tools, but they need particular precautions and skilled personnel to be collected with few complications[76,77]. Besides, traditional biological fluids (e.g. blood) require invasive sampling techniques like painful finger pricking that entail evident discomfort and health risks, such as infections and viral transmission. Hence, there is an increasing attention towards non-invasive sampling. In this context, the use of saliva as diagnostic fluid is becoming a clinical reality[75,78,79].

Saliva is a colourless, pseudo acidic, muco-serous exocrine secreted fluid. Whole saliva is a mixture from parotid (20–25% of secretion), submandibular (70–75% of secretion), sublingual, tubarial and minor glands. Main constituents include water (98%), mucopolysaccharides and glycoproteins, electrolytes, white blood cells, epithelial cells (DNA vehicle), proteins and enzymes like amylase lipase and antimicrobial enzyme. The daily production of saliva ranges from 0.5 to 1.5 litres,

its normal flow rate is about 0.3 mL/min and it increases up to 7 mL/min when stimulated. The resting pH varies from 6.2 to 7.4, and this value changes with a meal (it increases within 5 minutes after the intake of food, and returns to basal levels approximately 15 minutes after food consumption)[75,80,81].

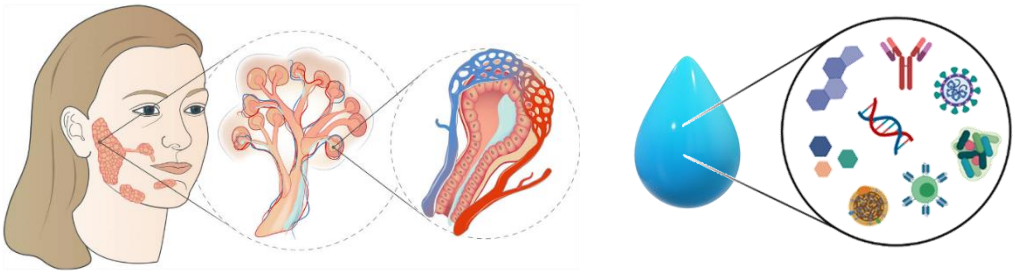

Figure 1.11 On the left, salivary glands location; in magnified, view of the duct and the acinar structures. On the right, representative biomarkers of salivary fluids.

Saliva contains a variety of molecules representative of the entire spectrum of normal or pathological conditions (see **Figure 1.11**). In human saliva are secreted endogenous substances at relative tissue concentrations, as well as molecules used for recreational purposes or therapy and markers of hormonal, immunological status, neurological and metabolic conditions.

Salivaomics is a term introduced in 2008 consequentially to the rapid development of knowledge on *-omics* salivary constituents[82–84]. To date, there are five major salivary diagnostic elements such as proteome, microbiome, transcriptome, micro-RNA, and metabolome to classify the salivary constituents as biomarkers. Most common and abundant salivary substances with clinical relevance (validated biomarkers) include microparticles, viruses, bacteria, various proteins, immune system complement as IgA, IgG, IgM, polynucleotides, lipids like cholesterol and triglycerides, steroid hormones, electrolytes and small signalling molecules[75,85].

Human saliva shows another tempting quality: it can be quickly and easily collected without training[86,87].

A relevant limitation to the use of saliva in diagnostics concerns the analyte concentration, as they are generally present in lower percentage than in serum. Such issue inevitably calls for a new generation of sensitive diagnostic methods to be designed. Despite the variety of nanoparticle-based colorimetric detection

mechanisms reported in the literature, no one of these can be effectively used to detect salivary biomarkers.

1.6.1 Salivary glucose as biomarker

Type 1 diabetes is a chronic autoimmune condition caused by the pancreas reduced (or absent) insulin production with unknown causes and without no way to prevent. Type 2 diabetes is a chronic progressive pathology with gradually loss of the ability to secrete sufficient insulin. Diabetes is frequently caused by lifestyle factors (obesity lacking physical activity), even if genetics also plays an important role, in fact in Asian populations type II diabetes is described as an "epidemic"[88,89]. Diabetes is constantly increasing impact on the population. From 2000 to 2016 there was a 6.8% increase of premature deaths (3.96 million in the age group 20-79 year) for diabetes; in 2014, more than the 8.5% of 18 aged adults was diagnosed with diabetes. Although the blood can be considered as the gold standard fluid for the disease diagnosis and monitoring, the associated risk of exposure to infections, the difficulties of sampling from children and/or chronically ill patients, can heavily affect compliance, strongly discouraging this kind of tests[90–93].

Self-monitoring glucose is a basic, routine procedure for diabetic patients. Education programs promote this practice emphasising the correct disposal of needles to avoid contaminations other than transmission of blood borne viruses[94]. However, despite the carefulness, hepatitis outbreaks have been reported in settings where multiple patients with diabetes undergo self or assisted monitoring of blood glucose. United States investigated 18 types of hepatitis B virus (HBV) infection outbreaks (1990-2008) associated with the improper use of blood glucose monitoring equipment[95].

Since glucose level is challenging to monitor and patients spend considerable periods in hyperglycaemic conditions (outside target range), an intensive insulin administration is often correlated with death, while more frequent glycaemic assessments reduce mortality and morbidity in critical ill persons, improving

observed beneficial outcome[96,97]. Regular glycaemia self-monitoring helps people to handle diabetes understanding the impact of food intake, sport activity, stress, illness etc. on their glucose levels. Frequent self-monitoring allows people to maintain an appropriate quality of life, and to adjust medications improving long-term health outcomes. This results into a reduced risk of diabetes-related complications (heart attack, stroke and irreversible damage to eyes, kidneys and nerves)[96,98,99]. There are several devices currently available to monitor glucose levels reported in **Table 1.1** and classified into three main categories.

Self-Monitoring Blood Glucose – SMBG	Continuous Glucose Monitoring– CGM	Flash Glucose Monitoring – FGM10
• Pain • Infection • Inconvenience with bulky kit to carry around and use • Embarrassment of testing in public • Fear of stigmatisation • Complexity of using lancet device	• Painful sensor insertion • Infection • Skin irritation and adhesion problems • Body image concerns about the visibility of the sensor • Difficulty in placing multiple devices on small bodies • Unsettling or annoying alarms • Demanding calibration procedures using SMBG • Lost signals resulting in data gaps • Difficulties related to the need for additional SMBG	• Infection • Allergic reactions • Skin reactions – redness, itching and rash • Bruising and bleeding • Sensor-insertion events • Sensor adhesive or site reactions

Table 1.1 Risks and difficulties with available invasive glucose monitoring devices for people with diabetes (ref. 100).

Self-monitoring blood glucose (SMBG) devices are the most affordable but also painful and costly. Continuous glucose monitoring (CGM) and flash glucose motinoring (FGM) devices offer a convenient option, even if the complexity of these technologies can be a restriction as the skin penetration entails a risk of pain, reactions, allergies and infections[100–102]. In this context, the use of saliva as biological source is attracting great interest from POC testing community to develop novel methods for glucose levels self-monitoring. Several studies report a good correlation between the blood glucose levels and the salivary ones. Despite the quantity of data, the literature is contradictory since several parameters affect

the salivary glucose values, most of which related to the collecting protocol and the subject group enrolment criteria used for the studies. However, P. Balanet al.[103] found that salivary glucose levels are significantly higher in uncontrolled diabetic subjects (13.35 ± 6.61 mg/dl) and controlled diabetic subjects (4.95 ± 2.479 mg/dl) than in nondiabetic subjects (1.18 ± 0.675 mg/dl), in accordance with previous studies[104,105]. Likewise, other works reported a remarkable correlation with variable ratios from 1:40 to 1:100 depending on the considered population (healthy or diabetic, age, body mass index etc.)[106–108] (see **Figure 1.12** and **1.13)**.

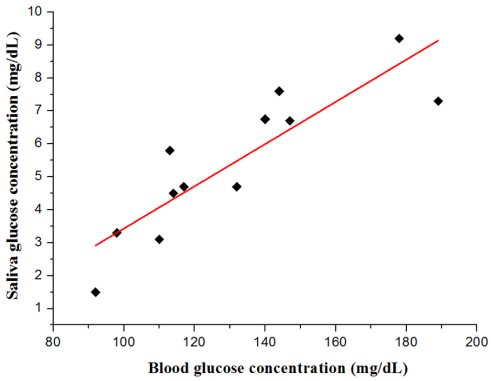

Parameters	Serum	Saliva	P value
Glucose	132 ± 5(mg/dl)	11±1.5(mg/dl)	0
Total protein	6.8±.86(gm/dl)	1.5± .22(mg/dl)	0
Calcium	9.1±1.7(mg/dl)	10.2±1.8(mg/dl)	.2857
Phosphorus	4.3 ±.40(mg/dl)	10.5±2.1(mg/dl)	0

Parameters	Groupl	Group II	P value
Glucose	11 ±1.5	1.5 ±.64(mg/dl)	0
Total Protein	1.5 ±.22	1.3±.50	0.03
Calcium	10.2 ±1.8	7.2 ±1.1	0
Phosphorus	10.5±2.1	8.1 ±.56	0

Figure 1.12 On the left, representative salivary-blood glucose level correlation (ref. 109). On the right, comparison of salivary and serum components in diabetes type II (above) and comparison between diabetic (group I) and non-diabetic (group II) persons (below).

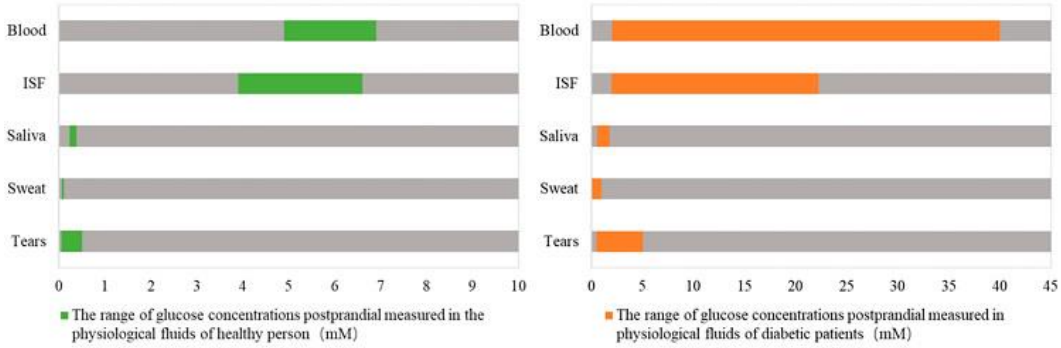

Figure 1. 13 Contrast of glucose concentrations in different physiological fluids between healthy and diabetic people[108].

Researchers have been attempting for several years to design functional commercial non-invasive glucose measurement devices. There are several

challenges associated with non-invasive monitoring and many factors that participate to inaccurate result readings. Sensitivity, selectivity and interferences represent the main obstacles even due to the limitations in hardware and software state of the art. Nevertheless, thanks to the new technologies and the continuous improvements, the appearance of novel and effective non-invasive glucose sensor is only a matter of time[109].

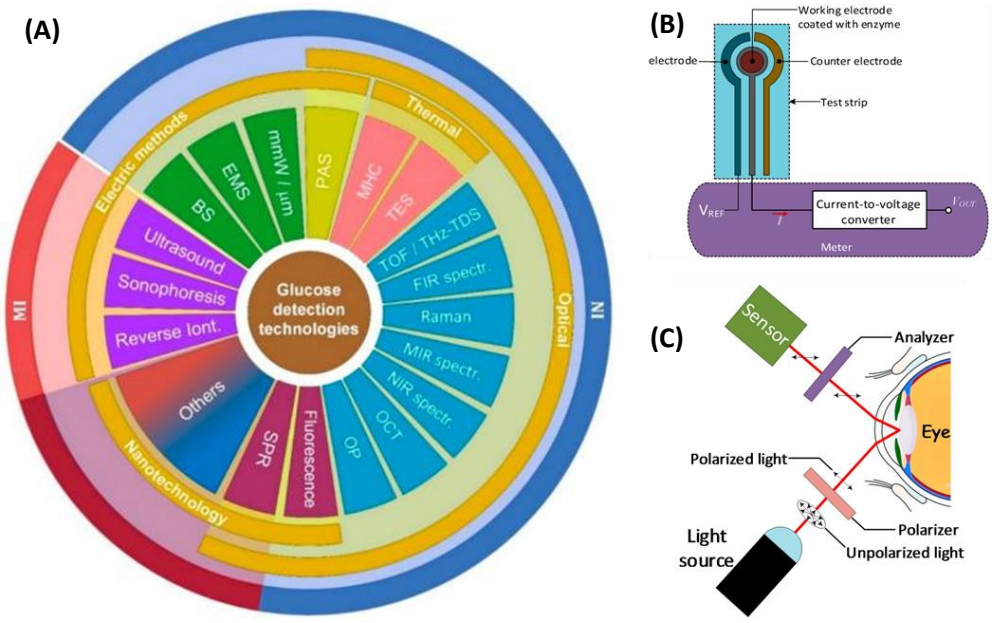

Figure 1.14 (A) Technologies under development for minimally invasive and non-invasive glucose detection; **(B)** block diagram of the device for glucose measurement with finger-pricking method; **(C)** principle of optical polarimetry in the eye for glucose monitoring [110].

1.7 Gold nanoparticles for nanobiosensor

1.7.1 Introduction to gold nanoparticles

The significant developments in microfabrication techniques have inspired the design of a new generation of metal-nanoparticle based sensors, which exploit the interesting physicochemical properties of such nanosized materials. Among them, gold nanoparticles (AuNPs) have revealed attractive tools to fabricate rapid and colorimetric detection platforms, due to their unique catalytic and optoelectronic

properties, and their easy preparation. High quality AuNPs can be rapidly synthesized by several standardized physical (laser ablation microwave and ultraviolet irradiation), chemical, and biological methods[110]. The most widely used is the wet chemical reaction[111,112] that produces stable AuNPs in aqueous medium. AuNP stability is a crucial factor for their applicability, and it is generally provided by a shell of charged capping agents, like trisodium citrate or cetyltrimethylammonium bromide (CTAB). Such array lends an electrical double layer (EDL), so that AuNPs undergo an electrostatic repulsion that prevents their aggregation and confers colloidal stability, according to the principles of Derjaguin–Landau–Verwey–Overbeek (DLVO) theory[113–116] (see **Figure 1.15**). Typically, particle stability is quantified by measuring the zeta potential values that correspond to the electrical potential at the external interface of the EDL. Nanoparticle solutions that present zeta potential lower than – 25/30 mV o higher than 25/30 mV have great colloidal stability, enough to remain stable (monodispersed particles) in solution for desired applications[117]. Nanoparticle environmental changes, such as the displacement of weakly bound capping agents, strongly affect both the Stern layer and the outer diffuse layer that show high plasticity[118].

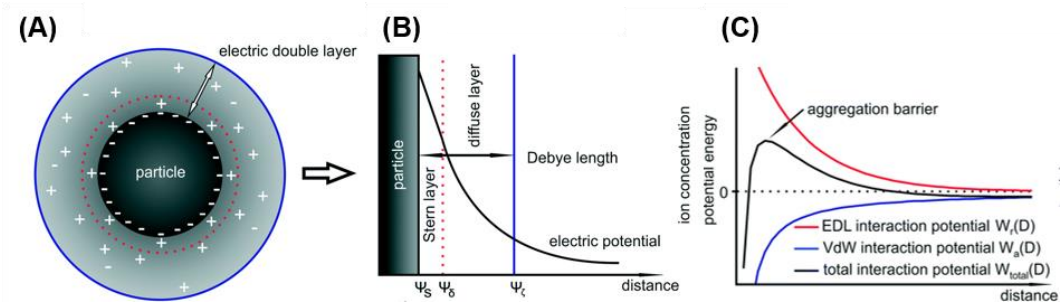

Figure 1.15 (A) Formed electrical double layer (EDL) which consists of the inner Stern layer and the outer diffuse layer; **(B)** corresponding decrease in the counter- and co-ion concentrations with respect to the distance from the particle surface; **(C)** plotting of the EDL, van der Waals and total interaction potentials of two nanoparticles [116].

The salt-induced aggregation is a well-known process in which the increased ionic strength of the solution makes the AuNPs thermodynamically unstable culminating in the diffusion-limited cluster aggregation or the reaction-limited cluster aggregation. To increase the nanoparticle stability and to assign bio-recognizing features at the same time, AuNP capping agents can be chemically substituted with several functional groups like protein, polymers and oligonucleotides. The peculiar physical and optical properties have rendered AuNPs suitable candidates to develop nanobiosensor that promise to be more sensitive, specific, and rapid compared to the conventional biochemical assays[119,120].

1.7.2 Gold nanoparticles properties

While bulk gold has a familiar yellow color in reflected light, thin Au films look blue in transmission and this blue color gradually changes through several tones of purple and red as the particle size is reduced to the nanometer range. This interesting optical behavior is due to a phenomenon known as Localized Surface Plasmon Resonance (LSPR)[118,119].

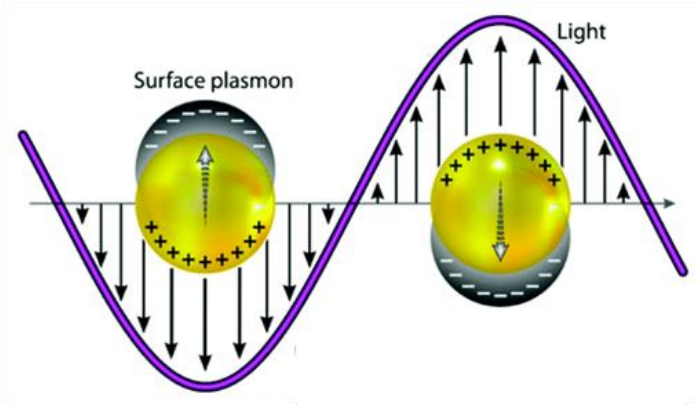

Figure 1.16 Schematic illustration of the resonant oscillation of conduction electrons in metal nanoparticles, which is responsible for the Localized Surface Plasmon Resonance (LSPR) phenomenon.

When electromagnetic radiation hits the particles, the conduction electrons respond with a collective oscillation (surface plasmon) at a certain frequency

(plasmon frequency), determined by parameters such as material, shape, size and dielectric constant of the environment[37] (see **Figure 1.16**).

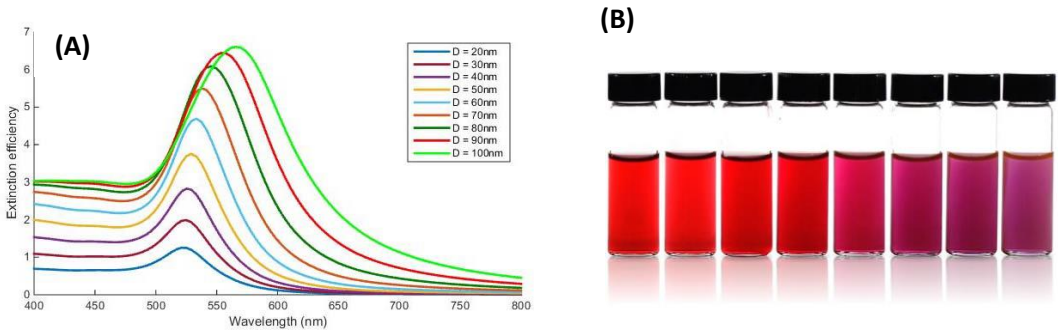

Figure 1.17 (A) Gold nanoparticle size dependant surface plasmon resonance; **(B)** colour shifting of various monodispersed colloidal gold nanoparticles [124-126].

When the frequency of the incident radiation matches the frequency of the particle electron cloud, there is a resonant interaction resulting into a great light scattering and an optical absorbance, with absorption peaks corresponding to the plasmon frequency[123]. For AuNPs such plasmon frequency interests the visible range of the electromagnetic spectrum, resulting in intensely coloured suspensions (see **Figure 1.17**) visible by visual inspection[121,122].

Moreover, AuNPs are endowed with an extinction coefficient that is three to five orders of magnitude higher than the brightest molecular dye, inducing a visible colour even at pM concentrations. Importantly, such optical features can be tuned by controlling the structure of AuNPs in terms of shape, size, inter-particle distance and environmental shell.

For instance, according to Gan theory[124,125], by changing the AuNP shape from spheres to rods, the plasmon band splits into two bands, one of which in NIR region (corresponding to electron oscillations along the long axis, referred to longitudinal band), and the other one in the visible region at a wavelength similar to that of gold nanospheres. To date, there are several methods reported to prepare various crystalline geometries such as wet chemical growing, e-beam coating or chemical etching. Among the available structures (nanorods, nanotriangles, nanocubes, bipyramid, and nanoshells)[126,127], multibranched (MB, star shaped) AuNPs appear attractive for their remarkable electromagnetic field,

stronger than the one of spherical nanoparticles (as confirmed by surface-enhanced Raman scattering and surface-enhanced fluorescence measurements), other than for the ability to synthetically fine-tune the shape[128].

The sharp and long edges of such nanocrystals result in an effective electromagnetic hot spot with related red-shift of the resonance peak due to the size effect. As the tip diameter increases, the inter-particle distance and the relative electric field increase too, while the attraction becomes weaker[122,129]. Consequently, the electric dipole oscillation period increases, and the resonance peak moves to lower frequencies (**Figure 1.18A**)[129]. The same red-shift of the LSPR is observed when increasing the number of tips (**Figure 1.18B**). In this case, a range of frequencies in the visible and near-IR can be covered by tuning MB-AuNP size and shape.[130]

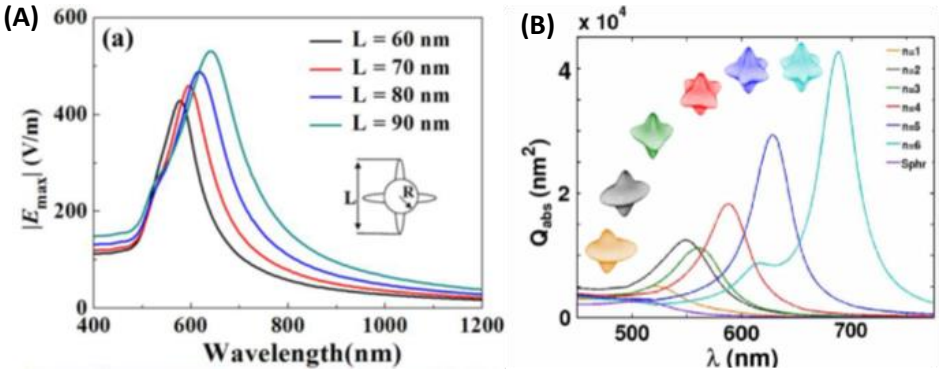

Figure 1. 18 (A) Resonance spectrum of multibranched gold nanoparticles with different tip length[129]; **(B)** absorption cross sections for Au nanostars with different number of tips from along with that for the equivalent Au nanosphere [134]**.**

Concerning the synthesis, there are several published methods to produce branched gold nanoparticles that require surfactants such as polymers, biomolecules or ions (cetyltrimethylammonium bromide, CTAB; polyvinylpyrrolidone, PVP, silver nitrate, $AgNO_3$ etc.) acting as shape-directing agents in seed-mediated approaches[131,132]. These molecules can strongly adsorb onto the nanocrystal surface, poisoning the reactivity. An interesting synthetic method combines NH_2OH and HEPES (2-[4-(2-hydroxyethyl)piperazin-1-yl]ethane

sulfonic acid) to obtain a complete set of MB-AuNPs, tuning the nanostructuration during the anisotropic seeded growth (**Figure 1.19**)[128].

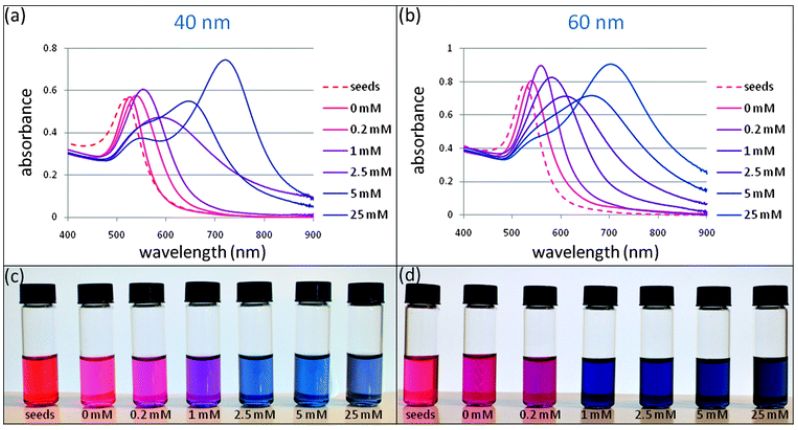

Figure 1.19 (A) and **(B)** UV-Vis spectra of the 40 and 60 nm Au MBNPs, grown in the presence of different concentrations of HEPES. The increasing SPR redshift is also observable by a representative photograph of Au MBNPs **(C)** and **(D)**[132].

AuNP property portfolio also includes remarkable catalytic activity in several reducing and oxidating reactions[133–135]. Common catalysed reactions include the thermal cis-trans isomerization, CO oxidation, cyclotrimerization, selective hydrogenations of nitro compounds, aldehydes, ketones etc. (**Figure 1.20 A**)[136]. Furthermore, recently, it has been reported that AuNPs can display enzymatic properties, being capable to mimic enzymatic activities such as reductase, glucose oxidase, peroxidase, catalase, superoxide dismutase and oxidase[136,137]. Several studies explored the dependence of AuNP catalytic properties according to their size and shape, and, in particular, they reported that a size reduction correspond to higher catalytic activity since the exposed surface is proportional to the activity (**Figure 1.20 B**) [136,138].

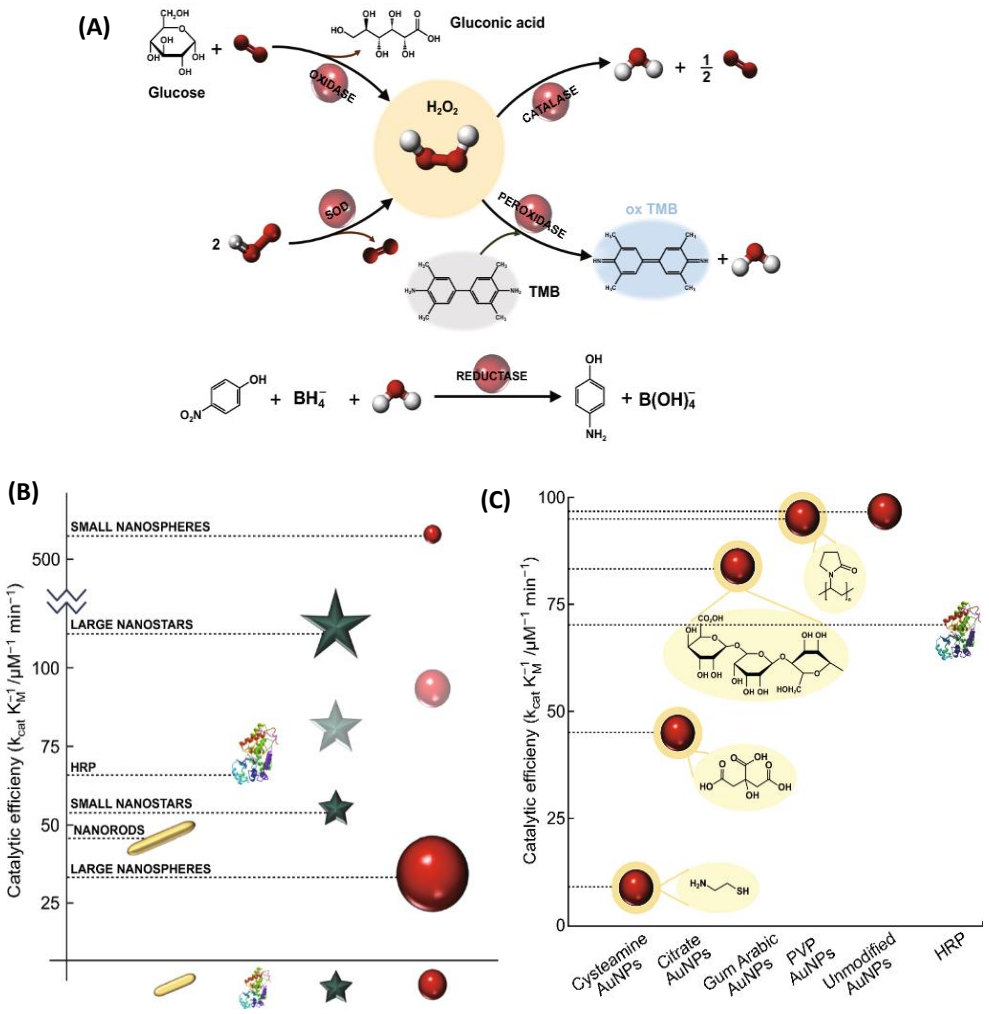

Figure 1.20 (A) Summary of the different AuNPs catalytic activities with representative examples; **(B)** comparison of the catalytic efficiency for the peroxidase-like activity of different-shaped and different-sized AuNPs. Horseradish peroxidase (HRP), their biological counterpart, is also included in the graph; **(C)** peroxidase-like activity of AuNP dependence on different surface modifications, measured as its catalytic efficiency [140].

1.7.3 Gold nanoparticle synthesis

AuNPs can be easily prepared by wet chemical synthesis that involves the reduction of gold ions by the use of chemical reductants[139]. Turkevich first reported the method to produce AuNP colloidal suspension by a single-step reduction process of ($AuCl^{4-}$) using sodium citrate as the reducing agent (whenever required, it is also possible resort to more than one reductant) [140].

Other common reductants include ascorbic acid, tannic acid, molecular hydrogen, hydrazine etc. In any case, the colloidal stabilization phase, by means of capping agents, is fundamental for a successful synthesis[141,142]. There are a number of advantages in using the chemical reduction protocol to synthesize AuNPs. Wet chemical processes are simple, produce metal nanocrystal closely similar in size and stable; the protocol is simple to scale-up and reproducible[115,143].

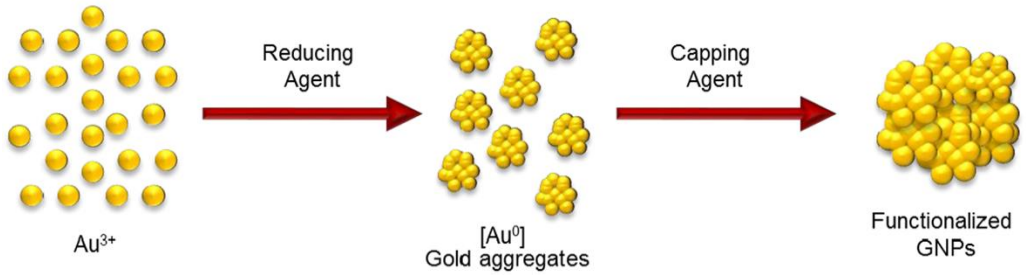

Figure 1.21 Schematic representation of the generalized mechanism of nanoparticle growth due to coalescence [148].

Briefly, a source of Au^{3+} (such as tetrachloroauric acid, $HAuCl_4$), is boiled and reduced to metallic gold (Au^0) adding trisodium citrate. These activated atoms start the nucleation step, leading to a 15 nm well-dispersed AuNPs that are stabilized by trisodium citrate (**Figure 1.21**). This protocol has been optimized adjusting $HAuCl_4$/citrate ratio, temperature and pH value in order to improve AuNP monodispersion in size and shape. 35 nm spherical AuNPs are, then, synthetized using the 15 nm seeds and following the seeded growth approach, which exploits the property of the reducing agent hydroxylamine to quantitatively and selectively reduce Au^{3+} to elemental metal on the Au seeds surface[143,144].

1.7.4 Gold-nanoparticle based colorimetric strategies

Among the available tools, the colorimetric nanobiosensors are the favourite methods for the design of POC devices for diagnosis and health condition assessment, environmental control, pollution monitoring and food analysis.

AuNPs exhibit certain properties as the strong LSPR in the visible region (and high extinction coefficients) and the enzymatic-like activity, which can be exploited to develop rapid, low-cost, and sensitive colorimetric sensors that allow clear and easy-to-interpret results. Therefore, the most studied gold-nanoparticle based colorimetric methods[145] include aggregation-, growth-, etching- and nanozyme-based mechanisms as summarized in **Figure 1.22**.

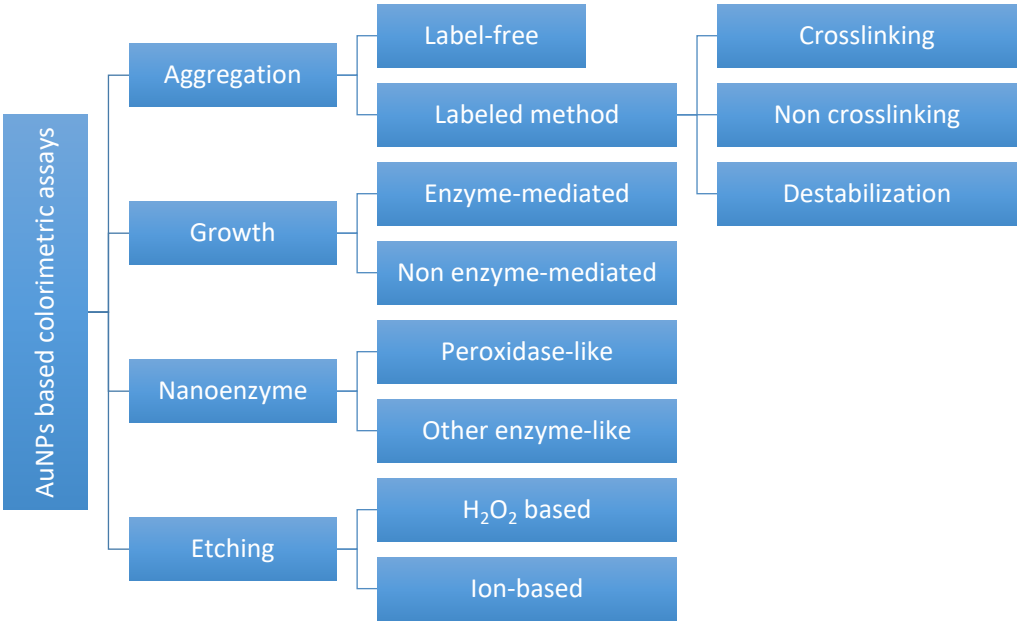

Figure 1.22 Summary of different types of gold-nanoparticle based colorimetric sensors (ref. 150).

Among the AuNP based methods, one of the most popular and diffused colorimetric sensing strategy is the controlled nanoparticle aggregation. This approach relies on a decrease in distance between nearby particles that results in a plasmon coupling effect and related colour shift. Such approach has become dominant in the field of colorimetric sensors since it requires a simple design and exhibits a high sensitivity[146].

As reported in **Figure 1.23**, the *labelled methods* relies on the use of AuNP-probes, meaning AuNPs functionalized with ligands such as DNA, antibodies or peptide. These chemically modified AuNPs have higher inter-particle repulsions and result to be more stable in high ionic strength environments than bare AuNPs, which undergo the salt-induced aggregation. AuNPs controlled aggregation strategies

can be achieved by *crosslinking*, *non-crosslinking*, or *destabilization* aggregation[147,148]. In the first approach, the crosslinker plays a crucial role, as it induces the aggregation through several mechanism. For instance, if the crosslinker is a small molecule that can be activated or suppressed, the AuNP aggregation ca be easily controlled by regulating the linker state.

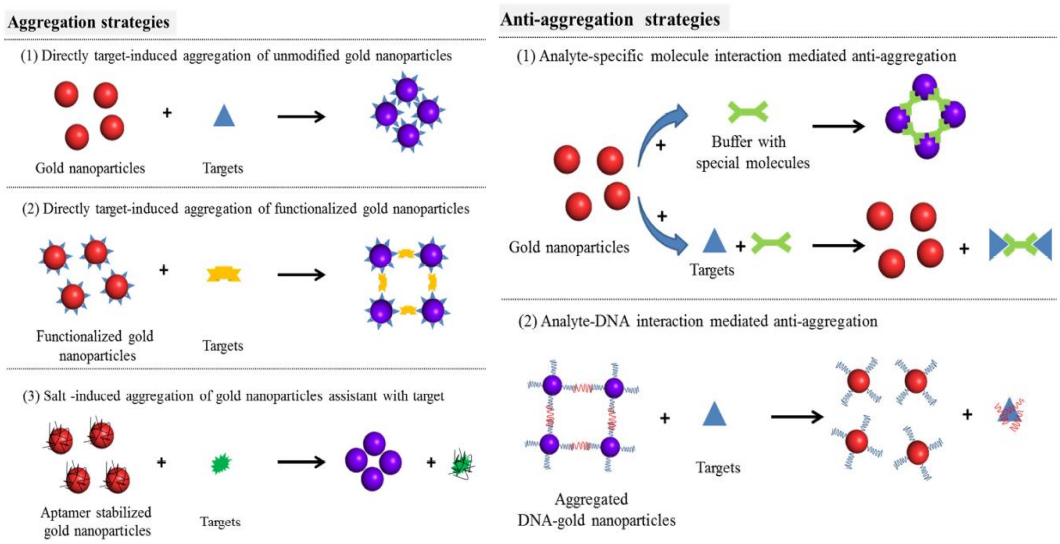

Figure 1.23 Typical strategies of colorimetric detection mechanism based on gold nanoparticles plasmonic shifting (ref. 151).

Another mechanism exploits the complementarity of oligonucleotides. An example was reported to detect Hg^{2+}, using the thymine-Hg^{2+}-thymine coordination chemistry and ssDNA-AuNP probes[149]. Hg^{2+} forms stable T-Hg^{2+}-T base pairs and increases the T_m value, thus inducing the complementary hybridization of ssDNA onto the AuNPs (see **Figure 1.24 A**). Similarly, using the crosslinking approach, Retout et al.[150] developed a rapid method for the detection of MDM2 oncoprotein (p53- and p14-binding protein with regulating functions). The AuNPs were functionalized with p53 and p14 proteins. In the presence of MDM2, the formation of a ternary complex (p53-MDM2-p14) caused the AuNP aggregation and relative colour change of the solution from red to blue. (**Figure 1.24 B**).

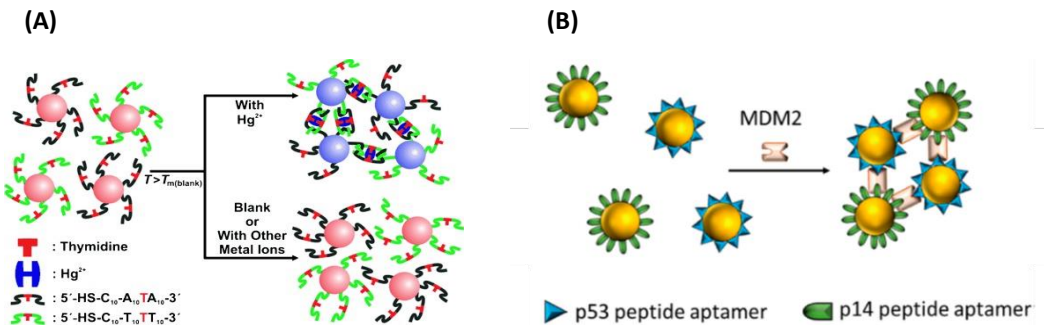

Figure 1.24 (A) Colorimetric detection of mercuric ion (Hg2+) using DNA–Au NPs (ref. 154); **(B)** detection of MDM2 using two peptide aptamer- functionalized AuNPs. The aggregation of the AuNPs was driven by the formation of a ternary complex of Mdm2, p53, and p14 (ref. 155).

The *non-crosslinking* approach deals with a spontaneous aggregation of AuNPs due to a destabilizing event. For instance, dsDNA-AuNP complexes are less stable in an aqueous medium than ssDNA-AuNP system, because the fully matched duplex reduces the repulsive interactions. Such strategy was successfully applied in the colorimetric detection of various targets, and some modifications in the mechanism were introduced to improve the dsDNA–AuNP method sensitivity.[151].

In the *destabilization*-induced aggregation strategies, AuNPs aggregate by cleaving partially or totally the ligand that provides their electro/steric stabilization. Pathogenic bacterial DNA can be detected by RNAse H-controlled aggregation of RNA-functionalized AuNPs. RNA ligand was cleaved by RNAse H with simultaneous DNA–RNA hybridization (see **Figure 1.25**) [152]. Another example of this approach uses aptamers that are oligonucleotides designed to have an affinity for a particular analyte, such as proteins, ions and small molecules[153]. These short sequences of nucleotides are adsorbed onto the AuNP surface that is stabilized. In the presence of the analyte, the aptamers leave the AuNP surface, determining a AuNP aggregation, whose rate is proportional to the target concentration.

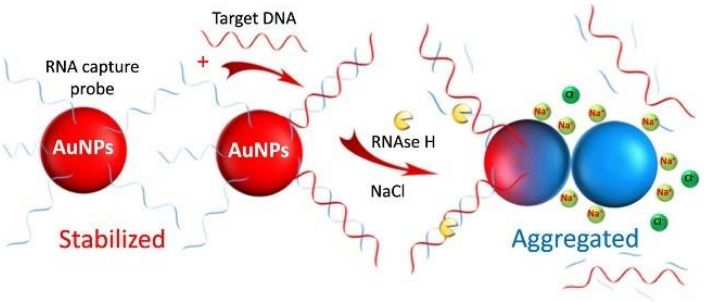

Figure 1.25 The RNAse H enzymatic cleavage in combination with DNA-RNA hybridization provides a highly specific and ultra-sensitive assay for the detection of DNA (ref. 157).

Despite these strategies have revealed effective and easy to be designed, they show mainly two problems: the generation of false positive/negative, due to an unspecific aggregation induced by several factors like solvent, pH, temperature, ions, or molecules; the complex modification of the linker molecules onto the nanoparticles.

Recently, a new class of nanosensors were developed, based on the enzymatic or chemical growth of small AuNPs on catalytic seeds. On the base of the principle for which hydrogen peroxide can be used as the reductant for AuNP growth, a colorimetric sensor for metal ion detection was developed[154]. For instance, Zhou and Ma reported an assay for the detection of mercury ions[155]. In particular, in the absence of Hg^{2+} ions, gold nanoclusters (AuNCs) catalysed H_2O_2 chemical dissociation and the Au crystal growth kinetics was slow. Otherwise, in the presence of Hg^{2+} ions, AuNC catalytic activity was inhibited toward H_2O_2 and the Au^{3+} reduction occurred at a fast rate, and non-aggregated AuNPs were grown.

In parallel to the growth methods, a new group of colorimetric methods is emerging[156]. Several AuNPs, from gold nanospheres to gold nanorods (AuNRs) and nanotriangles, are exploited in etching-based sensors. The etching process consists of a shape reduction and a size modification of the nanoparticles with corresponded LSPR shift. The use of etchants agents as H_2O_2 and halogen ions can preferentially etch the AuNR terminals, leading to a lower aspect ratio or spherical AuNPs[157]. AuNR etching by H_2O_2, as reported, shows several drawbacks in the reaction conditions, because the high concentration of H_2O_2 and the harsh conditions in terms of temperature and pH, may limit the suitability of this system for sensing purposes.

The introduction of catalytic agents such as metal ions and enzymes could overcome this issue with fast reaction kinetics. Therefore, fast and sensitive methods were reported in the literature, based on Fenton-like o horseradish peroxidase (HRP) catalysed etching[158] (see **Figure 1.26 A**). In the same way, the halide ions were used to increase the oxidative etching of AuNRs, promoting the solubility of gold monoxide. For example, the colorimetric detection of molybdate was optimized using the iodine-mediated etching method[159] (see **Figure 1.26 B**). H_2O_2 could oxidize I^- to I_2 that can corrode CTAB, the stabilizer for AuNRs in acid condition. Such reaction could be accelerated adding molybdate that promote the reaction between H_2O_2 and I^-[157,160].

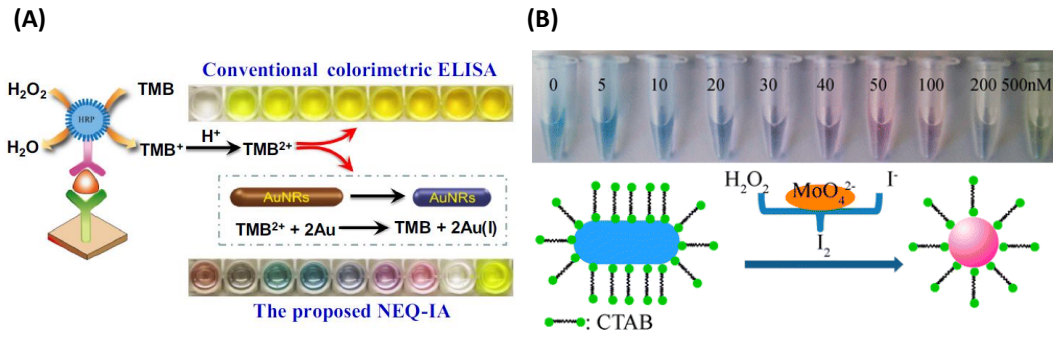

Figure 1.26 (A) The aspect ratios of AuNRs gradually decrease with the increase of TMB^{2+}, and the solution displays a colourful transition[163]; **(B)** colorimetric detection of molybdate based on catalytic etching of AuNRs[164].

In addition to the plasmonic properties, AuNPs are known to be effective as nanozymes, metal nanoparticles able to catalyse several reactions in strong, non-physiological conditions. Charged AuNPs can greatly promote the oxidation of the substrate 3,3,5,5-tetramethylbenzidine (TMB) in the presence of H_2O_2 to generate a characteristic blue coloured solution. Thus, TMB chromogenic oxidation reaction can be used to enhance the output of several recognition mechanism[145]. For example, Jiang et al. demonstrated that chitosan-functionalized AuNPs showed higher peroxidase-like activity than the one exhibited by natural enzymes[161]. In another work, Kwi Nam Han et al. proved that Hg^{2+} could boost the catalytic property of AuNPs, so the mercury ions could be detected exploiting AuNPs@Hg,

increasing the activity on TMB oxidation reaction[162] (see **Figure 1.27 A**). Wu et al. synthesized 2,6-diaminopurine (DAP)-capped AuNPs that responded to the presence of Fe^{2+} with an increased peroxidase-like activity[163] (see **Figure 1.27 B**). A sensitive Fe^{2+} sensor was optimized for the assessment of both haemoglobin HB and red blood cells RBCs in urine samples.

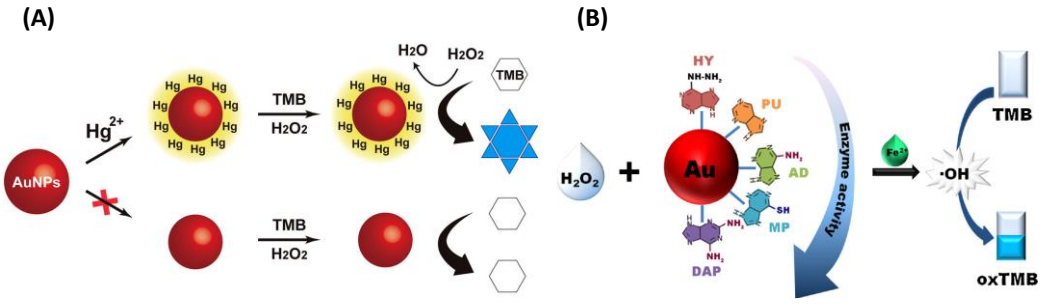

Figure 1.27 (A) Schematic illustration of the colorimetric PAD sensing mechanism for Hg^{2+} ions based on the mercury-promoted nanozyme activity of AuNPs (ref. 167); **(B)** the molecular structure of purine derivatives and the peroxidase like activity process of the AuNPs [168].

Shah et al. studied how the adenosine triphosphate (ATP) could promote the peroxidase-like activity of citrate-capped AuNPs and developed a nanosensor to detect ATP molecules[164]. These approaches extremely reduce the costs, simplifying the procedures and shortening the execution time. Moreover, these assays are suitable for smartphone-based devices, smart platform to detect, transduce and analyse data in short time. Nevertheless, there are still critical issues that need to be solved for effective applications in real sample testing for POC device set-up.

1.8 Bibliography

1. CFR - Code of Federal Regulations Title 21.
2. EUR-Lex - 32017R0746 - EN - EUR-Lex. Available at: https://eur-lex.europa.eu/eli/reg/2017/746/oj. (Accessed: 21st January 2021)
3. Beeler, J. F. Development and Commercialization of In Vitro Diagnostics: Applications for Companion Diagnostics. in *Biotechnology Entrepreneurship: Starting, Managing, and Leading Biotech Companies* 331–340 (Elsevier Inc., 2014). doi:10.1016/B978-0-12-404730-3.00024-5
4. Rooney, K. D. & Schilling, M. M. Point-of-care testing in the overcrowded emergency department - Can it make a difference? *Crit. Care* **18**, (2014).
5. Parco, S., Visconti, P. & Vascotto, F. Hematology point of care testing and laboratory errors: An example of multidisciplinary management at a children's hospital in northeast Italy. *J. Multidiscip. Healthc.* **7**, 45–50 (2014).
6. Rothschild, J. M. *et al.* The Critical Care Safety Study: The incidence and nature of adverse events and serious medical errors in intensive care*. *Crit. Care Med.* **33**, 1694–1700 (2005).
7. Cecconi, M. *et al.* Consensus on circulatory shock and hemodynamic monitoring. Task force of the European Society of Intensive Care Medicine. *Intensive Care Med.* **40**, 1795–1815 (2014).
8. Sarr, M. G., Gott, V. L. & Townsend, T. R. *COLLECTIVE REVIEW Mediastinal Infection after Cardiac Surgery*. doi:10.1016/S0003-4975(10)62300-4
9. Lee-Lewandrowski, E. *et al.* Implementation of a point-of-care satellite laboratory in the emergency department of an academic medical center: Impact on test turnaround time and patient emergency department length of stay. *Arch. Pathol. Lab. Med.* **127**, 456–460 (2003).
10. Asha, S. E. *et al.* Impact from point-of-care devices on emergency department patient processing times compared with central laboratory testing of blood samples: A randomised controlled trial and cost-effectiveness analysis. *Emerg. Med. J.* **31**, 714–719 (2014).
11. Schilling, U. M. Time is Money—the Economic Impact of Point of Care on the Emergency Department of a Tertiary Care University Hospital. *Point Care J. Near-Patient Test. Technol.* **13**, 21–23 (2014).
12. Global Point of Care (POC) Diagnostics Market 2019-2023| 10% CAGR Projection Over the Next Five Years | Technavio | Business Wire.
13. Point-of-Care Diagnostics Market | Growing at a CAGR of 10.4% | MarketsandMarkets. Available at: https://www.marketsandmarkets.com/Market-Reports/point-of-care-diagnostic-market-106829185.html. (Accessed: 21st January 2021)
14. Wang, Y., Yu, L., Kong, X. & Sun, L. Application of nanodiagnostics in point-of-care tests for infectious diseases. *Int. J. Nanomedicine* 12–4789 (2017). doi:10.2147/IJN.S137338
15. Tang, Y. W., Schmitz, J. E., Persing, D. H. & Stratton, C. W. Laboratory diagnosis of COVID-19: Current issues and challenges. *Journal of Clinical Microbiology* **58**, (2020).
16. Li, Z. *et al.* Development and clinical application of a rapid IgM-IgG combined antibody test for SARS-CoV-2 infection diagnosis. *J. Med. Virol.* **92**, 1518–1524 (2020).

17. Soh, J. H., Chan, H. M. & Ying, J. Y. Strategies for developing sensitive and specific nanoparticle-based lateral flow assays as point-of-care diagnostic device. *Nano Today* **30**, 100831 (2020).

18. Kim, H., Chung, D. R. & Kang, M. A new point-of-care test for the diagnosis of infectious diseases based on multiplex lateral flow immunoassays. *Analyst* **144**, 2460–2466 (2019).

19. Shrivastava, S., Trung, T. Q. & Lee, N. E. Recent progress, challenges, and prospects of fully integrated mobile and wearable point-of-care testing systems for self-testing. *Chemical Society Reviews* **49**, 1812–1866 (2020).

20. Li, K. F. Smart home technology for telemedicine and emergency management. *J. Ambient Intell. Humaniz. Comput.* **4**, 535–546 (2013).

21. Vimarlund, V., Olve Nils-Goran, N. G., Scandurra, I. & Koch, S. Organizational effects of information and communication technology (ICT) in elderly homecare: A case study. *Health Informatics J.* **14**, 195–210 (2008).

22. Mujawar, M. A. *et al.* Nano-enabled biosensing systems for intelligent healthcare: towards COVID-19 management. *Materials Today Chemistry* **17**, 100306 (2020).

23. Ho, T.-B., Le, L., Tran Thai, D. & Taewijit, S. Data-driven Approach to Detect and Predict Adverse Drug Reactions. *Curr. Pharm. Des.* **22**, 3498–3526 (2016).

24. Malik, P. *et al.* Nanobiosensors: Concepts and Variations. *ISRN Nanomater.* **2013**, 327435 (2013).

25. Debnath, N. & Das, S. Nanobiosensor: Current trends and applications. in *NanoBioMedicine* 389–409 (Springer Singapore, 2020). doi:10.1007/978-981-32-9898-9_16

26. Bergveld, P. The impact of MOSFET-based sensors. *Sensors and Actuators* **8**, 109–127 (1985).

27. Nidzworski, D. *et al.* A rapid-response ultrasensitive biosensor for influenza virus detection using antibody modified boron-doped diamond. *Sci. Rep.* **7**, 1–10 (2017).

28. Armbruster, D. A. & Pry, T. Limit of blank, limit of detection and limit of quantitation. *Clin. Biochem. Rev.* **29 Suppl 1**, S49-52 (2008).

29. Syedmoradi, L. *et al.* Point of care testing: The impact of nanotechnology. *Biosensors and Bioelectronics* **87**, 373–387 (2017).

30. Liu, L., Hao, Y., Deng, D. & Xia, N. Nanomaterials-based colorimetric immunoassays. *Nanomaterials* **9**, (2019).

31. Quesada-González, D. & Merkoçi, A. Nanomaterial-based devices for point-of-care diagnostic applications. *Chemical Society Reviews* **47**, 4697–4709 (2018).

32. EUR-Lex - 32011H0696 - EN - EUR-Lex. Available at: https://eur-lex.europa.eu/legal-content/EN/TXT/?uri=CELEX%3A32011H0696. (Accessed: 26th January 2021)

33. Asha, A. B. & Narain, R. Nanomaterials properties. in *Polymer Science and Nanotechnology* 343–359 (Elsevier, 2020). doi:10.1016/b978-0-12-816806-6.00015-7

34. Roduner, E. Size matters: Why nanomaterials are different. *Chem. Soc. Rev.* **35**, 583–592 (2006).

35. Sumanth Kumar, D., Jai Kumar, B. & Mahesh, H. M. Quantum Nanostructures (QDs): An Overview. in *Synthesis of Inorganic Nanomaterials* 59–88 (Elsevier, 2018). doi:10.1016/b978-0-08-101975-7.00003-8

36. Singh, M., Goyal, M. & Devlal, K. Size and shape effects on the band gap of semiconductor

compound nanomaterials. *J. Taibah Univ. Sci.* **12**, 470–475 (2018).

37. Kelly, K. L., Coronado, E., Zhao, L. L. & Schatz, G. C. The optical properties of metal nanoparticles: The influence of size, shape, and dielectric environment. *J. Phys. Chem. B* **107**, 668–677 (2003).

38. Träger, F. Optical properties of nanoparticles. *Applied Physics B: Lasers and Optics* **73**, 291 (2001).

39. Uglov, V. V., Doroshevich, I. L., Kvasov, N. T., Remnev, G. E. & Shymanski, V. I. On physical properties of nanoparticles: size effect and scale of nanoobjects. *Phys. status solidi* **13**, 903–907 (2016).

40. Albanese, A., Tang, P. S. & Chan, W. C. W. The Effect of Nanoparticle Size, Shape, and Surface Chemistry on Biological Systems. *Annu. Rev. Biomed. Eng.* **14**, 1–16 (2012).

41. Edwards, K. A., Bolduc, O. R. & Baeumner, A. J. Miniaturized bioanalytical systems: Enhanced performance through liposomes. *Current Opinion in Chemical Biology* **16**, 444–452 (2012).

42. Lei, J. & Ju, H. Signal amplification using functional nanomaterials for biosensing. *Chemical Society Reviews* **41**, 2122–2134 (2012).

43. Taton, T. A., Mirkin, C. A. & Letsinger, R. L. Scanometric DNA array detection with nanoparticle probes. *Science (80-.).* **289**, 1757–1760 (2000).

44. Lee, K. S. & El-Sayed, M. A. Gold and silver nanoparticles in sensing and imaging: Sensitivity of plasmon response to size, shape, and metal composition. *J. Phys. Chem. B* **110**, 19220–19225 (2006).

45. Alivisatos, P. The use of nanocrystals in biological detection. *Nature Biotechnology* **22**, 47–52 (2004).

46. Malekzad, H., Sahandi Zangabad, P., Mirshekari, H., Karimi, M. & Hamblin, M. R. Noble metal nanoparticles in biosensors: Recent studies and applications. *Nanotechnology Reviews* **6**, 301–329 (2017).

47. Tchounwou, P. B., Yedjou, C. G., Patlolla, A. K. & Sutton, D. J. Heavy Metals Toxicity and the Environment. *EXS* **101**, 133–164 (2012).

48. Clarkson, T. W., Magos, L. & Myers, G. J. The Toxicology of Mercury — Current Exposures and Clinical Manifestations. *N. Engl. J. Med.* **349**, 1731–1737 (2003).

49. Kubáň, P., Pelcová, P., Margetínová, J. & Kubáň, V. Mercury speciation by CE: An update. *Electrophoresis* **30**, 92–99 (2009).

50. Hong, Y. S., Kim, Y. M. & Lee, K. E. Methylmercury exposure and health effects. *J. Prev. Med. Public Heal.* **45**, 353–363 (2012).

51. Poulain, A. J. & Barkay, T. Cracking the Mercury Methylation Code. *Science (80-.).* **339**, 1280 LP – 1281 (2013).

52. Farina, M. & Aschner, M. Methylmercury-Induced Neurotoxicity: Focus on Pro-oxidative Events and Related Consequences. in *Advances in neurobiology* **18**, 267–286 (2017).

53. Farina, M., Aschner, M. & Rocha, J. B. T. Oxidative stress in MeHg-induced neurotoxicity. *Toxicol. Appl. Pharmacol.* **256**, 405–417 (2011).

54. Aschner, M. & Syversen, T. Methylmercury: recent advances in the understanding of its neurotoxicity. *Ther. Drug Monit.* **27**, 278–83 (2005).

55. Farina, M., Rocha, J. B. T. & Aschner, M. Mechanisms of methylmercury-induced neurotoxicity: Evidence from experimental studies. in *Life Sciences* **89**, 555–563 (Elsevier

Inc., 2011).

56. Mahaffey, K. R., Clickner, R. P. & Bodurow, C. C. Blood organic mercury and dietary mercury intake: National Health and Nutrition Examination Survey, 1999 and 2000. *Environ. Health Perspect.* **112**, 562–70 (2004).

57. Mania, M., Wojciechowska-Mazurek, M., Starska, K., Rebeniak, M. & Postupolski, J. [Fish and seafood as a source of human exposure to methylmercury]. *Rocz. Panstw. Zakl. Hig.* **63**, 257–64 (2012).

58. Guerrini, L. *et al.* Chemical speciation of heavy metals by surface-enhanced Raman scattering spectroscopy: identification and quantification of inorganic- and methyl-mercury in water. *Nanoscale* **6**, 8368–8375 (2014).

59. Sahuquillo, I., Lagarda, M. J., Silvestre, M. D. & Farré, R. Methylmercury determination in fish and seafood products and estimated daily intake for the Spanish population. *Food Addit. Contam.* **24**, 869–876 (2007).

60. Gosnell, K. J. & Mason, R. P. Mercury and methylmercury incidence and bioaccumulation in plankton from the central Pacific Ocean. *Mar. Chem.* **177**, 772–780 (2015).

61. Shipp, A. M. *et al.* Determination of a site-specific reference dose for methylmercury for fish-eating populations. *Toxicol. Ind. Health* **16**, 335–438 (2000).

62. *Commission Regulation (EC) No 1881/2006 of setting maximum levels for certain contaminants in foodstuffs (Text with EEA relevance)*.

63. Vieira, H. C., Morgado, F., Soares, A. M. V. M. & Abreu, S. N. Fish consumption recommendations to conform to current advice in regard to mercury intake. *Environ. Sci. Pollut. Res.* **22**, 9595–9602 (2015).

64. Nutrition, C. for F. S. and A. Metals - Mercury and Methylmercury.

65. Hight, S. C. & Cheng, J. Determination of methylmercury and estimation of total mercury in seafood using high performance liquid chromatography (HPLC) and inductively coupled plasma-mass spectrometry (ICP-MS): Method development and validation. *Anal. Chim. Acta* **567**, 160–172 (2006).

66. Rodrigues, J. L., de Souza, S. S., de Oliveira Souza, V. C. & Barbosa, F. Methylmercury and inorganic mercury determination in blood by using liquid chromatography with inductively coupled plasma mass spectrometry and a fast sample preparation procedure. *Talanta* **80**, 1158–1163 (2010).

67. Yao, C.-H., Jiang, S.-J., Sahayam, A. C. & Huang, Y.-L. Speciation of mercury in fish oils using liquid chromatography inductively coupled plasma mass spectrometry. *Microchem. J.* **133**, 556–560 (2017).

68. Li, X. & Wang, Z. Determination of mercury by intermittent flow electrochemical cold vapor generation coupled to atomic fluorescence spectrometry. *Anal. Chim. Acta* **588**, 179–183 (2007).

69. Aranda, P. R., Gil, R. A., Moyano, S., De Vito, I. & Martinez, L. D. Slurry sampling in serum blood for mercury determination by CV-AFS. *J. Hazard. Mater.* **161**, 1399–1403 (2009).

70. Chansuvarn, W., Tuntulani, T. & Imyim, A. Colorimetric detection of mercury(II) based on gold nanoparticles, fluorescent gold nanoclusters and other gold-based nanomaterials. *TrAC - Trends in Analytical Chemistry* **65**, 83–96 (2015).

71. Lou, T., Chen, Z., Wang, Y. & Chen, L. Blue-to-Red Colorimetric Sensing Strategy for Hg^{2+} and Ag^{+} via Redox-Regulated Surface Chemistry of Gold Nanoparticles. *ACS Appl. Mater. Interfaces* **3**, 1568–1573 (2011).

72. Chen, L., Li, J. & Chen, L. Colorimetric Detection of Mercury Species Based on

Functionalized Gold Nanoparticles. *ACS Appl. Mater. Interfaces* **6**, 15897–15904 (2014).

73. Aulsebrook, M. L., Watkins, E., Grace, M. R., Graham, B. & Tuck, K. L. Modified Gold Nanoparticles for the Temperature-Dependent Colorimetric Detection of Mercury and Methylmercury. *ChemistrySelect* **3**, 2088–2091 (2018).

74. Ilyin, S. E., Belkowski, S. M. & Plata-Salamán, C. R. Biomarker discovery and validation: Technologies and integrative approaches. *Trends in Biotechnology* **22**, 411–416 (2004).

75. Yoshizawa, J. M. *et al.* Salivary biomarkers: Toward future clinical and diagnostic utilities. *Clinical Microbiology Reviews* **26**, 781–791 (2013).

76. Peredy, T. R. & Powers, R. D. Bedside diagnostic testing of body fluids. *American Journal of Emergency Medicine* **15**, 400–407 (1997).

77. Gatti, R. *et al.* Cortisol assays and diagnostic laboratory procedures in human biological fluids. *Clinical Biochemistry* **42**, 1205–1217 (2009).

78. Ilea, A. *et al.* Saliva, a magic biofluid available for multilevel assessment and a mirror of general health-a systematic review. *Biosensors* **9**, (2019).

79. Malamud, D. Saliva as a Diagnostic Fluid. *Dental Clinics of North America* **55**, 159–178 (2011).

80. Humphrey, S. P. & Williamson, R. T. A review of saliva: Normal composition, flow, and function. *J. Prosthet. Dent.* **85**, 162–169 (2001).

81. Graphics Inc, P. *Saliva Composition and Functions: A Comprehensive Review*. (2008).

82. Shah, S. Salivaomics: The current scenario. *J. Oral Maxillofac. Pathol.* **22**, 375 (2018).

83. Wong, D. T. W. Salivaomics. *J. Am. Dent. Assoc.* **143**, 19S-24S (2012).

84. Koneru, S. & Tanikonda, R. Salivaomics - A promising future in early diagnosis of dental diseases. *Dent. Res. J. (Isfahan).* **11**, 11–5 (2014).

85. Zhang, L., Xiao, H. & Wong, D. T. Salivary Biomarkers for Clinical Applications. *Mol. Diagn. Ther.* **13**, 245–259 (2009).

86. Bellagambi, F. G. *et al.* Saliva sampling: Methods and devices. An overview. *TrAC - Trends in Analytical Chemistry* **124**, 115781 (2020).

87. Woo, J. S. & Lu, D. Y. Procurement, transportation, and storage of saliva, buccal swab, and oral wash specimens. in *Methods in Molecular Biology* **1897**, 99–105 (Humana Press Inc., 2019).

88. Ma, R. C. W. & Chan, J. C. N. Type 2 diabetes in East Asians: Similarities and differences with populations in Europe and the United States. *Ann. N. Y. Acad. Sci.* **1281**, 64–91 (2013).

89. IDF Diabetes Atlas 9th edition 2019. Available at: https://www.diabetesatlas.org/en/. (Accessed: 28th January 2021)

90. Shaw, J. E., Sicree, R. A. & Zimmet, P. Z. Global estimates of the prevalence of diabetes for 2010 and 2030. *Diabetes Research and Clinical Practice* **87**, 4–14 (2010).

91. Roglic, G. & Unwin, N. Mortality attributable to diabetes: Estimates for the year 2010. *Diabetes Research and Clinical Practice* **87**, 15–19 (2010).

92. Tiongco, R. E., Bituin, A., Arceo, E., Rivera, N. & Singian, E. Salivary glucose as a non-invasive biomarker of type 2 diabetes mellitus. *J. Clin. Exp. Dent.* **10**, e902–e907 (2018).

93. Gupta, S. *et al.* Correlation of salivary glucose level with blood glucose level in diabetes mellitus. *J. Oral Maxillofac. Pathol.* **21**, 334–339 (2017).

94. Klonoff, D. C. & Perz, J. F. Assisted monitoring of blood glucose: Special safety needs for a new paradigm in testing glucose. *Journal of Diabetes Science and Technology* **4**, 1027–1031 (2010).

95. Thompson, N. D. & Perz, J. F. Eliminating the blood: Ongoing outbreaks of hepatitis B virus infection and the need for innovative glucose monitoring technologies. *J. Diabetes Sci. Technol.* **3**, 283–288 (2009).

96. Van den Berghe, G. *et al.* Outcome benefit of intensive insulin therapy in the critically ill: Insulin dose versus glycemic control*. *Crit. Care Med.* **31**, 359–366 (2003).

97. Finney, S. J., Zekveld, C., Elia, A. & Evans, T. W. Glucose Control and Mortality in Critically Ill Patients. *J. Am. Med. Assoc.* **290**, 2041–2047 (2003).

98. Borus, J. S. & Laffel, L. Adherence challenges in the management of type 1 diabetes in adolescents: Prevention and intervention. *Current Opinion in Pediatrics* **22**, 405–411 (2010).

99. Sørgård, B., Iversen, M. M. & Mårtensson, J. Continuous glucose monitoring in adults with type 1 diabetes: A balance between benefits and barriers: A critical incident study. *J. Clin. Nurs.* **28**, 3318–3329 (2019).

100. Hilliard, M. E. *et al.* Benefits and Barriers of Continuous Glucose Monitoring in Young Children with Type 1 Diabetes. *Diabetes Technol. Ther.* **21**, 493–498 (2019).

101. Engler, R., Routh, T. L. & Lucisano, J. Y. Adoption Barriers for Continuous Glucose Monitoring and Their Potential Reduction With a Fully Implanted System: Results From Patient Preference Surveys. *Clin. Diabetes* **36**, 50–58 (2018).

102. *Addressing the Challenges of Invasive Glucose Monitoring*. (2019).

103. Balan, P. *et al.* Can saliva offer an advantage in monitoring of diabetes mellitus? - A case control study. *J. Clin. Exp. Dent.* **6**, e335-8 (2014).

104. Aydin, S. A comparison of ghrelin, glucose, alpha-amylase and protein levels in saliva from diabetics. *J. Biochem. Mol. Biol.* **40**, 29–35 (2007).

105. Carda, C., Mosquera-Lloreda, N., Salom, L., Gomez De Ferraris, M. E. & Peydró, A. A structural and functional salivary disorders in type 2 diabetic patients. *Med. Oral Patol. Oral Cir. Bucal* **11**, 209–214 (2006).

106. Srivastava, P., Agarwal, B. . & Chandel, M. S. A COMPARATIVE STUDY OF SERUM AND SALIVARY BIOCHEMICAL MARKERS IN DIABETES MELLITUS TYPE II WITH HEALTHY INDIVIDUALS. *Int. J. Med. Biomed. Stud.* **4**, 161–164 (2020).

107. Gupta, S. *et al.* Correlation of salivary glucose level with blood glucose level in diabetes mellitus. *J. Oral Maxillofac. Pathol.* **21**, 334–339 (2017).

108. Rp, A. *et al.* Noninvasive Method for Glucose Level Estimation by Saliva. *J Diabetes Metab Cit. Agrawal RP* **4**, 266 (2013).

109. Gonzales, W. V., Mobashsher, A. T. & Abbosh, A. The progress of glucose monitoring—A review of invasive to minimally and non-invasive techniques, devices and sensors. *Sensors (Switzerland)* **19**, (2019).

110. Singh, P. *et al.* Gold nanoparticles in diagnostics and therapeutics for human cancer. *International Journal of Molecular Sciences* **19**, (2018).

111. Low, A. & Bansal, V. A visual tutorial on the synthesis of gold nanoparticles. *Biomed. Imaging Interv. J.* **6**, (2010).

112. Lawrence, M., Testen, A., Koklic, T. & Smithies, O. A simple method for the size controlled synthesis of stable oligomeric clusters of gold nanoparticles under ambient conditions. *J.*

Vis. Exp. **2016**, (2016).

113. Park, J. W. & Shumaker-Parry, J. S. Structural study of citrate layers on gold nanoparticles: Role of intermolecular interactions in stabilizing nanoparticles. *J. Am. Chem. Soc.* **136**, 1907–1921 (2014).

114. Park, J., Joo, J., Soon, G. K., Jang, Y. & Hyeon, T. Synthesis of monodisperse spherical nanocrystals. *Angewandte Chemie - International Edition* **46**, 4630–4660 (2007).

115. Polte, J. Fundamental growth principles of colloidal metal nanoparticles - a new perspective. *CrystEngComm* **17**, 6809–6830 (2015).

116. Al-Johani, H. *et al.* The structure and binding mode of citrate in the stabilization of gold nanoparticles. *Nat. Chem.* **9**, 890–895 (2017).

117. Majzik, A., Patakfalvi, R., Hornok, V. & Dékány, I. Growing and stability of gold nanoparticles and their functionalization by cysteine. *Gold Bull.* **42**, 113–123 (2009).

118. Pamies, R. *et al.* Aggregation behaviour of gold nanoparticles in saline aqueous media. *J. Nanoparticle Res.* **16**, 1–11 (2014).

119. Hutter, E. & Fendler, J. H. Exploitation of localized surface plasmon resonance. *Adv. Mater.* **16**, 1685–1706 (2004).

120. Peixoto de Almeida, M. *et al.* Gold Nanoparticles as (Bio)Chemical Sensors. in *Comprehensive Analytical Chemistry* **66**, 529–567 (Elsevier B.V., 2014).

121. Homola, J., Yee, S. S. & Gauglitz, G. Surface plasmon resonance sensors: review. *Sensors Actuators, B Chem.* **54**, 3–15 (1999).

122. Papavassiliou, G. C. Optical properties of small inorganic and organic metal particles. *Progress in Solid State Chemistry* **12**, 185–271 (1979).

123. Huang, X. & El-Sayed, M. A. Gold nanoparticles: Optical properties and implementations in cancer diagnosis and photothermal therapy. *Journal of Advanced Research* **1**, 13–28 (2010).

124. Lee, K. S. & El-Sayed, M. A. Dependence of the enhanced optical scattering efficiency relative to that of absorption for gold metal nanorods on aspect ratio, size, end-cap shape, and medium refractive index. *J. Phys. Chem. B* **109**, 20331–20338 (2005).

125. Murphy, C. J. *et al.* Anisotropic metal nanoparticles: Synthesis, assembly, and optical applications. *J. Phys. Chem. B* **109**, 13857–13870 (2005).

126. Yaraki, M. T. & Tan, Y. N. Metal Nanoparticles-Enhanced Biosensors: Synthesis, Design and Applications in Fluorescence Enhancement and Surface-enhanced Raman Scattering. *Chem. – An Asian J.* **15**, 3180–3208 (2020).

127. Borzenkov, M., Chirico, G., Collini, M. & Pallavicini, P. Gold Nanoparticles for Tissue Engineering. in 343–390 (Springer, Cham, 2018). doi:10.1007/978-3-319-76090-2_10

128. Maiorano, G. *et al.* Monodispersed and size-controlled multibranched gold nanoparticles with nanoscale tuning of surface morphology. *Nanoscale* **3**, 2227–2232 (2011).

129. Shan, F. & Zhang, T. Theoretical study on surface plasmon properties of gold nanostars. in *IOP Conference Series: Materials Science and Engineering* **322**, 022005 (Institute of Physics Publishing, 2018).

130. Rodríguez-Oliveros, R. & Sánchez-Gil, J. A. Gold nanostars as thermoplasmonic nanoparticles for optical heating. *Opt. Express* **20**, 621 (2012).

131. Senthil Kumar, P., Pastoriza-Santos, I., Rodríguez-González, B., Javier García De Abajo, F. & Liz-Marzán, L. M. High-yield synthesis and optical response of gold nanostars.

Nanotechnology **19**, 015606 (2008).

132. Sau, T. K. & Murphy, C. J. Room temperature, high-yield synthesis of multiple shapes of gold nanoparticles in aqueous solution. *J. Am. Chem. Soc.* **126**, 8648–8649 (2004).

133. Leyva-Pérez, A. *et al.* Reactivity of electron-deficient alkynes on gold nanoparticles. *ACS Catal.* **3**, 1865–1873 (2013).

134. Burch, R. Gold catalysts for pure hydrogen production in the water-gas shift reaction: Activity, structure and reaction mechanism. *Phys. Chem. Chem. Phys.* **8**, 5483–5500 (2006).

135. Herzing, A. A., Kiely, C. J., Carley, A. F., Landon, P. & Hutchings, G. J. Identification of active gold nanoclusters on iron oxide supports for CO oxidation. *Science (80-.).* **321**, 1331–1335 (2008).

136. Lou-Franco, J., Das, B., Elliott, C. & Cao, C. Gold Nanozymes: From Concept to Biomedical Applications. *Nano-Micro Letters* **13**, 1–36 (2021).

137. Lin, Y., Ren, J. & Qu, X. Nano-gold as artificial enzymes: Hidden talents. *Adv. Mater.* **26**, 4200–4217 (2014).

138. Stenlid, J. H. & Brinck, T. Extending the σ-Hole Concept to Metals: An Electrostatic Interpretation of the Effects of Nanostructure in Gold and Platinum Catalysis. *J. Am. Chem. Soc.* **139**, 11012–11015 (2017).

139. Alshammari, A. & Kalevaru, V. N. Supported Gold Nanoparticles as Promising Catalysts. in *Catalytic Application of Nano-Gold Catalysts* (InTech, 2016). doi:10.5772/64394

140. Wuithschick, M. *et al.* Turkevich in New Robes: Key Questions Answered for the Most Common Gold Nanoparticle Synthesis. *ACS Nano* **9**, 7052–7071 (2015).

141. Daruich De Souza, C., Ribeiro Nogueira, B. & Rostelato, M. E. C. M. Review of the methodologies used in the synthesis gold nanoparticles by chemical reduction. *Journal of Alloys and Compounds* **798**, 714–740 (2019).

142. Iqbal, M. *et al.* Preparation of gold nanoparticles and determination of their particles size via different methods. *Mater. Res. Bull.* **79**, 97–104 (2016).

143. Thanh, N. T. K., Maclean, N. & Mahiddine, S. Mechanisms of nucleation and growth of nanoparticles in solution. *Chemical Reviews* **114**, 7610–7630 (2014).

144. Turkevich, J. Colloidal gold. Part I - Historical and preparative aspects, morphology and structure. *Gold Bull.* **18**, 86–91 (1985).

145. Chang, C. C. *et al.* Gold nanoparticle-based colorimetric strategies for chemical and biological sensing applications. *Nanomaterials* **9**, (2019).

146. Chen, H., Zhou, K. & Zhao, G. Gold nanoparticles: From synthesis, properties to their potential application as colorimetric sensors in food safety screening. *Trends in Food Science and Technology* **78**, 83–94 (2018).

147. Fujita, M. *et al.* Structural study on gold nanoparticle functionalized with DNA and its non-cross-linking aggregation. *J. Colloid Interface Sci.* **368**, 629–635 (2012).

148. Wang, G., Akiyama, Y., Takarada, T. & Maeda, M. Rapid Non-Crosslinking Aggregation of DNA-Functionalized Gold Nanorods and Nanotriangles for Colorimetric Single-Nucleotide Discrimination. *Chem. - A Eur. J.* **22**, 258–263 (2016).

149. Lee, J.-S., Han, M. S. & Mirkin, C. A. Colorimetric Detection of Mercuric Ion (Hg2+) in Aqueous Media using DNA-Functionalized Gold Nanoparticles. *Angew. Chemie Int. Ed.* **46**, 4093–4096 (2007).

150. Retout, M. *et al.* Rapid and Selective Detection of Proteins by Dual Trapping Using Gold Nanoparticles Functionalized with Peptide Aptamers. *ACS Sensors* **1**, 929–933 (2016).

151. Chang, C. C., Wang, G., Takarada, T. & Maeda, M. Target-recycling-Amplified colorimetric detection of pollen allergen using non-cross-linking aggregation of dna-modified gold nanoparticles. *ACS Sensors* **4**, 363–369 (2019).

152. McVey, C., Huang, F., Elliott, C. & Cao, C. Endonuclease controlled aggregation of gold nanoparticles for the ultrasensitive detection of pathogenic bacterial DNA. *Biosens. Bioelectron.* **92**, 502–508 (2017).

153. Chiu, T.-C. & Huang, C.-C. Aptamer-Functionalized Nano-Biosensors. *Sensors* **9**, 10356–10388 (2009).

154. De La Rica, R. & Stevens, M. M. Plasmonic ELISA for the ultrasensitive detection of disease biomarkers with the naked eye. *Nat. Nanotechnol.* **7**, 821–824 (2012).

155. Zhou, Y. & Ma, Z. Colorimetric detection of Hg2+by Au nanoparticles formed by H2O2reduction of HAuCl4using Au nanoclusters as the catalyst. *Sensors Actuators, B Chem.* **241**, 1063–1068 (2017).

156. Plasmonic colorimetric sensors based on etching and growth of noble metal nanoparticles: Strategies and applications - ScienceDirect. Available at: https://www-sciencedirect-com.biblio.iit.it/science/article/pii/S0956566318303567. (Accessed: 7th February 2021)

157. Rao, H., Xue, X., Wang, H. & Xue, Z. Gold nanorod etching-based multicolorimetric sensors: Strategies and applications. *Journal of Materials Chemistry C* **7**, 4610–4621 (2019).

158. Ma, X. *et al.* A universal multicolor immunosensor for semiquantitative visual detection of biomarkers with the naked eyes. *Biosens. Bioelectron.* **87**, 122–128 (2017).

159. Zhang, Z., Chen, Z. & Chen, L. Ultrasensitive Visual Sensing of Molybdate Based on Enzymatic-like Etching of Gold Nanorods. *Langmuir* **31**, 9253–9259 (2015).

160. Weng, G., Dong, X., Li, J. & Zhao, J. Halide ions can trigger the oxidative etching of gold nanorods with the iodide ions being the most efficient. *J. Mater. Sci.* **51**, 7678–7690 (2016).

161. Jiang, C. *et al.* Chitosan-gold nanoparticles as peroxidase mimic and their application in glucose detection in serum. *RSC Adv.* **7**, 44463–44469 (2017).

162. Han, K. N., Choi, J. S. & Kwon, J. Gold nanozyme-based paper chip for colorimetric detection of mercury ions. *Sci. Rep.* **7**, 1–7 (2017).

163. Wu, Y. *et al.* Accelerating peroxidase-like activity of gold nanozymes using purine derivatives and its application for monitoring of occult blood in urine. *Sensors Actuators, B Chem.* **270**, 443–451 (2018).

164. Shah, J., Purohit, R., Singh, R., Karakoti, A. S. & Singh, S. ATP-enhanced peroxidase-like activity of gold nanoparticles. *J. Colloid Interface Sci.* **456**, 100–107 (2015).

2 Gold nanoparticles noncatalytic/ nanoplasmonic based sensor for organic mercury detection

2.1 Introduction to colorimetric mercury species detection methods

Nowadays, the detection and quantification of mercury species (Hg^{2+}, $MeHg^{+}$) are done by using Inductively Coupled Plasma spectrometry (ICP-MS)[1–3], Atomic Fluorescence Spectrometry, Cold Vapor Atomic Absorption spectroscopy (CVAAS), Cold Vapor Atomic Fluorescence spectroscopy (CVAFS)[4,5], High Performance Liquid Chromatography (HPLC) and Gas Chromatography (GC). However, these techniques, even if highly sensitive, are expensive, as they require complex and costly instrumentation, laborious protocols and qualified personnel. Therefore, there is a strong need of portable and easy-to-use devices for the simple and rapid home testing of these threating pollutants. Harvesting the potential recently opened by the application of nanoparticles to analytic issues, several colorimetric nanosensors have been recently proposed for naked-eye detection of mercury[6,7]. However, the sensitivity and reliability are still a major challenge for routine monitoring application. Moreover, only few reports deal with the detection of organic mercury[8], which is the most abundant and dangerous species in fish flesh.

In the field of nanosensors for diagnostic and environmental control, AuNPs have been exploited to develop different detection strategies [9]. In particular, there are several reports regarding mercury species detection via optical read out approaches [10–12]. Many of them are based on the AuNPs color shift (related to the nanoparticles surface plasmon resonance), caused by the analyte-induced aggregation. Other studies are focused on the catalytic properties of nanoparticles that are affected by the presence of mercury and can be then further quantitatively transduced in a signal employing chromogenic or fluorescent

substrates[13,14]. To improve as possible the efficiency and the selectivity of analyte recognition step, those nanomaterials are usually functionalized with ssDNA, surfactants, thiols and other ligands[15]. While for inorganic mercury some colorimetric detection strategies have been recently reported due to the possible exploitation of Hg^{2+} reactivity and direct interaction with noble metal NPs, such as gold and platinum[16], detection of methylmercury was hampered to date in POC schemes because of its challenging reduction to its metallic form via simple and biocompatible reagents and methods. This prevented the implementation of portable colorimetric methods, since organic forms cannot directly interact with nanoparticles or chromogenic substrates. In a recent study[15], a colorimetric strategy for organic Hg has been achieved using a combination of AuNPs, copper ions, diethyldithiocarbamate (DDTC), and EDTA in a multi-step reaction, exploiting the Hg/Cu displacement in DDTC complex, with its consequent surface interaction and destabilization of the AuNPs. Moreover, in a different work[17], a strong reducing agent 4-(2-Hydroxyethyl)piperazine-1-(2-hydroxypropanesulfonic acid) monohydrate (HEPPSO) has been employed in an interesting and sensitive strategy to convert organic mercury to Hg^0, which inhibits the dual chromogenic functionality of HEPPSO. This latter approach, however, showed some limitations as a POC sensor, in terms of long operational procedure and use of strong reagents. Other approaches, which rely on the use of thymine-rich aptamers coupled to AgNPs, , need for controlled temperature cycles, or instrumental fluorescence detection[12,18], together with long reaction times. Similarly, thymine-functionalized AuNPs have been exploited in a Hg-induced cross-linking configuration, although reaching low sensitivity[8]. The characteristics of the main methods have been summarized in **Table 2.1**. Here, we demonstrate how citrate-capped gold Au NPs can be effectively used to detect both inorganic and organic mercury species exploiting simultaneously their catalytic and plasmonic properties. This method consists in an aggregation reaction induced by the formation of Hg^0 amalgam on particles surface as a consequence of mercury species reduction catalyzed by the AuNPs. Without adding any functional groups on the surface of the nanomaterial, we can reach remarkable limit of detection

(LOD) equal to 2 µM, while color change associated with the aggregation process is complete in less than 2 minutes.

Authors	Organic mercury	Visual detection	POC method	One-step reaction
Chi-Wei Liu et al.[19]	✗	✓	✗	✗
Huang Chih-Ching [20]	✗	✗	✗	✓
Chen Guan-Hua [21]	✗	✓	✓	✗
Chansuvarn Woravith [7]	✗	✓	✓	✗
Chen Yinji [10]	✗	✓	✓	✗
Danlian Huang [22]	✗	✓	✗	✓
Li Xiaokun [23]	✓	✓	✗	✗
Ling Chen [24]	✓	✓	✗	✗
Zhiqiang Chen[11]	✓	✓	✗	✗
Margaret L. Aulsebrook [8]	✓	✓	✗	✗
This work	✓	✓	✓	✓

Table 2.1 Analysis of the characteristics of the main methods for organic mercury detection, together with selected methods detecting inorganic mercury.

2.2 Materials and methods

All chemicals and reagents employed were of high technical grade, stored following vendor recommendations and directly used with no further purification. Hydroxylamine sulfate ($H_3NO•0.5H_2SO_4$, 88944) and Hydrogen Tetrachloroaurate ($HAuCl_4*XH_2O$, Au 49% min, 42803) were purchased from Alfa Aesar. Sodium citrate tribasic hydrate ($HOC(COONa)(CH_2COONa)_2$, Reagent Plus®, ≥99%, 25114 was purchased from Sigma-Aldrich.

2.2.1 Synthesis of AuNPs

Colloidal 15 nm citrate-capped AuNPs were synthesized by the classical Turkevich–Frens method[25] using sodium citrate as the reducing agent. All glassware was washed with aqua regia (HCl and HNO_3, in a 3:1 volumetric ratio). 75 mL of 0.25 mM acqueous solution of $HAuCl_4$ was added in a two-neck round-bottom flask, connected to a bulb condenser and. After reaching boiling point (using silicon oil as heating fluid, setting the temperature at 110°C), 1.4 mL of 1% aqueous solution of trisodium citrate were added. The solution was kept gently boiling for 25 min.

In a second step, 35 nm citrate capped AuNPs were synthetized according to a previously published method[26]. Briefly, the procedure relies on a seed-mediated growth using the 15 nm AuNPs (seeds) and NH_2OH, which efficiently reduces Au^{3+} in presence of Au surface. To determine the volume of seeds required, a preliminary calibrating synthesis is performed for the desired final particle size. 1 mL of 15 nm Au seeds solution were diluted in a round-bottom flask, under vigorous stirring and at room temperature, into 60 mL of MilliQ water, followed by the adding of 200 µL of 100 mM hydroxylamine sulfate solution. Then, 5 mL of $HAuCl_4$ 2 mM were added at 90 ml/h by syringe pump. After the addition of $HAuCl_4$, 1.3 mL of 100 mM trisodium citrate were added, to stabilize gold nanoparticles. Unreacted reagents were removed by centrifugation in 50 mL polycarbonate tube at 3800 rcf, for 25 minutes. Concentrated AuNPs batch was collected and stored at 4°C, until the use.

2.2.2 UV-vis characterization

In a 1.5 mL tube, 10 µL of a solution containing various concentrations (2.5-20 nM) of 35 nm AuNPs were added to 990 µL of an aqueous sample spiked with CH_3Hg^+. The mixture was then shacked and incubated with 3% v/v formic acid (50-1000 mM). Typically, the reaction started in 30 seconds and the color change was complete in a minute. UV-vis spectra (400-800 nm) were acquired by a NanoDrop®

(Thermo Fisher) with a small volume cuvette or by Spark® multimode microplate reader (Tecan) with flat transparent 96 multiwell plate.

2.2.3 TEM imaging

The TEM images of AuNPs deposited on carbon coated grids were acquired by a JEOL JEM 1400 microscope.

2.2.4 X-ray Photoelectron Spectroscopy (XPS) analyses

The XPS analyses were carried out with a Kratos Axis Ultra spectrometer, using a monochromatic Al Kα source, operated at 20 mA and 15 kV. The sample for XPS characterization was prepared by drop casting a few microliters of a 100-fold concentrated solution of a spiked sample containing $MeHg^+$ (100μM), AuNPs (20nM), and formic acid (150 mM) on a freshly cleaved highly oriented pyrolytic graphite (HOPG) substrate (NT-MDT, ZYB). Wide scan analyses were carried out with an analysis area of 300 x 700 microns and a pass energy of 160 eV. High resolution analyses were carried out with the same analysis area at a pass energy of 10 eV. Spectra were analysed using Casa XPS software (version 2.3.17).

2.2.5 NMR characterization

All the NMR experiments were performed at 298 K on a Bruker Ultrashield Plus FT-NMR 600 MHz ADVANCE III equipped with a CryoprobeTM QCI 1H/19F–13C/15N–D and with a SampleJetTM autosampler with temperature control. For each sample, a 1D 1H NMR spectrum was recorded; the water suppression was obtained using a standard pulse sequence (NOESY presat; Bruker) with 64 k data points, a spectral width of 20 ppm, an acquisition time of 2.7 s, a relaxation delay of 4s and a mixing time of 100 μs.

2.3 Results

2.3.1 Sensing strategy

The oxidation or reduction of heavy metal inorganic and organic compounds has been seldomly used for the development of nanosensors since the kinetics of these reactions can be extremely slow without the addition of a strong reducing or oxidizing agent that adversely interferes with the determination of the substance. This has been overcome in the paper published by my mentor's laboratory by using the catalytic surface properties of AuNPs, able to effectively harness the weak reducing ability of formic acid to obtain the reduction of methylmercury to elemental mercury on the nanomaterial interface. The reaction between formic acid and methylmercury is catalysed at the surface of the gold nanomaterial and leads to the reduction of methylmercury and to the formation of a layer of metallic mercury on the surface of Au NPs. This results in a modification of the AuNPs colloidal dispersion and, as a consequence, in a change of the AuNPs plasmonic properties. Indeed, the mixture loses the red colour of a stable colloidal AuNPs solution and becomes blue/violet as AuNPs get closer to each other and aggregate with the consequent modification of their plasmonic properties detected by naked eye (**Figure 2.1**). This mechanism based on the catalytic and plasmonic properties of AuNPs permits to drastically improve the sensitivity of the nanosensor, reaching the level required by the law.

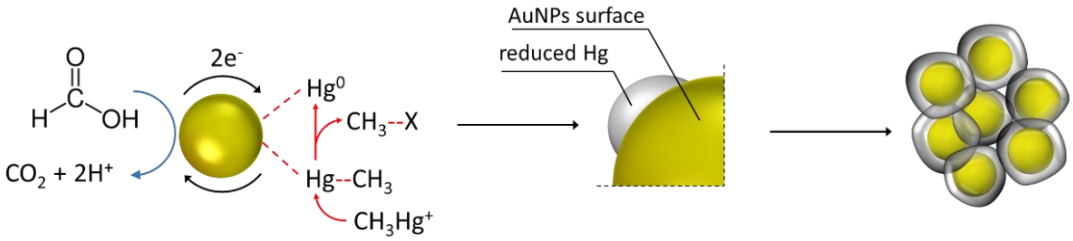

Figure 2.1 Detection mechanism triggered by the Red-Ox reaction at the surface of AuNPs between formic acid and methylmercury. As soon as reduced elemental mercury (Hg0) nucleates on AuNPs surface, fast particle aggregation is observed, with clear red-to-violet color change of the solution.

2.3.2 AuNPs characterization

The first step was the AuNPs synthesis: as previously described (paragraph 2.2.1), citrate-capped 15 nm AuNPs have been produced and then used as seeds in a further growing reaction to obtain 35 nm AuNPs. Both 15 and 35 nm nanoparticles have been characterized in size and shape. The results are shown below (see **Figure 2.2** and **Figure 2.3**). The method allowed to obtain well monodispersed, spherical AuNPs. The UV-vis spectra reports a maximum of absorbance at $\lambda = 520$ nm peculiar of 15 nm spherical nanoparticles, according to AuNPs plasmonic theory (see **Figure 2.2 (A)**) and the DLS analysis report a narrow peak (Z-Ave = 15.2 nm) without side population of aggregates (see **Figure 2.2 (B)**). In the **Figure 2.2 (C)** the size distribution calculated on statistical significative population of particles on TEM images (see **Figure 2.2 (B)**).

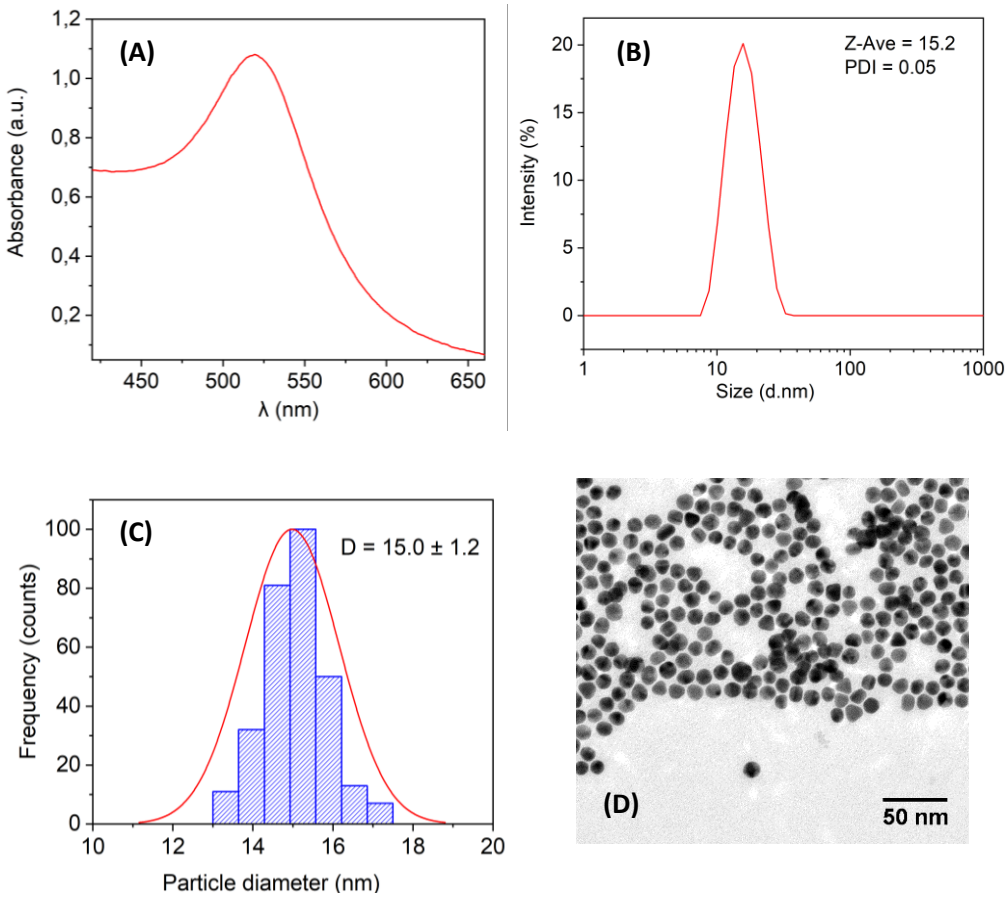

Figure 2.2 15 nm AuNPs characterization **(A)** UV-vis absorption spectrum in water, **(B)** DLS measurement **(C)** TEM size distribution analysis showing a monodisperse population with an average size of 15 nm, **(D)** representative TEM micrograph.

The same characterization in terms of size distribution and stability has been performed for 35 nm citrate capped AuNPs. The **Figure 2.3 (A)** shows the UV-vis absorption spectra with $\lambda max = 525$ nm according to plasmonic theory. The DLs analysis confirm the particles size with one peak at Z-Ave = 36 nm (see **Figure 2.3 (B)**). In **Figure 2.3 (C)** has been reported the distribution of the diameters measured on statistical significative sample of particles after TME images acquiring (see **Figure 2.3 (D)**).

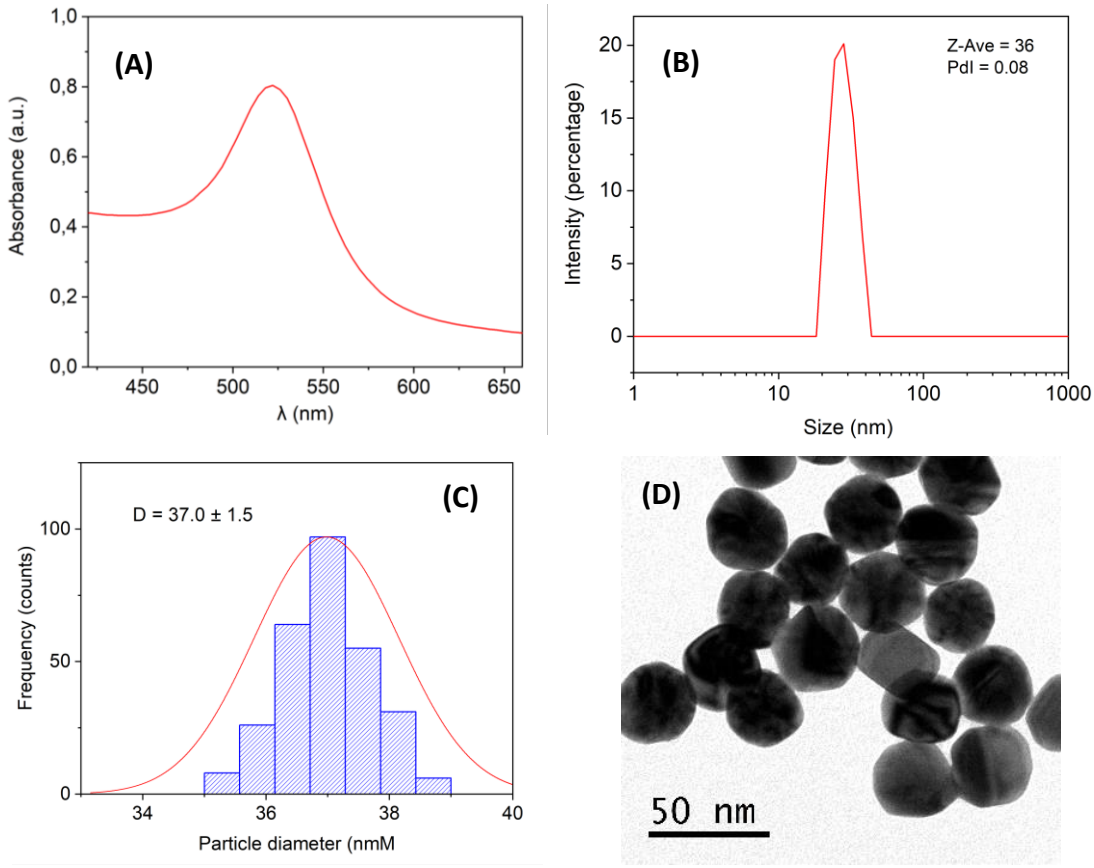

Figure 2.3 35 nm AuNPs characterization **(A)** UV-vis absorption spectrum in water, **(B)** DLS measurement **(C)** TEM size distribution analysis showing a monodisperse population with an average size of 35 nm, **(D)** representative TEM micrograph.

2.3.3 NMR characterization

The proposed sensing scheme and its underlying reactions were characterized by nuclear magnetic resonance (NMR), transmission electron microscopy (TEM), X-ray photoelectron spectroscopy (XPS), and absorption spectroscopy (UV-vis). First, to confirm the role of the AuNP as catalyst for the $MeHg^{+}$ reduction, 1^{H} NMR spectra have been acquired during the reaction. A sharp signal around 0.9 ppm represents the aqueous solution containing methylmercury (**Figure 2.4 a**)[27,28]. As expected, the addition of formic acid did not elicit any detectable change in the spectrum, as such weak reductants are not able to reduce methylmercury (**Figure 2.4 b**)[27,29,30]. Even after several days of incubation, we did not observe any appreciable signal reduction. As a control, we also verified that AuNPs alone did

not cause any significant effect (see **Figure 2.4 c**). Noteworthy, in presence of both AuNPs and formic acid, a significant decrease in the signal of methylmercury was visible already after few minutes, indicative of the strong activity of the nanocatalyst (see **Figure 2.4 d**). In the same spectrum, the 1H NMR signal of the methane produced during the reaction is also visible, while no methane signals can be observed in the spectra acquired without AuNPs or formic acid (red asterisks).

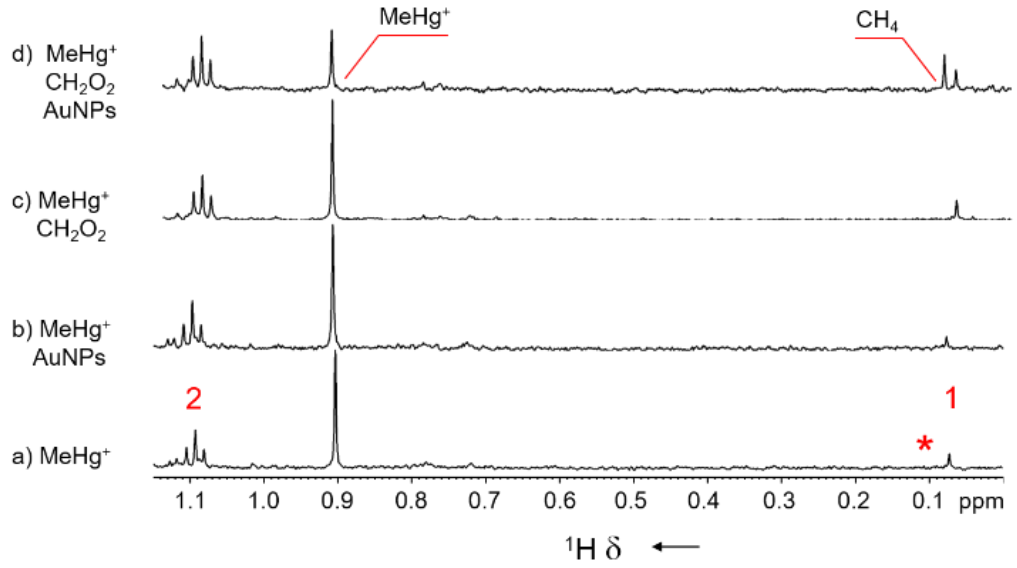

Figure 2.4 Expansion regions between 1 and 0 ppm of the 1D ^{1}H spectra recorded for **(a)** methylmercury ($MeHg^{+}$) in water; **(b)** in presence of formic acid; **(c)** in presence of AuNPs; **(d)** in presence of both AuNPs and formic acid. **1** and **2** indicate the NMR signals of some impurities present in all the samples. Red asterisks indicate the absence of methane signals

Therefore, the gold nanocatalyst is crucial for the reaction to happen, allowing fast organic mercury conversion to its metallic form. To further investigate the AuNPs catalytic activity, increasing concentrations of NPs have been tested (see **Figure 2.5**). Going from a concentration of AuNPs of 78 pM to one of 468 pM, the NMR analysis show a complete CH_3Hg^{+} conversion.

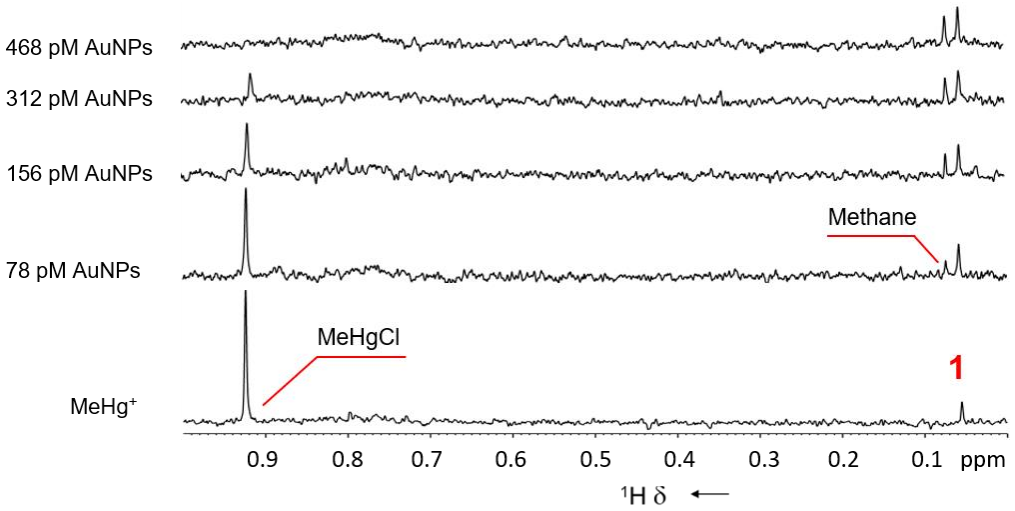

Figure 2.5 Expansion regions between 1 and 0 ppm of the 1D ^{1}H spectra recorded for 50 μM CH_3Hg^+ in MilliQ 50% D_2O, 200 μM citric acid and 50 mM formic acid (bottom line) and after the addition of increasing concentrations of AuNPs (78-468 pM). The ^{1}H NMR signal of $MeHg^+$ clearly decreases, as a function of increasing Au-NP concentration. At the highest particle concentration, the reaction is complete (*).

2.3.4 XPS characterization

To verify the presence of metallic mercury on the surface of AuNPs, XPS measurements were performed on the particles after incubation with methylmercury. **Figure 2.6** shows the XPS data collected over the binding energy typical for Au 4f and Hg 4f peaks. Each Au 4f (Hg 4f) level is represented by a doublet, due to spin-orbit coupling, showing an intensity ratio of 4:3 between the 7/2 and 5/2 components and a doublet splitting of 3.67 eV (4.05 eV)[31]. The oxidation state of both Au and Hg could be estimated by evaluating the position of their 4f7/2 components. Au 4f7/2 and Hg 4f7/2 were found at a binding energy of (83.9±0.2)eV and (99.6±0.2)eV, respectively, indicating that both Au and Hg are present in their metallic state in the sample[31]. By calculating the Hg and Au peak areas and after normalization to the corresponding relative sensitivity factors (parameters that can be related to the cross section of the X-ray induced photoemission process), the Au:Hg atomic ratio was calculated to be 90.4:9.6. ± 0.5. These data indicate the presence of metallic mercury on the AuNP surface, in agreement with the sensing scheme described in **Figure 2.1**.

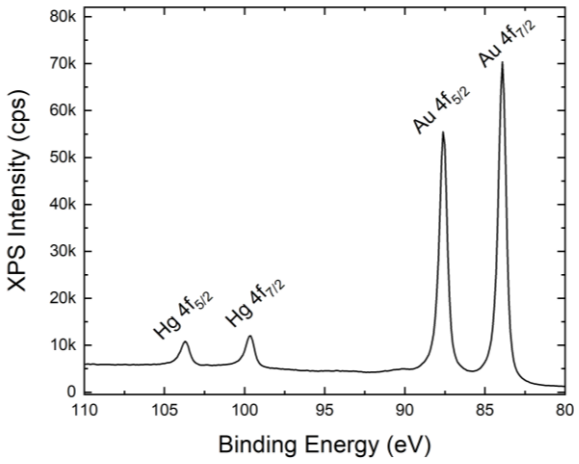

Figure 2.6 High resolution XPS spectrum showing the Au 4f and Hg 4f peaks. The position of the XPS peaks indicates that both Au and Hg are present in the sample in their metallic state.

2.3.5 TEM characterization

TEM images were then acquired on the AuNPs before and after the detection reaction with methylmercury. Unlike the pristine status of AuNPs in the initial state characterized by separated particles on the grid (see **Figure 2.7 A,B**), the formation of mercury amalgam is clearly evident after methylmercury incubation, with the presence of large particle aggregates fused together (see **Figure 2.7 C,D**). This envisages possible color change of the AuNP solution, due to aggregation-induced plasmon shift. TEM images clearly show the aggregation process: while before the assay the AuNPs are well monodispersed, after the catalyzed organic mercury reduction, the nanoparticles appear densely aggregated as a result of mercury amalgam formation.

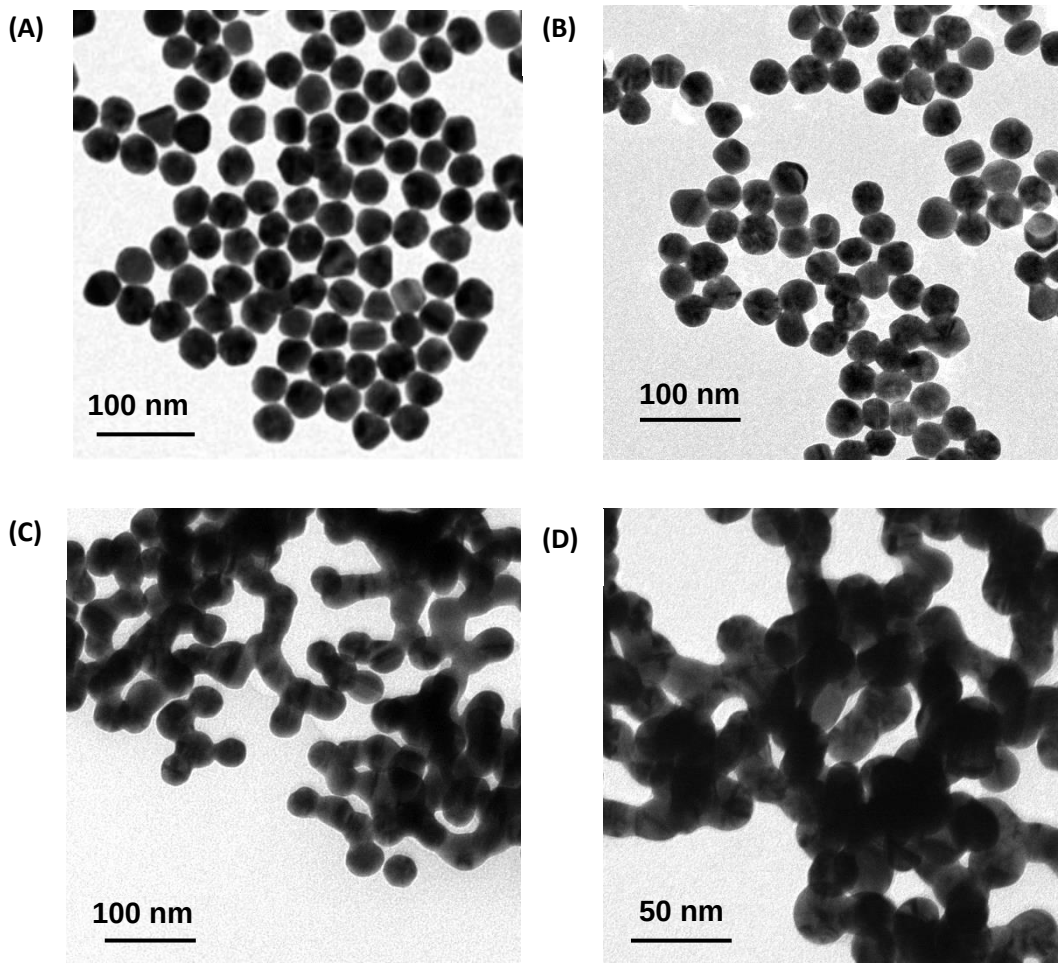

Figure 2.7 Representative TEM images of AuNPs before **(A,B)** and after **(C,D)** the incubation with a spiked sample containing methylmercury.

2.3.6 UV-vis characterization

The spectral response of our colorimetric test was characterized by UV-vis spectroscopy (see **Figure 2.8**). A fast and constant decrease of the plasmon band around 520 nm, ascribed to monodispersed AuNPs, and a related increase of a broad absorbance of aggregate population (650-780 nm) were clearly observed, in line with TEM data. Interestingly, the process was complete in less than 2 minutes, reaching a remarkable 750nm/620nm absorbance ratio already after 1 minute.

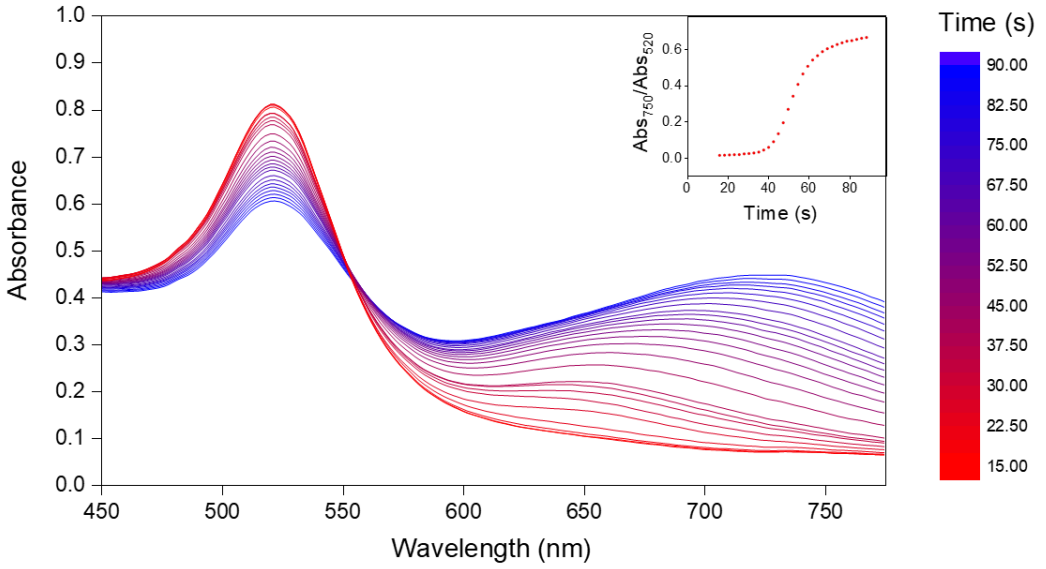

Figure 2.8 Time-dependent absorption spectra of AuNPs (200 pM) upon incubation with methylmercury (0.2 ppm) in presence of formic acid. A very fast aggregation process can be observed in 1 minute, with a clear colour change of the solution, in the inset graph the aggregation rate as Abs_{750}/Abs_{520}.

Noteworthy, the colorimetric test can be also assessed by simple visual inspection. As reported in **Figure 2.9 A**, the red-to-violet color change elicited by the presence of methylmercury could be clearly observed after only 1 minute of incubation, even in the case of low levels of contamination. After systematic optimization, the Limit-Of-Detection (LOD) of our assay by naked-eye was found to be around 0.1 ppm. This is important in view of real applications to food contaminations (e.g. on fish samples), where the exposure limit is 0.5-1.0 ppm mercury (depending on the food species). Moreover, since real samples from water to food extracts might contain various metallic cations that can interfere with the detection of CH_3Hg^+ giving false positive signals, the selectivity of proposed method was assessed against different ions, tested at high concentration (i.e. 1 ppm, that is 10-fold our LOD). As shown in **Figure 2.9 A**, only mercury contamination elicited a significant increase of 750nm/620nm absorbance ratio, which corresponds to a clear color change, while the other analyzed cations did not produce any significant spectral change. The test selectivity is due to the specific affinity of reduced mercury with AuNPs, resulting in Au-Hg amalgam system, unlike other cations.

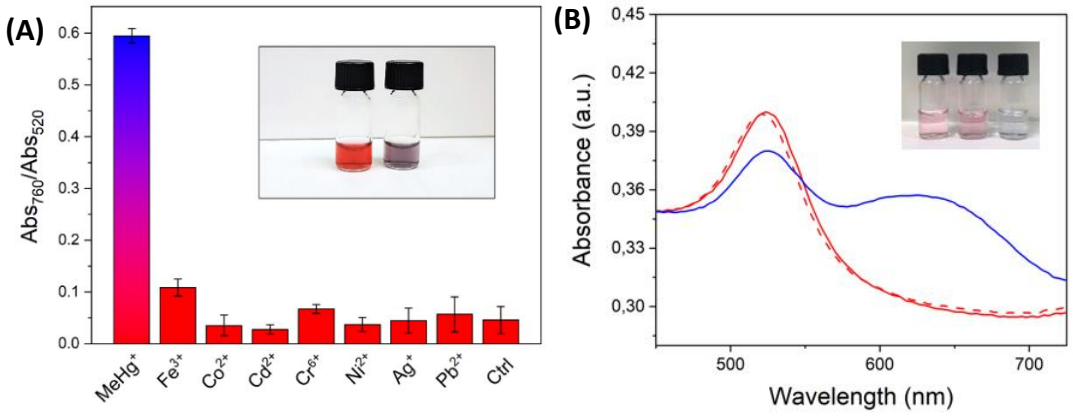

Figure 2.9 (A) Selectivity of presented method versus other toxic metallic cations, in terms of absorbance ratio measured at the end point of aggregation kinetic (after 180 sec). The results are expressed as mean ± SD of triplicate experiments. **(B)** efficiency and selectivity of the nanosensor in presence of high concentrations of interfering cations ($Fe3^{+}$), using PVP-AuNPs. Absorption spectra of 35 pM AuNPs before (red line) and after (dashed red line) incubation with 100-fold excess of $Fe3^{+}$ (12,5 ppm), and subsequent incubation (blue line) with methylmercury (125 ppb). Representative photograph of the naked-eye colorimetric response (inset).

2.3.7 Real samples testing

As a consequence of samples complexity (e.g. high concentration of solutes and ionic strength) AuNPs requires further stabilization to avoid unspecific aggregation. Several polymers are tested as stabilizing agent. Specifically, a picomolar solution of AuNPs has been incubated overnight under stirring with different concentrations of Polyvinylpyrrolidone (PVP), Polyacrylic acid (PAA) and Polyethylene glycol (PEG). After being washed, the particles stability is evaluated monitoring the plasmon shifting over the time in presence of different concentrations of sodium chloride (NaCl) (see **Figure 2.10**). PVP-stabilized AuNPs showed remarkable performance in real biological samples, like urine, where this sensor can detect low concentration of methylmercury, spiked in the sample. The nanosensor performance properly maintained its efficiency and selectivity even in case of complex real sample like human urine (see **Figure 2.11 B**).

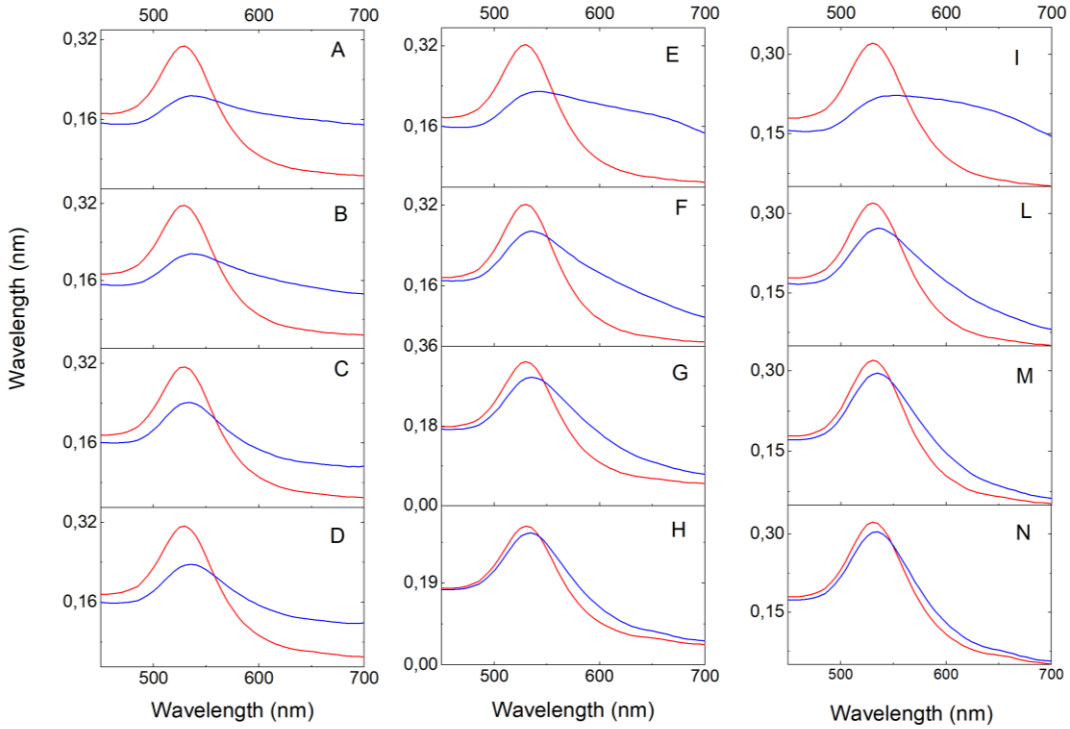

Figure 2.10 (A-D) Absorption spectra of PAA-coated AuNPs, **(E-H)** Absorption spectra of PEG-coated AuNPs, **(I-N)** Absorption spectra of PVP-coated AuNPs. PVP 10K results to be the best stabilizing agent on mercury sensing conditions.

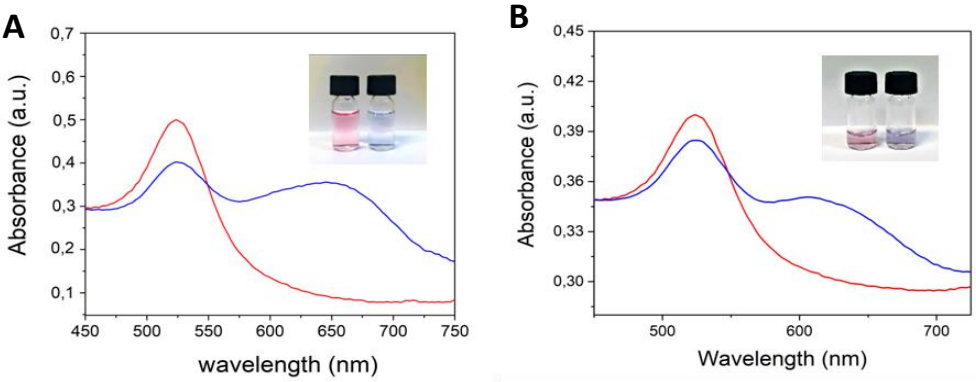

Figure 2.11 (A) Absorption spectra of the colorimetric nanosensor using PVP-coated AuNPs. The spectral analysis was performed with 30 pM AuNPs before (red line) and after (blue line) 1-minute incubation with methylmercury (25 ppb) and formic acid. **(B)** PVP-AuNPs based nanosensor in human urine collected and spiked with methylmercury and left to equilibrate.

2.4 Conclusions

Here, we exploit the interesting property of AuNPs to efficiently catalyze the fast transformation of methylmercury in the Hg^0 form, even in presence of a weak and biocompatible reducer, such as formic acid. The potential of nanocatalysts to promote reduction of organic mercury in absence of strong reducers has been previously reported in photocatalysis with titania NPs, and in case of electrocatalysis with AuNP-functionalized electrode. In our strategy, such process allows quasi-simultaneous metallic mercury nucleation on the AuNP surface and amalgam formation, with prompt particle destabilization and aggregation. Thus, the coupled catalytic/plasmonic functionality of AuNPs allows for ultrafast and specific naked-eye detection of organic mercury at relevant concentrations, due to metal-induced shift of the plasmonic band. These results open interesting perspectives for the development of low-cost, rapid, and portable sensors, enabling frequent screening of organic mercury contaminations, which represents an important option for routine food assessment, as well as for health and environmental protection. Interestingly, the overall reaction that leads to the fast and sensitive detection of organic mercury can be performed at ambient conditions, with stable and "green" reagents, thus opening promising perspectives toward frequent mercury screening by point-of-care devices. In particular, the possibility to use biocompatible and weak reducing agents, such as formic acid, is enabled by the action of the surface of gold nanocatalyst, as clearly proven by the NMR analysis. Indeed, in such sensing scheme, the use of stronger reductants (e.g. sodium borohydride) is hampered by immediate AuNP destabilization and loss of assay sensitivity and specificity. This makes the interplay of the nanocatalyst/nanoplasmonic activities and reactants strength unique. Considering that this detection protocol can be easily monitored by naked-eye, and that it has high selectivity and short reaction time, the method has been patented (n° 102018000008034 date: 10/08/2018). The presented results are published as Nanocatalyst/Nanoplasmon-Enabled Detection of Organic Mercury: A One-Minute Visual Test Donati P. et al.[32]

2.5 Bibliography

1 Yao, C.-H., Jiang, S.-J., Sahayam, A. C. & Huang, Y.-L. Speciation of mercury in fish oils using liquid chromatography inductively coupled plasma mass spectrometry. Microchem. J. 133, 556–560 (2017).

2. Rodrigues, J. L., de Souza, S. S., de Oliveira Souza, V. C. & Barbosa, F. Methylmercury and inorganic mercury determination in blood by using liquid chromatography with inductively coupled plasma mass spectrometry and a fast sample preparation procedure. Talanta 80, 1158–1163 (2010).

3. Hight, S. C. & Cheng, J. Determination of methylmercury and estimation of total mercury in seafood using high performance liquid chromatography (HPLC) and inductively coupled plasma-mass spectrometry (ICP-MS): Method development and validation. Anal. Chim. Acta 567, 160–172 (2006).

4. Aranda, P. R., Gil, R. A., Moyano, S., De Vito, I. & Martinez, L. D. Slurry sampling in serum blood for mercury determination by CV-AFS. J. Hazard. Mater. 161, 1399–1403 (2009).

5. Li, X. & Wang, Z. Determination of mercury by intermittent flow electrochemical cold vapor generation coupled to atomic fluorescence spectrometry. Anal. Chim. Acta 588, 179–183 (2007).

6. Lou, T., Chen, Z., Wang, Y. & Chen, L. Blue-to-Red Colorimetric Sensing Strategy for Hg 2+ and Ag + via Redox-Regulated Surface Chemistry of Gold Nanoparticles. ACS Appl. Mater. Interfaces 3, 1568–1573 (2011).

7. Chansuvarn, W. & Imyim, A. Visual and colorimetric detection of mercury(II) ion using gold nanoparticles stabilized with a dithia-diaza ligand. Microchim. Acta 176, 57–64 (2012).

8. Aulsebrook, M. L., Watkins, E., Grace, M. R., Graham, B. & Tuck, K. L. Modified Gold Nanoparticles for the Temperature-Dependent Colorimetric Detection of Mercury and Methylmercury. ChemistrySelect 3, 2088–2091 (2018).

9. Priyadarshini, E. & Pradhan, N. Gold nanoparticles as efficient sensors in colorimetric detection of toxic metal ions: A review. Sensors Actuators B Chem. 238, 888–902 (2017).

10. Chen, Y. et al. Rapid and ultrasensitive colorimetric detection of mercury(II) by chemical initiated aggregation of gold nanoparticles. Microchim. Acta (2015) doi:10.1007/s00604-015-1538-0.

11. Chen, Z. et al. Specifically and Visually Detect Methyl-Mercury and Ethyl-Mercury in Fish Sample Based on DNA-Templated Alloy Ag-Au Nanoparticles. Anal. Chem. 90, 5489–5495 (2018).

12. Chen, Z. et al. Specifically and Visually Detect Methyl-Mercury and Ethyl-Mercury in Fish Sample Based on DNA-Templated Alloy Ag–Au Nanoparticles. Anal. Chem. 90, 5489–5495 (2018).

13. Han, K. N., Choi, J. S. & Kwon, J. Gold nanozyme-based paper chip for colorimetric detection of mercury ions. Sci. Rep. 7, 1–7 (2017).

14. Peng, C.-F., Zhang, Y.-Y., Wang, L.-Y., Jin, Z.-Y. & Shao, G. Colorimetric assay for the simultaneous detection of Hg 2+ and Ag + based on inhibiting the peroxidase-like activity of core–shell Au@Pt nanoparticles. Anal. Methods 9, 4363–4370 (2017).

15. Chen, L., Li, J. & Chen, L. Colorimetric Detection of Mercury Species Based on Functionalized Gold Nanoparticles. ACS Appl. Mater. Interfaces 6, 15897–15904 (2014).

16. Ojea-Jiménez, I., López, X., Arbiol, J. & Puntes, V. Citrate-coated gold nanoparticles as smart scavengers for mercury(II) removal from polluted waters. ACS Nano 6, 2253–2260 (2012).

17. Li, X. et al. Catalysis-reduction strategy for sensing inorganic and organic mercury based on gold nanoparticles. Biosens. Bioelectron. 92, 328–334 (2017).

18. Deng, L. et al. Ultrasensitive and Highly Selective Detection of Bioaccumulation of Methyl-Mercury in Fish Samples via Ag 0 /Hg 0 Amalgamation. Anal. Chem. 87, 2452–2458 (2015).

19. Liu, C.-W., Hsieh, Y.-T., Huang, C.-C., Lin, Z.-H. & Chang, H.-T. Detection of mercury(ii) based on Hg2+–DNA complexes inducing the aggregation of gold nanoparticles. Chem. Commun. 2242 (2008) doi:10.1039/b719856f.

20. Huang, C.-C., Yang, Z., Lee, K.-H. & Chang, H.-T. Synthesis of Highly Fluorescent Gold Nanoparticles for Sensing Mercury(II). Angew. Chemie Int. Ed. 46, 6824–6828 (2007).

21. Chen, G.-H. et al. Detection of Mercury(II) Ions Using Colorimetric Gold Nanoparticles on Paper-Based Analytical Devices. Anal. Chem. 86, 6843–6849 (2014).

22. Huang, D. et al. Colorimetric determination of mercury(II) using gold nanoparticles and double ligand exchange. doi:10.1007/s00604-018-3126-6.

23. Li, X. et al. Catalysis-reduction strategy for sensing inorganic and organic mercury based on gold nanoparticles. Biosens. Bioelectron. 92, 328–334 (2017).

24. Chen, L., Li, J. & Chen, L. Colorimetric Detection of Mercury Species Based on Functionalized Gold Nanoparticles. ACS Appl. Mater. Interfaces 6, 15897–15904 (2014).

25. Turkevich, J., Stevenson, P. C. & Hillier, J. A study of the nucleation and growth processes in the synthesis of colloidal gold. Discussions of the Faraday Society vol. 11 55–75 (1951).

26. Pompa, P. P. et al. Physical assessment of toxicology at nanoscale: Nano dose-metrics and toxicity factor. Nanoscale 3, 2889–2897 (2011).

27. Wrackmeyer, B. & Contreras, R. 199Hg NMR Parameters. Annu. Reports NMR Spectrosc. 24, 267–329 (1992).

28. Granger, P. NMR of the elements Copper to Mercury. Stud. Inorg. Chem. 13, (1991).

29. Binev, Y. & Aires-de-Sousa, J. Structure-Based Predictions of 1 H NMR Chemical Shifts Using Feed-Forward Neural Networks. J. Chem. Inf. Comput. Sci. 44, 940–945 (2004).

30. Wrackmeyer, B. & Contreras, R. 199Hg NMR Parameters. Annu. Reports NMR Spectrosc. 24, 267–329 (1992).

31. NIST X-ray Photoelectron Spectroscopy (XPS) Database, Version 3.5. https://srdata.nist.gov/xps/.

32. Donati, P. et al. Nanocatalyst/Nanoplasmon-Enabled Detection of Organic Mercury: A One-Minute Visual Test. Angew. Chemie Int. Ed. 58, 10285–10289 (2019).

3 Nanoplasmonic gold nanoparticles-based sensor for salivary glucose assessment

3.1 Gold nanoparticles for glucose detection

Gold nanoparticles have been largely used in colorimetric sensing of variety of analytes, from DNA sequences to metal ions[1–4]. One of the most popular strategies is based on the controlled aggregation, in which a decreased distance between nearby particles results in a plasmon coupling effect and related band shift and consequent colour change[5,6]. Even if this approach exhibits great sensibility, it presents auto-aggregation problems due to the bio-chemical samples composition, that may lead to false results since high concentration of proteins, salts and others solutes, strongly affect the AuNPs stability. Moreover, the required engineering of nanoparticles with recognition probes can be expensive and time-consuming. Recently, a group of "non-aggregation" methods is drawing the attention of the scientific community. These strategies based on the nanoparticle etching and growth result in a plasmon band shifting as a consequence of the particles re-modelling, achieving a sensible detection of biomarkers, virus, ions[7]. Nevertheless, also the growth approach presents some limitations when used in complex media such as biological fluids, in which the solutes like proteins, small molecules or salts can inhibit the reaction on the particle surface[8,9]. An effective "non-aggregation" approach is based on the etching of metal nanoparticles. This strategy has been used to detect metal ions, anions, glucose and amino acids. We can mention several mechanisms, depending on the agent that triggers the particles' erosion: direct etching by targets, intermediate-mediated etching, alloy-promoted etching, enzyme-mediated etching. In the case of enzyme mediated etching, there are several published methods in which the hydrogen peroxide produced by the enzyme induces the oxidation of gold nanorods (AuNRs), resulting in a strong plasmon shifting[7,10,11]. However, the erosion step needs to be catalysed, and to obtain a clear colour

change, the AuNRs must be largely etched. These methods require strong conditions, long reaction times and lead to an obvious loss of optical density as a consequence of nanoparticles final reduced dimensions. A colorimetric assay for blood glucose determination using this mechanism was explored on gold nanorods and the colour change was obtained following the particle corrosion and shortening in presence of glucose[12]. In a similar work, the glucose oxidase (GOx) enzyme reacts specifically with glucose in complex media producing H_2O_2 that, via Fenton or Fenton-like reactions, transforms in the free radical form able to rapidly oxidize (and partially dissolve) the AuNPs[13,14].

Likewise, a gold nano-bipyramid has been used as probe to dose glucose, exploiting the interaction of hydrogen peroxide and halogen that results in particles shortening[11]. Yet, also this work shows the same limitations previously reported. Despite of the number of available methods, there is still a lack of suitable tools for a fast and sensitive visual detection of biomarker, like glucose, in real biological samples.

3.2 Materials and methods

3.2.1 Chemicals and materials

All chemicals and reagents employed were of high technical grade, stored following vendor recommendations and directly used with no further purification. Hydroxylamine sulfate ($H_3NO•0.5H_2SO_4$, 88944) and Hydrogen Tetrachloroaurate ($HAuCl_4*XH_2O$, Au 49% min, 42803) were purchased from Alfa Aesar. Sodium citrate tribasic hydrate ($HOC(COONa)(CH_2COONa)_2$, ReagentPlus®, ≥99%, 25114), HEPES (BioUltra, for molecular biology, ≥99.5%, 54457), Potassium bromide (KBr,EMSURE® ACS,Reag. 1.04905), Potassium chloride (KCl, EMSURE®,1.04936), Potassium iodide (KI, for analysis EMSURE® ISO,Reag, 1.05043), D-(+)-Glucose (C6H12O6 ACS reagen, G5767) and Glucose Oxidase from Aspergillus (Type X-S, lyophilized powder, G7141) were purchased from Sigma-Aldrich. Nylon membrane

filters (Whatman® pore size 0.45 µm, 13 mm Ø, thickness150-187 µm, WHA7404001**)**, Nitrocellulose membrane filters (Whatman® pore size 0.45 µm, 13 mm Ø, WHA7184001), PDVF Membrane filters (Millipore Durapore®, pore size 0.45 µm, hydrophilic, 13 mm Ø, HVLP01300) were purchased from Sigma-Aldrich. Syringe filter holder (re-usable polycarbonate, for 13 mm Ø filters, 0.5 cm^2 filtration area, 16514) were purchased from Sartorius. A high sensitivity glucose assay kit (Merck - MAK181-1KT) was employed as reference standard technique.
If not specified differently, all solutions and buffers were prepared using ultrapure deionized water (MilliQ). The saliva samples were spontaneously donated from healthy subjects and their use in this study was approved by Ethical Committee. Saliva samples from diabetic patients were provided by the San Matteo hospital of Pavia.

3.2.2 Synthesis of AuMBNPs

60 nm multibranched gold nanoparticles (AuMBNPs) were prepared by slightly modified Maiorano–Pompa method[19], optimized for our purposes. The procedure relied on a seed-mediated growth. Briefly, 6.5 mL of the prepared 15 nm gold seeds (1.8 nM), 0.28 mL of hydrogen tetrachloroaurate (100 mM) and 0.8 mL of hydroxylamine sulphate (100 mM) were consecutively added to 250 mL of HEPES solution (50 mM, pH = 7.0), under vigorous stirring. After 15-20 minutes at room temperature, the reaction mixture becomes blue. Residual reagents excess was removed by centrifugation (400 RCF, 25 min). AuMBNPs were characterized by DLS, UV-vis spectrophotometry and TEM.

3.2.3 UV-visible spectroscopy

UV-vis spectra (400-800 nm) of the nanoparticle suspension were acquired by a Thermo Fisher NanoDrop® (wavelength Accuracy ± 1 nm, absorbance accuracy 3 % at 0.74 Abs@350nm) with a small volume cuvette or by Tecan Spark® multimode

microplate reader (wavelength accuracy < 0.3 nm, absorbance accuracy < 0.5%@260) nm with flat transparent 96 multiwell plate.

3.2.4 Reflectance spectroscopy

Reflectance spectra were recorded on dried substrates using Ocean Optics spectrophotometer equipped with a reflection probe and an OCEAN-HDX-XR detector. For the white balance, a reflectance standard was employed (Diffuse Reflectance Std, Spectralon).

3.2.5 Optimization of pH conditions

Different acetate buffers (14 mM) were prepared varying the ratio between acetic acid and sodium acetate to obtain three solutions with pH 4.5, 5.0 and 5.5, respectively. 20 µL of AuMBNPs (0.5 nM, ALSPR = 0.8, $\varepsilon = 16.87 \times 10^9$ M-1cm-1), 20 µL of KBr (50 mM) and 20 µL of H_2O_2 (2.5 mM) were added to 140 µL of the different acetate buffer solutions (pH = 4.5, 5.0 and 5.5). Controls were performed in absence of H_2O_2 (replaced by 20 µL of H_2O). The experiment was performed in a 96-multiwell plate and absorption spectra were recorded at room temperature by Tecan plate reader to monitor the reaction over the time.

3.2.6 Halogen screening

Three halogen ion solutions were used at their “best” operational concentration (previously experimentally identified), since, due to their very different reactivity, employing them at the very same concentration would have not allowed for a fair comparison among their potential role in the sensing platform. KCl (500 mM), KBr (50 mM) and KI (50 µM) were the selected stock solutions used in this study. 20 µL

of AuMBNPs (0.5 nM, ALSPR = 8.0, ε = 16.87 × 10^9 M-1cm-1), 20 µL of acetate buffer (100 mM, pH = 5) and 20 µL of halogen stock solution were added to 140 µL of H_2O_2 (2.86 mM). H_2O_2 final concentration was 2 mM in the total volume.

3.2.7 Efficiency of hydrogen peroxide detection

Several sample solutions with different H_2O_2 concentrations were prepared (0, 0.71, 2.14, 3.57 and 4.29 mM). 20 µL of AuMBNPs (0.5 nM, ALSPR = 0.8, ε = 16,87 ×109 M-1cm-1), 20 µL of KBr (50 mM) and 20 µL of acetate buffer (100 mM, pH = 5) were added to 140 µL of the prepared H_2O_2 solutions (presenting, in the total volume, a final concentration of 0, 0.5, 1.5, 2.5 and 3 mM). The experiment was performed in a 96-multiwell plate and absorption spectra were recorded at room temperature by Tecan plate reader to monitor the reaction over time.

3.2.8 Optimization of the reshaping process in water

20 µL of AuMBNPs (0.5 nM, ALSPR = 0.8, ε = 16,87 ×10^9 M-1cm-1), 20 µL of KBr (50 mM) and 20 µL of acetate buffer (100 mM, pH = 5) were added to 140 µL of H_2O_2solution presenting, in the total volume, a final concentration of 3 mM.

3.2.9 Saliva sampling

The saliva samples were spontaneously donated from healthy subjects, and their use in this study was approved by Ethical Committee. Donors were asked to avoid eating, drinking and oral hygiene procedures for at least one hour before saliva collection. Furthermore, donors were asked to provide unstimulated saliva (no speaking or swallowing for one minute prior to collection). Samples were collected by the donor into a 15 mL sterile and protein lo-bind falcon tube. The tube was stored at 4 °C and processed within one hour from donation. The sensing platform

was conceived for self-monitoring of untreated whole saliva, however in this work we employed saliva samples from different donors and therefore, for safety reasons, samples were manipulated under the chemical hood and filtered (0.2 µm methyl cellulose syringe filter) from bacteria. Saliva samples from diabetic patients were provided by the San Matteo hospital of Pavia.

3.2.10 Salivary glucose assay in suspension

Hyperglycemia conditions were simulated by supplementing the collected saliva samples (see the saliva sampling section) with a glucose solution in order to reach pathological concentrations (2 mM, 36 mg/dL). Non-supplemented saliva representing physiological normal condition was used as a control. 20 µL of AuMBNPs (0.5 nM), 20 µL of GOx (0.021 mg/mL, 3 U/mL) in acetate buffer (50 mM, pH = 5), and 80 µL of KBr solution (5 M) were added to 80 µL of glucose supplemented saliva under stirring at 37 °C.

3.2.11 TEM analysis on AuMBNPs morphological changes

The glucose assay was performed as described in the previous section. The mixture was stirred at 37 °C for 10 min and, after colour change from blue to red, the reaction was stopped diluting and washing (centrifugation and resuspension process) the nanoparticles with cold (4 °C) HEPES buffer (10 mM, pH = 8.0). The control experiment was performed using non-supplemented saliva. The obtained nanoparticles were analysed by TEM.

3.2.12 Glucose dipstick, substrate preparation

0.4 mL of a freshly prepared AuMBNPs suspension (25 pM, A_{LSPR} = 0.4) in HEPES buffer (25 mM, pH = 7.0) were passed through a 0.4 µm porous nylon membrane using a syringe filter holder. The system was maintained in a vertically position promoting the uniform injection of the liquid and therefore uniform immobilization of the AuMBNPs on the membrane. Subsequently, 2 mL of air were injected to remove any residual water from the system. The prepared substrate was dried under vacuum for 10 minutes and then 15 µL of GOx solution (1 mg/mL, 145 U/mL) in acetate buffer (100 mM, pH = 5) were deposited by direct drop casting on the membrane.
The coated nylon support was dried again under vacuum and, finally, stored in low humidity conditions.

3.2.13 Glucose assay protocol

The glucose tests were performed adding on the prepared substrate 50 µL glucose supplemented saliva (90 – 180 µM, 1.5 – 3 mg/dL) and 50 µL of KBr solution (5 M) in acetate buffer (10 mM, pH = 5). The tests were carried out incubating the supports at 37 °C for 15 minutes. The test can be also carried out at room temperature leading to the same outcome but requiring a slightly longer time window.

3.2.14 Assay's reliability and validation

The glucose concentration of twenty saliva samples (eight from healthy subjects and twelve from diabetic subjects) was measured using a high sensitivity glucose assay kit (Merck - MAK181-1KT) chosen as a standard reference technique. Six saliva samples from healthy subjects presenting a physiological glucose concentration < 2 mg/dL were selected to numerically estimate the colorimetric

changes of our device at a targeted threshold (4 mg/dL ± 0.5). The glucose-dependent assay's color change was estimated after 15 min using Red, Green and Blue (RGB) coordinates acquired using ColorGrab (smartphone app). Glucose spikes were employed to normalize the saliva samples to 2.5, 4, and 6 mg/dL to evaluate the ΔRGB variability and the ΔRGB value range.

3.2.15 Assay reproducibility and Limit-Of-Detection

The experiments were performed using saliva samples from healthy donors, and the basal glucose concentration was measured using a high sensitivity glucose assay kit (Merck - MAK181-1KT) as a reference technique. The device reproducibility was tested using five independently produced assays, prepared with the same protocol. The reagents ratios were tuned to obtain an evident color change for salivary glucose concentrations ≥ 4 (± 0.5) mg/dL as the selected threshold. The reproducibility tests were performed using different glucose concentrations and identifying the color change numerically by extracting the RGB coordinates using Color Grab (smartphone free app).

3.3 Results

3.3.1 Sensing strategy

Here we present an original customizable nano-biosensor that allows the fast and sensitive visual detection of salivary glucose. This nanosensor pushes forward the state of the art of "non-aggregation" strategies, solving issues like the reaction time and conditions or the reliability in biological systems, which has limited so far POCT applications. The platform involves both etching and growing processes resulting in a reshaping effect that leads to a fast plasmon shifting and avoids any optical density (OD) loss (see **Figure 3.4**). The molecular mechanism underlying

the sensing strategy can be divided in two steps, one involving the oxidant species production and a second in which such species trigger a series of reactions, leading to AUMBNPs morphological changes. The enzyme produces hydrogen peroxide (H_2O_2) from the quantitative oxidation of the biomarker, H_2O_2 react with the halogen ions (X^-), present in stoichiometric excess, producing Br^-, Br^{2-}, Br^{3-} and $HBrO$ (the latter eventually converting to Br^2) that reduces the peroxide activation energy[15]. The second step consists of the etching of the nanoparticles. For this there are three possibilities[16–18]. In the first one, the halogen induces the H_2O_2 decomposition producing radicals ($^{\cdot}OH$) capable to oxidize gold. The second proposed strategy consists of X^- acting as ligand, stabilizing the dissolved Au atoms and promoting the erosion. In the third and most probable mechanism, H_2O_2 forms X_2 and X_3^- that oxidize gold atoms (**Figure 3.1**).

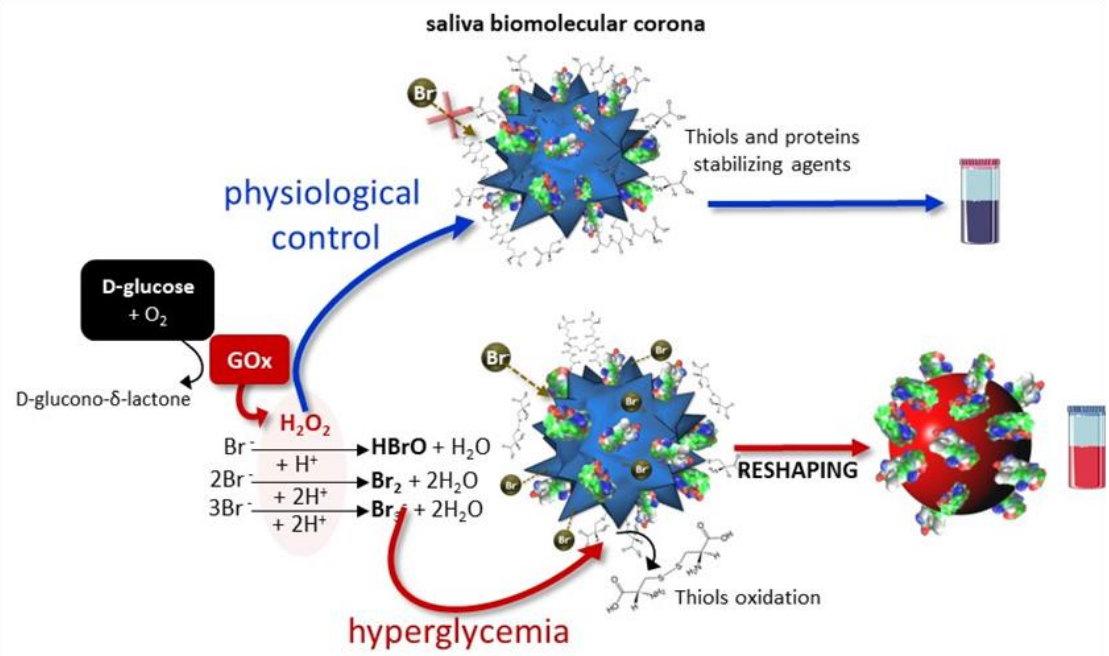

Figure 3.1 Scheme of detection mechanism to spot hyperglycemia from saliva sample.

3.3.2 AuMBNPs synthesis

15 nm citrate capped AuNPs have been obtained as previously described (see chapter2.) and used as seeds, 40 nm HEPES-capped AuMBNPs were synthetized as described in the paragraph 3.2, NPs size and shape have been characterized by UV-visible spectra, TEM and DLS analyses (see **Figure 3.2**).

Furthermore, the AuMBNPs has been optimized in order to obtain several shapes in terms of tips number and length. To tune the nanostructure branching, both HEPES and hydroxylamine concentrations have been modulated. Obtained particles have been characterized in terms of plasmonic shift by UV-visible spectroscopy (**Figure 3.3(C)**) with a peculiar peak of the AuMBNPs. In **Figure 3.3(B)** has been reported the DLS analysis, performed to characterize particles dimension and aggregation state, the peak position at Z-Ave= 66 nm confirm the dimension and the absence of secondary populations. In **Figure 3.3(A)** has been graphed the distribution of the particles diameters measured on acquired TEM images (see **Figure 3.3(D).**

Several AuMBNPs shapes have been synthetized and tested in terms of relative plasmon blue shifting (best sensitivity has been achieved for a $615 < \lambda_{max} < 650$nm). The **Figure 3.3(A)** reports the spectra of three synthesis in presence of increasing concentration of HEPES, tuning the binding agent concentration the plasmon peak can be modulated changing the dimension of the AuMBNPs tips. In the same way dosing the hydroxylamine, the particles shape can me modulated (see **Figure 3.3(B)**).

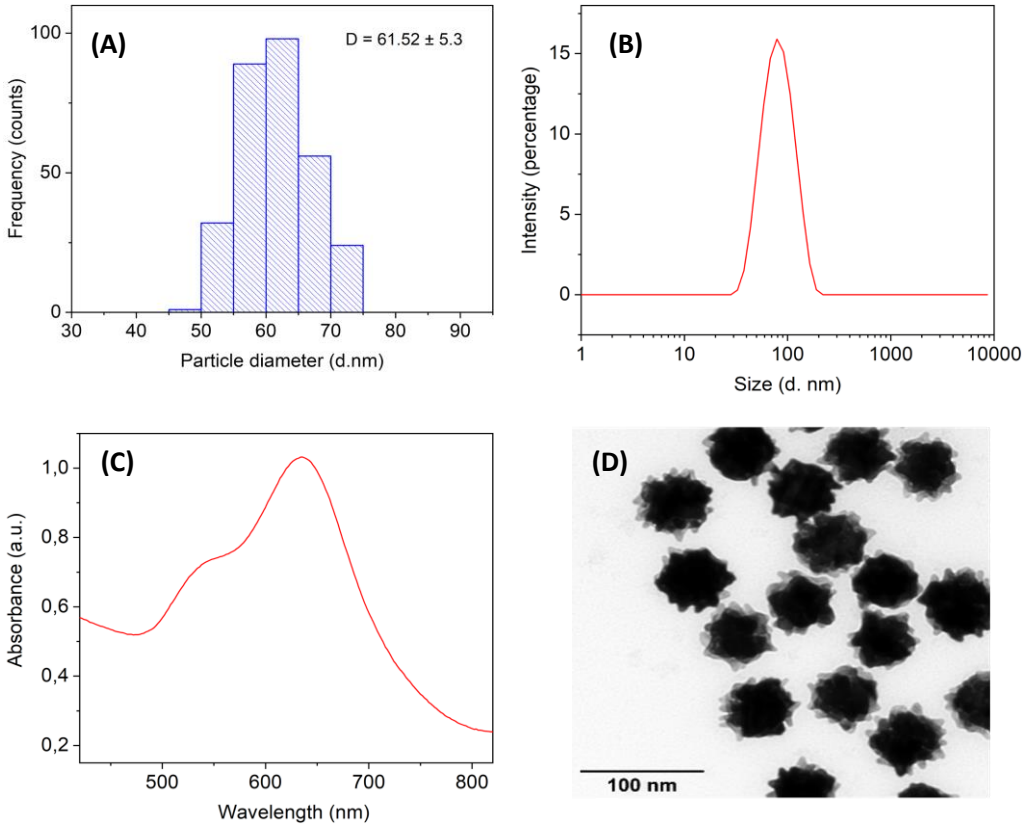

Figure 3.2 AuMBNPs characterization, **(A)** frequency distribution, **(B)** DLS analysis and diameters, **(C)** UV-Vis spectrum and **(D)** TEM image of AuMBNPs.

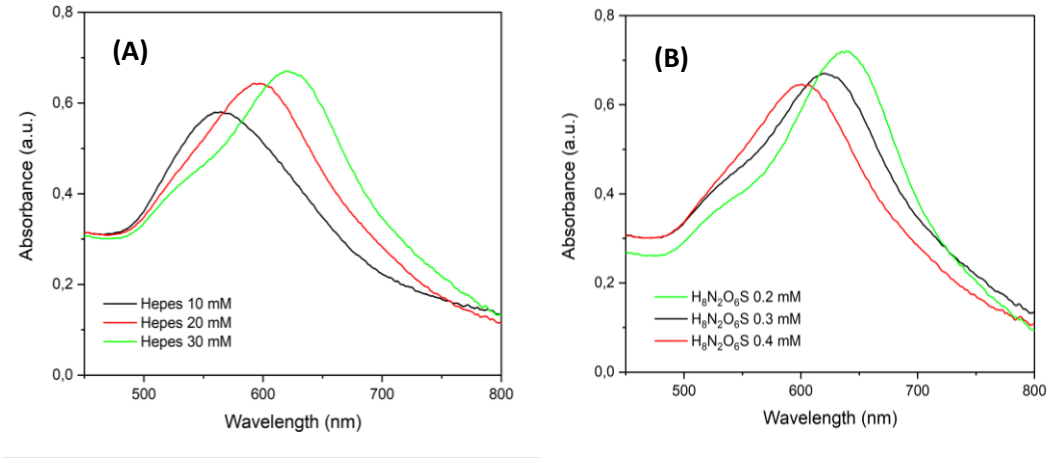

Figure 3.3 UV-Vis spectra of the 40 nm AuMBNPs grown in the presence of different concentrations of HEPES (**A**) and different concentrations of hydroxylamine (**B**). The LSPR redshift is finely tuneable.

3.3.3 Sensing strategy optimization

The nanoplasmonic sensor is based on the reshaping process of the AuMBNPs. Differently from a classical etching process in which the corrosion causes nanosensor shape and size modification with related optical density (OD) loss (see **Figure 3.4**), in this case we exploit reshaping process. The oxidized Au^{3+} is reduced again in an Ostwald ripening-like process. Combining etching and growing the reshaping process leads to a final spherical morphology.

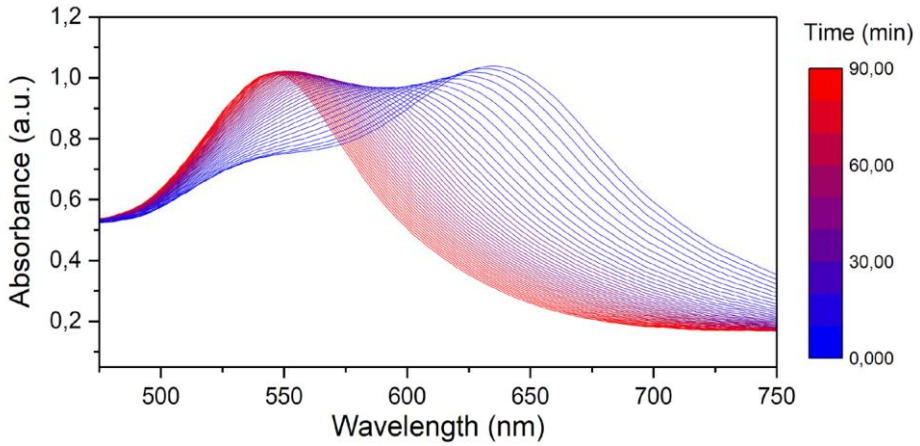

Figure 3.4 LSPR shifting resulting from the reshaping process in water; there is not any absorbance reduction since the particles dimension does not decrease over the process.

As a first step, the nanosensors capability has been characterized in terms of sensibility as color change in aqueous environment to determine best operational conditions. Since the etching is favored in acidic media, the pH has been optimized in the same experiment, while the activity of three different halogen ions has been evaluated (Cl^-, Br^-, I^-). After having optimized the reaction parameters, we have tested the platform sensitivity in a range of hydrogen peroxide concentrations in water as solvent. The optimal pH resulted to be pH=5, while the best selectivity was found using Br^- that promotes a clear LSPR blue shift in presence of hydrogen peroxide, while the control showed a relatively small color change (see **Figure 3.5**).

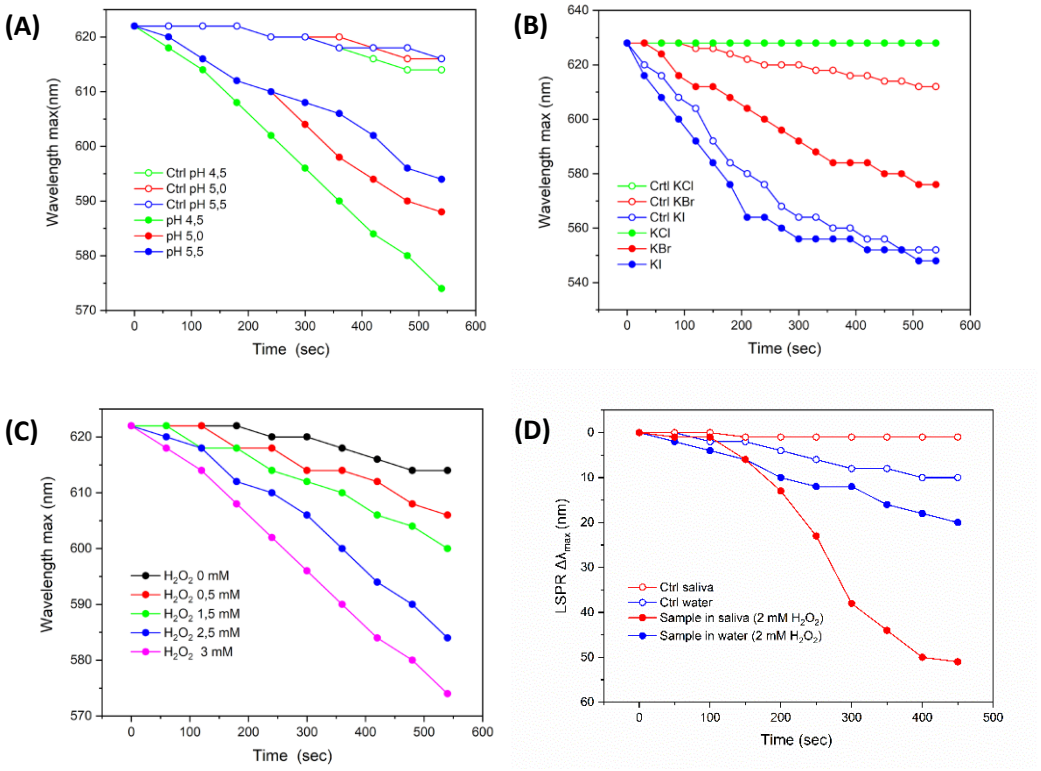

Figure 3.5 (A) LSPR λ_{max} evolution over time related to AuMBNPs reaction with H_2O_2 and KBr at pH = 4.5 (green), pH = 5 (red) and pH 5.5 (blue), **(B)** LSPR λ_{max} evolution over time related to AuMBNP reaction with H_2O_2 (3 mM) in presence of optimized concentrations of different halogens Cl- (green), Br-(red), I- (blue), **(C)** LSPR λ_{max} evolution for different concentrations of H_2O_2 in water (3-0 mM), **(D)** LSPR $\Delta\lambda_{max}$ evolution over time related to the reshaping in saliva and in water (the two model platforms performance at H_2O_2 final concentration of 2 mM).

AuMBNPs plasmon shifting has been characterized in a dedicated experiment to evaluate the role of hydrogen peroxide in a long-term interaction that can lead to non-specific etched products. AuMBNPs have been incubate with hydrogen peroxide (0-30mM) and the UV-visible spectra have been recorded for two hours. Reshaping process takes place only in presence of suitable conditions while, higher concentration of hydrogen peroxide can erode nanoparticles causing size reduction and optical density loss (see **Figure 3.6 A**). Evolution of absorbances over the time, shows that tuning relative concentrations of halogen, peroxide and AuMBNPs, reshaping process can be achieved (see **Figure 3.6 B**).

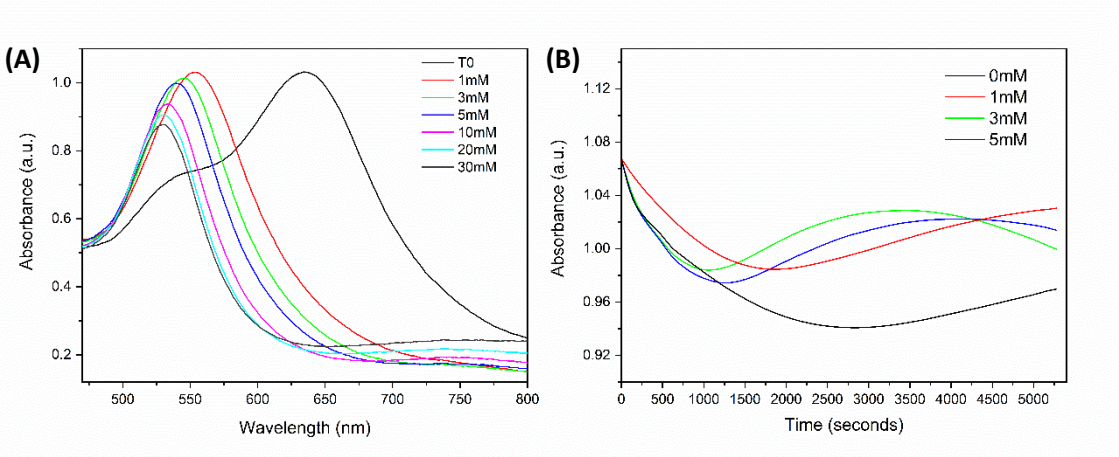

Figure 3.6 (A) Effect of hydrogen peroxide on AuMBNPs absorption intensity in water: absorption spectra related to AuMBNPs before (control) and after reaction with increasing concentrations of H_2O_2 (in presence of KBr). While H_2O_2 at 1-3 mM induced minimal absorption intensity variation, at higher concentrations (10-20-30 mM) significant loss of LSPR intensity was observed, suggesting that etching process occurred. **(B)** Evolution of optical density over the process suggests that etching/growing reactions interests AuMBNPs surface

3.3.4 Reshaping process characterization

To characterize and confirm the reshaping process, AuMBNPs dimensions have been measured. After having selected the shape indicators as tips number and length, together with the core diameter, several nanoparticles have been measured on acquired TEM images. The changes in morphology related to LSPR shifting are clearly visible in terms of number of tips and tips length. The morphological parameters measured to characterize the changes in shape are measured as reported in **Figure 3.7C**: d1 corresponding to the external diameter measured from tip to tip; d2, the core diameter, equal to the NP solid except the tips; d3 the tips length measured from the base to the end. While the (control) ctrl did not exhibit significant morphological changes, the saliva sample with pathological concentration of glucose led to nanostructures rearrangement from multibranched to spherical shape. (see **Figure 3.7**). The morphological analysis results are presented in **Figure 3.8**. The histograms show the comparison of dimensions with respect of the number of tips (N = 320), their length (N = 1700) and the core diameter (N = 1400). All samples are normally distributed, and Mann-

Whitney test confirmed statistical significance (p-value < 0.001) of mean sizes distribution difference.

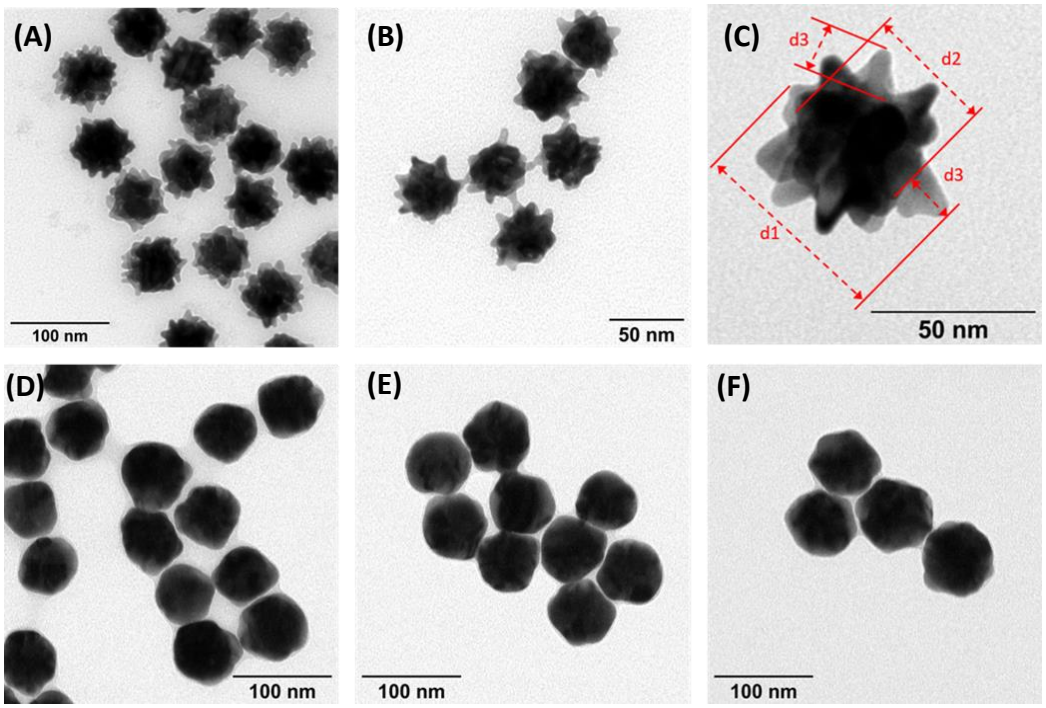

Figure 3.7 TEM images of AuMBNPs after glucose assay in saliva **(A)**-**(C)** representative images of the AuMBNPs after testing non-supplemented saliva sample; **(D)**-**(F)** representative images of AuMBNPs after testing glucose-supplemented saliva.

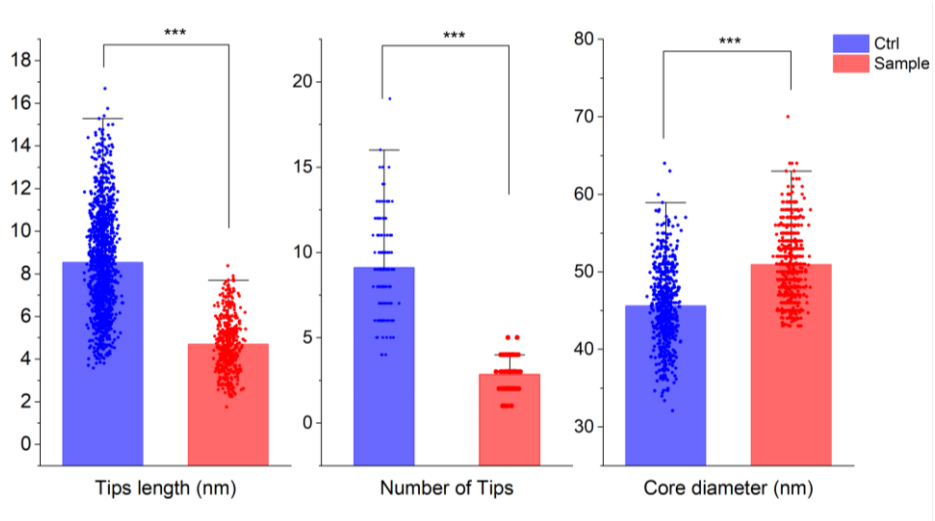

Figure 3.8 Statistical TEM analysis measuring tips (numbers and lengths) and "core" dimensional variation between control and sample nanostructures. Statistical significance was determined by Mann-Whitney test (***p < 0.001).

3.3.5 Saliva testing (in solution)

Adapting this platform to real working conditions in saliva, employing glucose spikes, GOx enzyme, and a large excess of Br^- (see scheme in **Figure 3.1**) resulted in a strikingly better performance than that in water. The system was so stable that we could employ much larger Br^- concentration, without affecting the control. Proteins and metabolites present in saliva can rapidly coat the AuMBNPs forming the so-called biomolecular corona, which can act as an organic shield protecting and stabilizing the surface atoms. Stability of the AuMBNPs has been tested versus raw saliva with and without GOx enzyme. While most of colorimetric detection methods using nanoparticles can't be exploited in real samples because of the complexity of matrixes like saliva, this nanosensor shows good stability maintaining particles surface properties (see **Figure 3.9**).

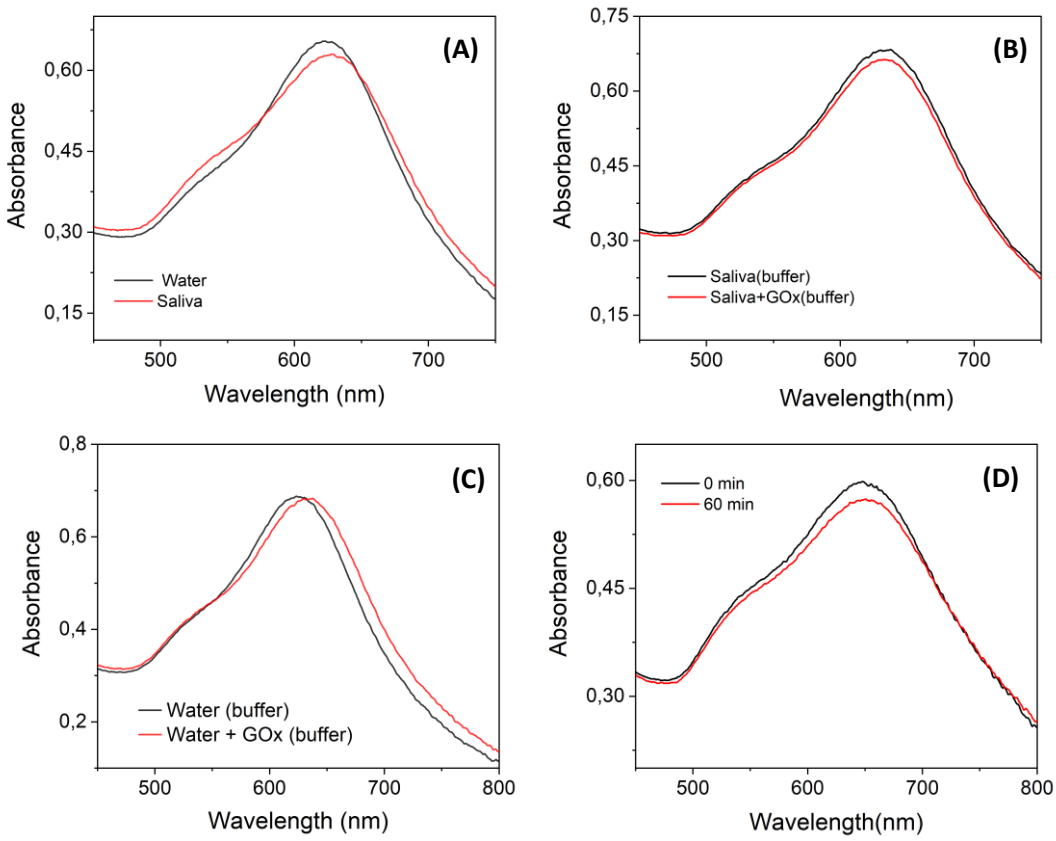

Figure 3.9 (A) Characteristic LSPR red-shift related to the protein adsorption on plasmonic nanoparticles. **(B)** and **(C)** show no GOx effect on the LSPR. **(D)** Stability test of AuMBNPs in saliva: the absorption spectra show good colloidal stability over 60 min also in presence of the enzyme. The saliva employed was previously diluted 1:4 in acetate buffer as for assay condition.

Salivary proteins (i.e., mucin) promote higher colloidal stability limiting the surface availability by steric hindrance, while salivary thiols (i.e., cysteine, glutathione and others) can act as surface ligands. These factors together firmly preserve the AuMBNPs shape even in presence of a large excess of Br^- that otherwise would lead to uncontrolled fast etching and immediate colour change even in absence of glucose. Indeed, the saliva medium allowed for a significant extension of the dynamic range of the assay along with a faster response, meaning that resolution and sensitivity were also strongly improved (see **Figure 3.4 D**). Analysing the

physiological control (no added glucose), no significant spectral changes were observed, indicating a better resolution of the nanosensor in saliva compared to non-biological media (see **Figures 3.4 D**). This is a key point since it excludes the possibility of false positives, due to spontaneous color changes of the AuMBNPs in the test timeframe (10–20 min); furthermore, it guarantees a faster naked-eye recognizable color distinction, due exclusively to the glucose present in saliva. The presence of non-physiological glucose concentrations in saliva (≥2 mM), reproducing hyperglicemia conditions, indeed promote a spectral fast change with a large blue shift of the LSPR wavelength max, and no significant OD loss (**Figure 3.10 A**).

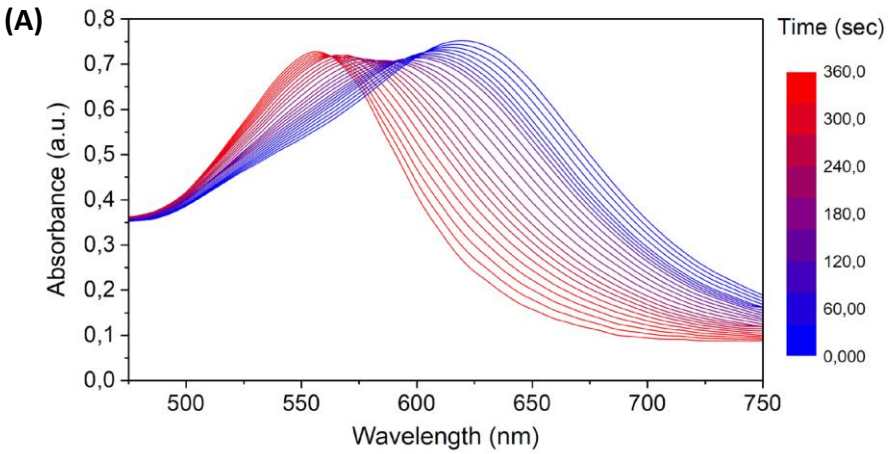

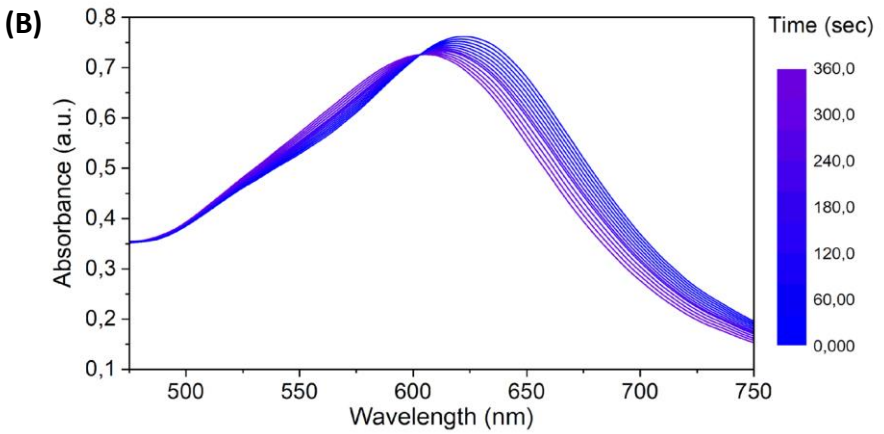

Figure 3.10 Reshaping process in saliva: AuMBNPs absorption spectra evolution over time during the assay using **(A)** glucose supplemented saliva (hyperglycemic condition) **(B)** physiological saliva (ctrl). For more details, see the experimental procedure section.

3.3.6 Micro-Pad (μ-Pad) device fabrication

In order to realize a portable home-testing device prototype, the sensing platform was transferred onto a solid substrate. Several casting methods have been tested to obtain a well monodispersed layer of AuMBNPs. Classical incubation-like and drop casting techniques resulted to be inadequate, leading to surface defects, for which reason, a filtering-based deposition method was chosen. To evaluate the particles retention capability, residual AuMBNPs (in washing water) have been dosed by UV-visible spectra of aqueous solution after deposition (see **Figure 3.11 B**). Using a syringe filter holder, 600mL of AuMBNPs colloidal solution at O.D.= 0.9 was homogenously deposited on 0.22 mm mesh size nylon membrane and then covered with a layer of glucose oxidase enzyme to produce the micro-Pad (μ-Pad) (see **Figure 3.11 A**).

Among the different materials tested (including cellulose acetate, nitrocellulose, PVDF), a porous nylon membrane was selected, presenting well structured (ordered) surface and a good balance between wettability and hydrophobicity.

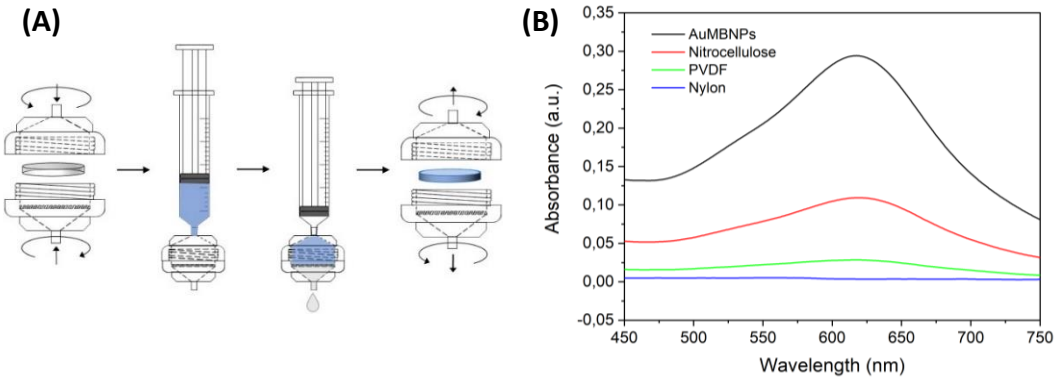

Figure 3.11 (A) Schematics of the AuMBNPs deposition on the membrane substrate. **(B)** UV-vis absorption spectra of a AuMBNPs (20 pM) aqueous solution before (black curve) and after filtration through different membranes (nitrocellulose, PVDF and nylon). All the AuMBNPs were retained in the nylon membrane, leading to colourless filtrate (no light absorption, blue curve).

3.3.7 μ-Pad device characterization

From the reflectance spectra, glucose supplemented saliva appeared to be ca. 50 nm blue-shifted compared to the control (consistent with the data observed in suspension), with the curve minima corresponding to the particles LSPR. This is also a confirmation of the reshaping process occurring on the substrate, with spherical GNPs on the test membrane after exposure to hyperglycemic saliva (see **Figure 3.12**). The use of a solid substrate led to a significant improvement of the reagents stability. While colloidal dispersions of AuMBNPs in water lose their morphological and plasmonic properties overtime, the on-substrate assay showed excellent stability up to 6 months, meaning that also the enzyme functionality was maintained. An additional advantage is that, even after glucose testing, the "test strip" could be stored, keeping the outcome unaltered for ≥6 months.

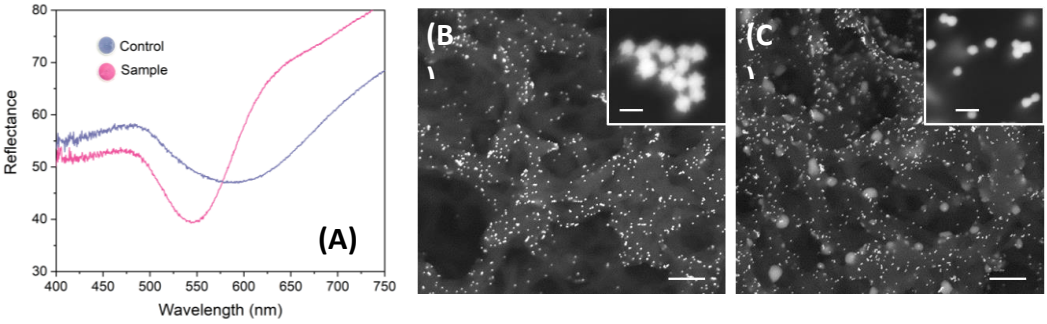

Figure 3.12 (A) Reflectance spectra of the membrane substrates, related to control and sample (picture in inset), showing a clear blue-shift (from λ = 600–550 nm). **(B)** SEM image of control (scale bar 2μm, inset scale bar 100nm), **(C)** SEM image of sample (scale bar 2μm, inset scale bar 100nm).

The μ-Pads surface was characterized by using reflectance spectroscopy and scanning electron microscopy (SEM). From SEM imaging, we could observe the nanostructure morphology directly on the membrane. Comparing images of nylon and cellulose as solid substrate for μ-Pad fabrication is clearly visible how a more organized microstructure allows a monodisperse organization of deposed AuMBNPs. Nylon membrane can efficiently host and stabilize gold nanoparticles in a well monodisperse layer (see **Figure 3.13 A, C, E**) without compromising the reactivity. On the contrary, cellulose paper requires for higher concentration of AuMBNPs to obtain suitable colour intensity for naked eye applications since most of nanoparticles are trapped and covered on disordered fiber matrix (see **Figure 3.13 B, D, F**).

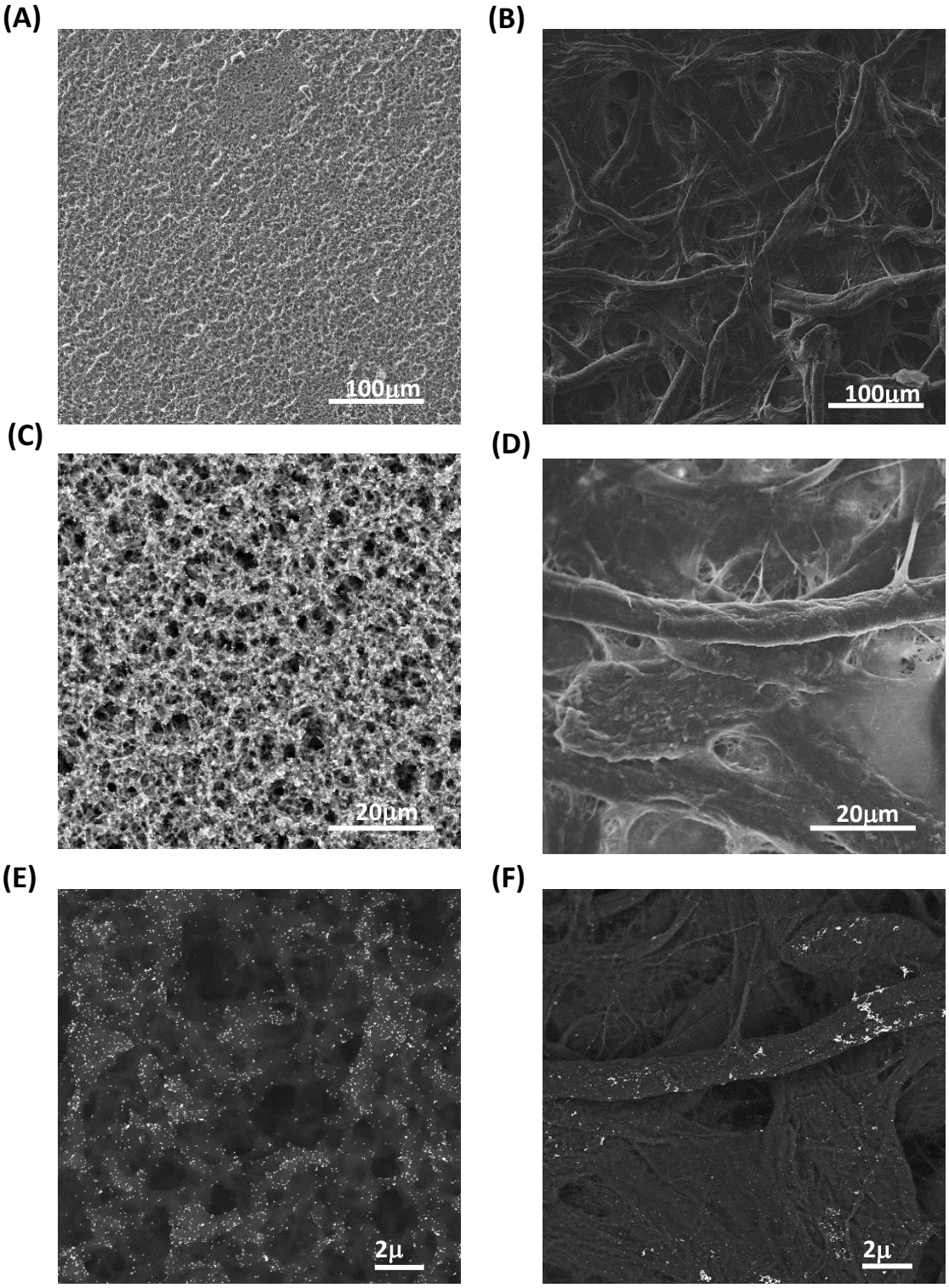

Figure 3.13 (A), **(C)** SEM images of Nylon membrane, **(B)**, **(D)** SEM image of Cellulose membrane. **(E)** SEM image of Nylon membrane in back scattering mode with monodisperse AuMBNPs, **(F)** SEM image of Cellulose membrane in back scattering mode with raft AuMBNPs.

3.3.8 Real saliva samples testing

From an active collaboration with a group of Prof.ssa Mariangela Rondanelli, MD, PhD "Ospedale Policlinico San Matteo" of Pavia, we obtained a sets of saliva samples of diabetic subjects collected in normal and hyperglycemic conditions. Using a high-sensitivity glucose assay kit (Merck - MAK181-1KT) chosen as a standard reference technique, we initially defined the correlation between blood and salivary glucose. Since the literature is contradictory about glucose salivary levels and its correlation with blood levels, we tested two different collecting protocols in healthy and diabetic donors to characterize both the effect of salivary flow stimulation, and the lag time between blood and salivary glucose peaks over the day (also using traditional blood electrochemical glucometer). Considering the poor correlation and the high intra-subject variability that we observed, we had to improve the collecting protocol, preferring the fluid normally secreted (unstimulated) by all set of oral glands. In a comparative experiment, stimulated saliva samples show a lower correlation and higher variability (see **Figure 3.14**) compared with unstimulated samples collected at the same time (pairing blood glycemic conditions),

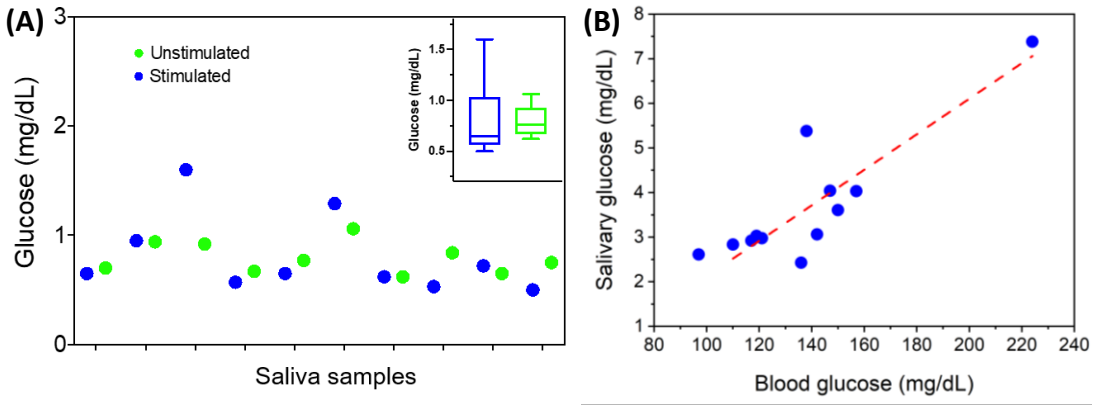

Figure 3.14 (A) Salivary glucose level of stimulated samples (blue dots) and unstimulated ones (green dots).In the inset are illustrated mean values and standard deviation of each populations. **(B)** correlation of saliva and blood glucose values of different diabetic patients.

Saliva samples were tested with the proposed micropad-like colorimetric assay prototype. A small amount (20 µL) of glucose supplemented saliva (with several glucose concentrations) was sufficient to trigger a rapid colour change from blue to red within 5–15 min, depending on the glucose concentration. Saliva samples from 4 different donors have been spiked using glucose standard solution adding 1 mg/dL (Spl1), 2 mg/dL (Spl2) and 5 mg/dL (Spl3) using as control samples without GOx (Ctrl 1), with denaturized GOx (Ctrl 2) and without spikes (Ctrl 3). As reported in **Figure 3.15**, the µ-Pad allows the quantitative colorimetric glucose detection. By finely tuning the reshaping conditions is possible to achieve a threshold for ON-OFF colour change suitable in fast screening applications.

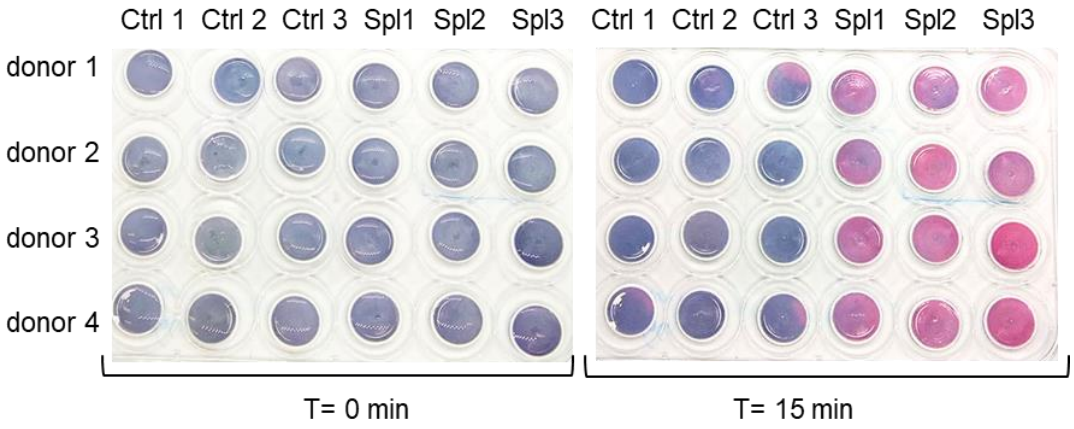

Figure 3.15 Preliminary validation of the glucose assay prototype on different saliva samples: picture of the glucose assay immediately after saliva sample addition on the membrane (left) and after 15 min (right). The saliva samples collected from different donors were tested with no additional glucose (Ctrl3) and supplemented with glucose (Spl1 = 1.5 mg/dL, Spl2 = 3 mg/dL, Spl3 = 5 mg/dL) to reproduce hyperglycemic conditions. Additional controls in which the assay was performed on non-supplemented saliva but in absence of GOx (Ctrl1) or in presence of inactivated GOx (Ctrl2) were also included in the study.

3.3.9 Colour change characterization

The assay prototype was finally optimized for analysis on real samples, considering that physiological glucose concentration in saliva is commonly <2 mg/dL (<130

mg/dL in human serum) while it is ≥4 mg/dL for hyperglycemic condition (≥160–200 mg/dL in human serum). It is important to stress that the correlation between hematic and salivary glucose is not based on a constant ratio over the whole range of concentrations. For this reason, aiming at an ON/OFF response as an alarm bell for healthcare, we set our threshold about ≥4 ± 0.5 mg/dL. For salivary glucose concentrations above this range values, the assay must produce an evident color change. To numerically estimate the colorimetric changes of our device and perform statistical data analysis, RGB and Ciano, Magenta, Yellow and Black (CMYK) coordinates of the substrate were acquired using a smartphone app. (see **Figure 3.16**)

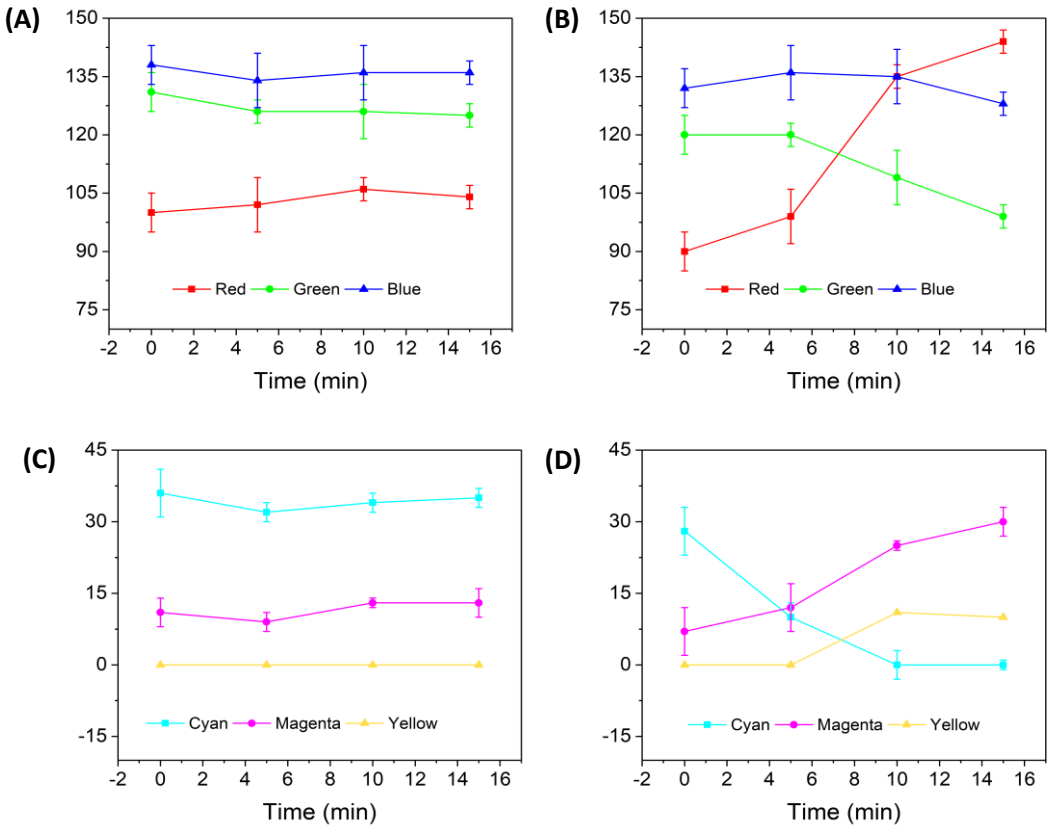

Figure 3.16 (A) (C) RGB and CMY coordinates evolutions in a "negative" sample for a glucose concentration < 4 ± 0.5 mg/dL, **(B)** and **(D)** RGB and CMY coordinates evolutions in a "positive" sample for a glucose concentration > 4 ± 0.5 mg/dL

3.3.10 Limit-Of-Detection

The ΔRGB (see formula below) obtained at different glucose concentrations was employed for statistical data analysis:

$$\Delta RGB = \sqrt{(R_{t1} - R_{t0})^2 + (G_{t1} - G_{t0})^2 + (B_{t1} - B_{t0})^2}$$

Glucose spikes were employed to normalize the saliva samples to 2.5, 4, and 6 mg/dL to evaluate the ΔRGB variability and the ΔRGB value range, allowing to identify our threshold. An evident colour change, expected for salivary glucose concentrations ≥ 4 (± 0.5) mg/dL after 15 min of test, was estimated to correspond approximately to ΔRGB ≥ 30 (± 10) while little or no color change is expected for physiological concentrations (ΔRGB < 15 ± 5). Altogether, the twenty saliva samples were analysed for their basal content using our ON/OFF colorimetric assay and the commercial kit to perform a small clinical trial (see **Figure 3.17**). The acquired ΔRGB obtained at different glucose concentrations in after 15 minutes of test were also employed to calculate the LOD.

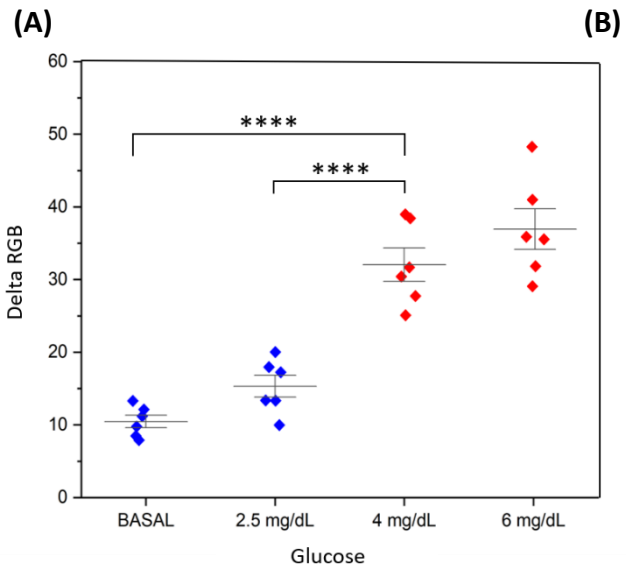

Donors (n)	Glucose (mg/dL)	Assay's colour (ON/OFF)
1	2.6	●
2	5.0	●
3	5.4	●
4	7.4	●
5	3.1	●
6	2.7	●
7	4.4	●
8	4.3	●
9	2.4	●
10	4.0	●
11	1.6	●
12	3.0	●
13	1.5	●
14	1.5	●
15	1.5	●
16	1.8	●
17	1.5	●
18	2.2	●
19	1.8	●
20	1.7	●

Figure 3.17 (A) Analytical plot for LOD calculation, statistical significance was determined using a one-way ANOVA and Tukey's multiple comparison test (****P < 0.0001). **(B)** ΔRGB data relative to the color change of the assay obtained from clinical samples

The LOD was calculated based on the ratio between three times the standard deviation for the control and the angular coefficient obtained from the analytical curve (**Figure 3.18(B)**) (see formula below).

$$X_{LOD} = 3{,}3 * SD_{blank}/b$$

X_{LOD}: limit of detection; SD_{blank}: standard deviation of the naturally occurring pseudo-blank; b: slope of the calibration. The assay performances were very good and reproducible using different independently produced devices to analyse the same saliva sample from a donor, reaching a LOD of 0.4 mg/dL, in line with the best performing glucose colorimetric sensors reported[20,21]. However, some variability on the LOD values was expected when analysing saliva samples from multiple different donors (presenting some difference in the composition), resulting in a more representative average value of 1.4 mg/dL. Such LOD value is still appropriate for our ON/OFF detection, allowing to cope with the intrinsic biological variability or real clinical samples.

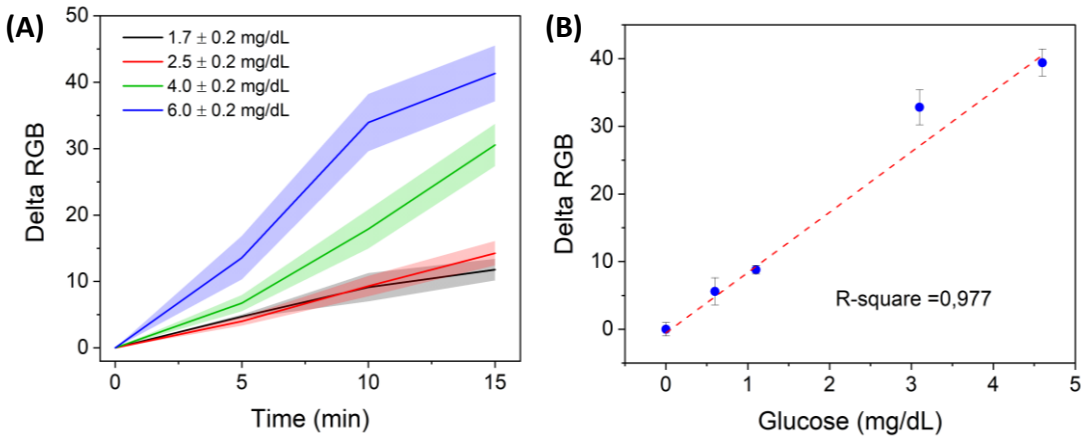

Figure 3.18 Assay performance analysis: (**A**) Delta RGB for different spiked sample, in a ON-OFF setup samples containing glucose < 4 mg/dL report negligible colour change while 4 and 6 mg/dL show remarkable proportional delta RGB (**B**) Analytical plot for LOD calculation.

3.4 Conclusions

In conclusion, the nanoscale architecture of AuMBNPs and their sensitive plasmonic features were exploited for the development of a novel colorimetric assay for hyperglycemia, demonstrated to be effective in real saliva samples. Interestingly, the sensing platform, when operating in salivary medium, showed improved solidity and better dynamic range than in water, suggesting a proactive role of the biomolecular corona both in stabilizing the nanosensor and in promoting the reshaping process (instead of etching). The technological transfer from solution to the solid substrate finally led to the realization of a dipstick-like prototype for non-invasive self-monitoring of glycemia. The assay was finally validated as a rapid test (15 min) on various clinical samples showing good reliability and, with further technological development, great potential for future home-testing applications. Overall, it is important to stress that the designed sensing platform could be easily adapted for the monitoring of several other pathologies, directly involving different oxidase enzymes.

Considering the high selectivity and sensitivity as well as the remarkable colorimetric readout, the nanosensor has been already patented as "Procedimento e kit per rilevare un analita in un campione".P. Pompa and P. Donati 102020000007162 (2020). Moreover, in light of the results from real salivary samples glucose assessment, and the notable potentiality in a POCT device application this work has been published in a peer reviewed journal[22].

3.5 Bibliography

1. Zhang, M., Liu, Y. Q. & Ye, B. C. Colorimetric assay for parallel detection of Cd2+, Ni 2+ and Co2+ using peptide-modified gold nanoparticles. *Analyst* **137**, 601–607 (2012).
2. Zhou, W., Gao, X., Liu, D. & Chen, X. Gold Nanoparticles for in Vitro Diagnostics. *Chemical Reviews* **115**, 10575–10636 (2015).
3. Saha, K., Agasti, S. S., Kim, C., Li, X. & Rotello, V. M. Gold nanoparticles in chemical and biological sensing. *Chemical Reviews* **112**, 2739–2779 (2012).
4. Howes, P. D., Chandrawati, R. & Stevens, M. M. Colloidal nanoparticles as advanced biological sensors. *Science (80-.).* **346**, 1247390 (2014).
5. Valentini, P. & Pompa, P. P. Gold nanoparticles for naked-eye DNA detection: Smart designs for sensitive assays. *RSC Advances* **3**, 19181–19190 (2013).
6. Peixoto de Almeida, M. *et al.* Gold Nanoparticles as (Bio)Chemical Sensors. in *Comprehensive Analytical Chemistry* **66**, 529–567 (Elsevier B.V., 2014).
7. Zhang, Z. *et al.* Plasmonic colorimetric sensors based on etching and growth of noble metal nanoparticles: Strategies and applications. *Biosensors and Bioelectronics* **114**, 52–65 (2018).
8. Monopoli, M. P., Åberg, C., Salvati, A. & Dawson, K. A. Biomolecular coronas provide the biological identity of nanosized materials. *Nat. Nanotechnol.* **7**, 779–786 (2012).
9. Pino, P. Del *et al.* Protein corona formation around nanoparticles - From the past to the future. *Materials Horizons* **1**, 301–313 (2014).
10. Rao, H., Xue, X., Wang, H. & Xue, Z. Gold nanorod etching-based multicolorimetric sensors: Strategies and applications. *Journal of Materials Chemistry C* **7**, 4610–4621 (2019).
11. Xu, S. *et al.* A morphology-based ultrasensitive multicolor colorimetric assay for detection of blood glucose by enzymatic etching of plasmonic gold nanobipyramids. *Anal. Chim. Acta* **1071**, 53–58 (2019).
12. Zhang, Z., Chen, Z., Cheng, F., Zhang, Y. & Chen, L. Highly sensitive on-site detection of glucose in human urine with naked eye based on enzymatic-like reaction mediated etching of gold nanorods. *Biosens. Bioelectron.* **89**, 932–936 (2017).
13. Liu, X. *et al.* A plasmonic blood glucose monitor based on enzymatic etching of gold nanorods. *Chem. Commun.* **49**, 1856–1858 (2013).
14. Zhang, Z., Chen, Z. & Chen, L. Ultrasensitive Visual Sensing of Molybdate Based on Enzymatic-like Etching of Gold Nanorods. *Langmuir* **31**, 9253–9259 (2015).
15. Weng, G., Dong, X., Li, J. & Zhao, J. Halide ions can trigger the oxidative etching of gold nanorods with the iodide ions being the most efficient. *J. Mater. Sci.* **51**, 7678–7690 (2016).

16. Long, R., Zhou, S., Wiley, B. J. & Xiong, Y. Oxidative etching for controlled synthesis of metal nanocrystals: Atomic addition and subtraction. *Chem. Soc. Rev.* **43**, 6288–6310 (2014).
17. Yuan, H. *et al.* Reshaping anisotropic gold nanoparticles through oxidative etching: The role of the surfactant and nanoparticle surface curvature. *RSC Adv.* **5**, 6829–6833 (2015).
18. Sun, S. *et al.* Visually monitoring the etching process of gold nanoparticles by KI/I2 at single-nanoparticle level using scattered-light dark-field microscopic imaging. *Nano Res.* **9**, 1125–1134 (2016).
19. Maiorano, G. *et al.* Monodispersed and size-controlled multibranched gold nanoparticles with nanoscale tuning of surface morphology. *Nanoscale* **3**, 2227–2232 (2011).
20. de Castro, L. F. *et al.* Salivary diagnostics on paper microfluidic devices and their use as wearable sensors for glucose monitoring. *Anal. Bioanal. Chem.* **411**, 4919–4928 (2019).
21. Gabriel, E. F. M. *et al.* Highly sensitive colorimetric detection of glucose and uric acid in biological fluids using chitosan-modified paper microfluidic devices. *Analyst* **141**, 4749–4756 (2016).
22. Donati, P., Pomili, T., Boselli, L. & Pompa, P. P. Colorimetric nanoplasmonics to spot hyperglycemia from saliva. *Front. Bioeng. Biotechnol.* **8**, 1404 (2020).

4 Appendix: Platinum nanoparticles-based colorimetric sensor for mercury detection

4.1 Platinum nanoparticles

In recent years, platinum nanoparticles (PtNPs) have attracted impressive attention in many fields, such as chemical industry and renewable energies, for their selectivity and efficiency in catalysis[1,2]. PtNPs are effective heterogeneous catalysts, widely used in the hydrogenation, isomerization, and dehydrogenation reactions. Moreover, they are applied in the preparation of several high-value chemicals of food industry, such as vitamins and fats, as well as fine biofuel for the energy sector[34–7].

Another field of research involving the use of this nanomaterial concerns nanomedicine[8]. Thanks to their good cytocompatibility[9,10] and the stability in biological environment[11,12], PtNPs have been proposed, in combinations with other materials, as drug carriers in anticancer, radiothermal, and photothermal therapies[9,10,13,14]. Moreover, they represent good candidates for the second generation of high sensitivity nanobiosensors, due to their ability to act as artificial enzymes (nanozymes). Indeed, exploiting PtNPs in the signal amplification step, the colorimetric/fluorimetric response can be significantly enhanced[15].

4.1.1 Nanozymes

The term “nanozyme” has been used for the first time by Manea *et al*. to define functionalized gold NPs with prominent ribonuclease-like activity[16]. Today, this definition is adopted for all the NPs exhibiting enzymatic-like activity[17,18]. Such artificial and often inorganic enzymes result to be highly stable, robust, and cost-effective compared to the corresponding biological native form[19]. Moreover, they

offer a large surface-to-volume ratio and easy customizable surface for a variety of ligand conjugations.

An important class of enzymes highly investigated in nanomedicine for biosensing and medical applications include[20,21]:

- Peroxidase (HRP), an antioxidant enzyme that catalyses the oxidation of a substrate through the decomposition of peroxides, such as hydrogen peroxide (H_2O_2).

$$2AH + H_2O_2 \xrightarrow{Peroxidase} 2A + H_2O$$

- Oxidase, that promotes the oxidation of an antioxidant substrate with molecular oxygen (O_2), following two possible and different routes of reaction.

$$AH + O_2 \xrightarrow{Oxidase} A + H_2O \qquad 2\,AH + O_2 + H_2O \xrightarrow{Oxidase} 2A + 2H_2O_2$$

- Superoxide dismutase (SOD) and catalase (CAT), that display an antioxidant activity, neutralizing excess of reactive oxygen species (ROS), such as superoxide ($O_2^{\cdot}$), hydroxyl radical ($HO^{\cdot}$), and (H_2O_2).

$$O_2^{\cdot} + O_2^{\cdot} + 2H^+ \xrightarrow{SOD} O_2 + H_2O_2 \qquad 2H_2O_2 \xrightarrow{CAT} O_2 + H_2O$$

Among other metal nanoparticles, PtNPs have gained huge attention in nanomedicine as enzymes substitutes, due to their efficiency as CAT, HRP, and SOD[22–26]. PtNPs are gradually substituting HRP and CAT in several colorimetric or fluorometric assays. Up to now, PtNPs-based colorimetric sensors have been developed for the detection of tumour markers[27], metal ions, drugs[28], viruses[15], antibodies[29], and small molecules[3031].

PtNPs enzymatic activity is affected by NPs size, shape, and coating. Most notably, it has been demonstrated that nanozyme activity scales inversely with the particle size. Smaller nanoparticles expose larger surface, showing higher catalytic activity compared to the larger ones (with the same total mass)[20]. It has been reported that PtNPs of 5 nm have higher peroxidase performance (apparent Km with H_2O_2 = 47.2 mM) compared to 20 nm PtNPs[26] (apparent Km with H_2O_2= 123.6 mM) (see

Figure 4.1). Moreover, recently published studies reported that the NP shape affects the catalytic activity[32–34], drawing the scientific attention to the development of more controllable synthetic protocols[32].

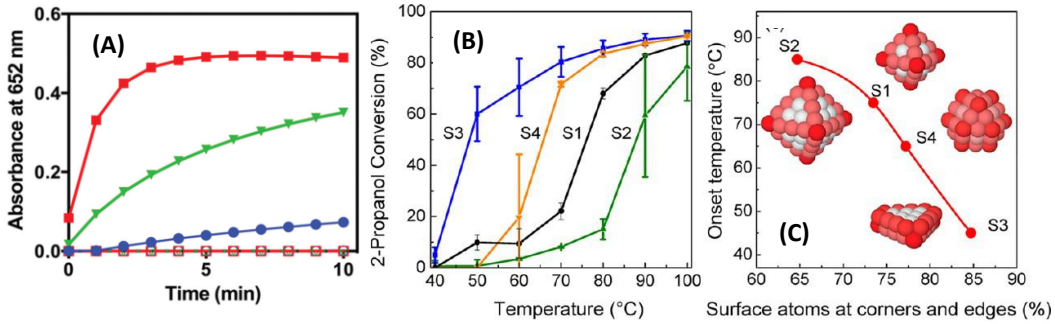

Figure 4.1 HRP-like activity of PtNPs. **(A)** Time-dependent UV-visible absorption spectra at 652 nm of 5 nm PtNPs (red), 20 nm PtNPs (green), and HRP enzyme (blue) (ref.26) **(B)** Partial oxidation of 2-propanol over PtNPs of similar size (S1-S4) but different shape. **(C)** Average number of broken bonds at the NP surface (ref 32).

4.1.2 PtNPs as peroxidase-mimics

In biological environment, peroxidase catalyzes the reduction of hydrogen peroxide, oxidizing the antioxidant molecule glutathione.

In diagnostics, this enzyme is used in combination with chromogenic or fluorometric substrates (e.g., 3,3',5,5'-tetramethylbenzidine-TMB, 2,2'-azino-bis(3-ethylbenzothiazoline-6-sulphonic acid)-ABTS or luminol) and hydrogen peroxide in several assays. However, its use in POC diagnostics is restricted by intrinsic limitations, namely intolerance to harsh conditions and ease of denaturation together with the large-scale production problems and the high costs[21]. Therefore, PtNPs have been proposed to effectively replace peroxidase in these applications. Indeed, it has been demonstrated that PtNPs are able to catalyse the hydrogen peroxide dissociation in 2 radicals ($HO^{\cdot}$) that trigger a chain mechanism resulting in a two-step electron transfer for the TMB oxidation[35–37] (see **Figure 4.2 A**).

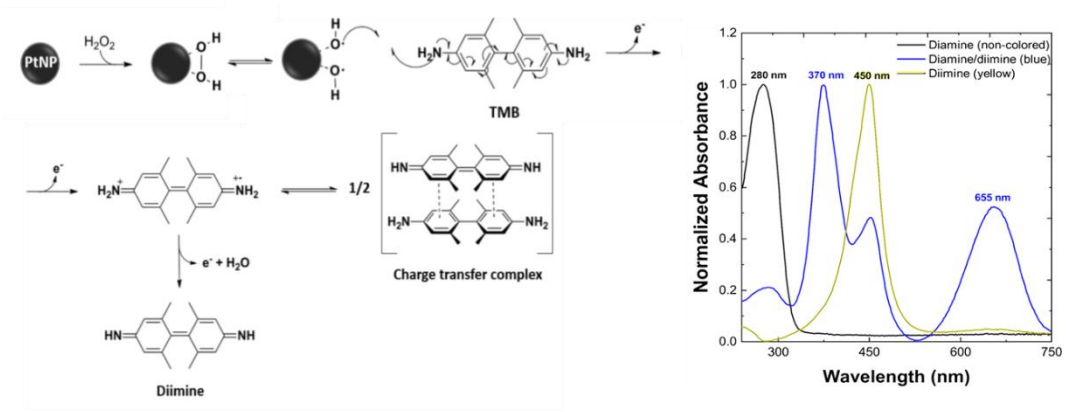

Figure 4.2 (A) PtNPs-catalyzed TMB oxidation mechanism in the presence of H_2O_2. **(B)** UV-vis spectra of TMB species: consumed diamine (280 nm, black line), charge transfer complex (370 nm and 652 nm, blue line), and diimine (450 nm, yellow line) (ref.38).

The first step leads to the 3, 3',5 ,5'-Tetramethylbenzidine TMB radical that disproportionates in a blue-coloured complex, whilst the second electron transfer step is induced by the addition of sulfuric acid, resulting in a yellow diimine molecule. The reaction can be monitored by UV-vis spectrophotometric analysis: over the reaction progress, the TMB molecule UV peak (λ = 280 nm) decreases, and two new peaks appear in the visible range (λ1 = 370 nm, and λ2 = 652 nm) relatively to the charge transfer complex. These two peaks grow to a maximum during the reaction and then decay, being replaced by a peak at λ = 450 nm, indicating the formation of the diiminic product[38,39] (see **Figure 4.2 B**). The PtNPs peroxidase-like behaviour has been extensively investigated by a kinetic study, confirming that PtNPs exhibit Michaelis-Menten kinetics, showing higher affinity to TMB compared to the natural enzyme[26].

4.1.3 PtNPs synthesis

Chemical Reduction (WCR) represents the most commonly used PtNP synthetic method[4041]. It involves the use of a reducing agent, such as sodium borohydride ($NaBH_4$), sodium citrate and ascorbic acid, to produce metallic platinum, starting from the Pt salt, namely hexachloroplatinic acid (H_2PtCl_6). The reduction rate, the reducing agent/ Pt salt ratio, the temperature of the reaction, and the stabilizing

molecules can be easily modified for the tuning of the PtNP shape and size. PtNPs with a diameter of 20-100 nm can be obtained by a multistep seed-mediated growth process[42]. In the first step, the nucleation phase takes place, and clusters of Pt (0) atoms are obtained. In a later step, the NPs growth from seeds occurs, leading to bigger structures.

To meet the increasing demand for high biocompatible and surfactants-free PtNPs, researchers have moved their attention on "green" synthesis protocols. These methods are mainly based on the use of "green" reagents, such as ascorbic acid and trisodium citrate, and "green" solvents, such as water instead of ethylene glycol.[43] In our laboratory, the green PtNPs synthesis was optimized to produce well monodispersed, flower-shaped platinum nanoparticles[26]. The jagged surface of PtNPs offers a drastically increased surface, if compared to spherical shaped NPs.

4.1.4 PtNPs-based methods for mercury ions detection

Aa previously discussed in *Chapter 2*, most of heavy metal ions are known to be carcinogens and highly toxic. Notably, mercury species effects on living organisms have been well characterized[44–46]. However, considering that traditional tests are expensive and require costly instrumentations (e.g. graphite furnace atomic absorption spectroscopy-GF-AAS, inductively coupled plasma-mass spectrometry-ICP-MS, and liquid chromatograph-mass spectrometry-LC-MS)[47–49], the mercury assessment in drinking water and food is sporadic. Therefore, the development of an effective mercury detection method for point-of-care applications is still a challenge.

The purpose of this project was the development of a novel naked eye, rapid, and easy-to-use PtNPs-based mercury sensor.

The method consists of two stages. First, mercury ions are quantitatively reduced using a weak reducing agent, like ascorbic acid (AA), leading to elemental mercury

that nucleates on the nanoparticle surface (nucleation step). Subsequently, residual free PtNP surface is evaluated by monitoring the TMB oxidation in the presence H_2O_2, according to the reaction reported in the **Figure 4.3**.

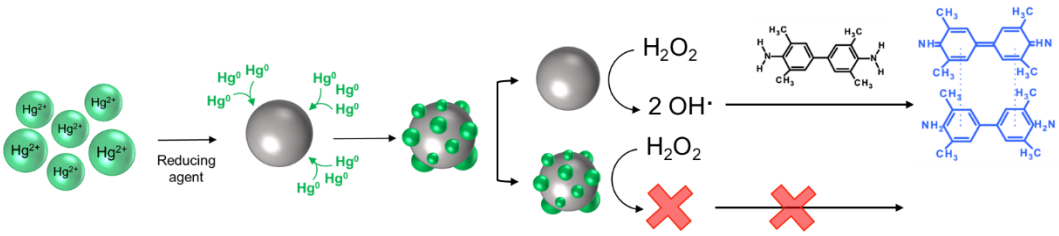

Figure 4.3 Pt-NPs based method for the mercury detection.

4.2 Materials and methods

4.2.1 Synthesis of spherical 5 nm PtNPs

Citrate-capped PtNPs with a diameter of 5 nm (Pt5) were synthesized by direct nucleation. 160 µL of 0.5 M H_2PtCl_6 were dissolved in 79.65 mL of double distilled water together with 192 µL of 0.5 M sodium citrate. 5.4 mL of a solution 0.06 M of $NaBH_4$ were added by slow dropwise, under vigorous stirring. To remove the excess of reducing agent, the temperature was then raised to 75 °C. After 30 minutes, the solution was cooled to room temperature and washed with 2 mM sodium citrate solution using 10K Centrifugal Filters, and stored under 4 °C.

4.2.2 Synthesis of flower-like 20 nm PtNPs

Citrate-capped PtNPs with a diameter of 20 nm were synthesized by a seed-growth method[26], starting from 3 nm seeds prepared by the procedure reported by Bigall *et al*[42]. 3mL of this solution were added to 150 mL of double distilled water, under stirring, together with 216 µL of 0.5 M H_2PtCl_6. Subsequently, 1.5 mL of a solution

containing 1.25% (m/v) sodium citrate and 1% (m/v) L-ascorbic acid were added and the temperature was gradually raised (~ 5 °C/min) to the boiling point. The reaction was conducted at reflux (~ 100 °C) for 1 h. After being cooled at room temperature, the solution was washed with 2 mM citrate solution using 50K centrifuge filters to remove any contaminant.

4.2.3 TEM imaging

The TEM analysis was performed using a JEOL JEM 1400 microscope. Samples were prepared drop casting 3 µL of each solution on oxygen plasma cleaned grid (CF150-Cu-50 - Carbon Film 150 Mesh, Cu, 50/bx) and vacuum drying.

4.2.4 UV-visible spectroscopy

UV-vis spectra (400-800 nm) of the nanoparticle suspension were acquired by a Thermo Fisher NanoDrop® (wavelength Accuracy ± 1 nm, absorbance accuracy 3 % at 0.74 Abs@350nm) with a small volume cuvette. PtNPs were incubated with positive samples obtained by adding a spike of a standard mercury solution in tap water. After the nucleation step, the detection mix was added and the TMB oxidation reaction was monitored by spectrophotometric kinetic reading. Briefly, 5.0 µL of 200 mM citric acid/sodium citrate buffer solution (pH 5.0) were added to 80 µL of mercury spiked water followed by 1 µL of Pt20 (125 pM in 2 mM trisodium citrate) or 5 µL of Pt5 (5 nM in 2 mM trisodium citrate) and 1 µL of 5 mM ascorbic acid solution. After 5 minutes of incubation, 20 µL of 500 mM TMB and 20 µL of 1M H_2O_2 were added and the solution color change was registered.

4.2.5 X-ray Photoelectron Spectroscopy (XPS)

The XPS analyses were carried out with a Kratos Axis Ultra spectrometer. The sample for XPS characterization was prepared by drop casting a few microliters of a 200-fold concentrated solution of PtNPs (after incubation) on a freshly cleaved highly oriented pyrolytic graphite (HOPG) substrate (NT-MDT, ZYB). Spectra were analyzed using CasaXPS software (version 2.3.17).

4.3 Results

4.3.1 PtNPs characterization

Two sets of PtNPs have been tested to compare the behaviour of 20 nm flower-like PtNPs and 5 nm spherical PtNPs. After the synthesis bot 5 and 20 nm PtNPs have been characterized in terms of size acquiring TEM images (see Fi**gure 4.4** and **Figure 4.5**).

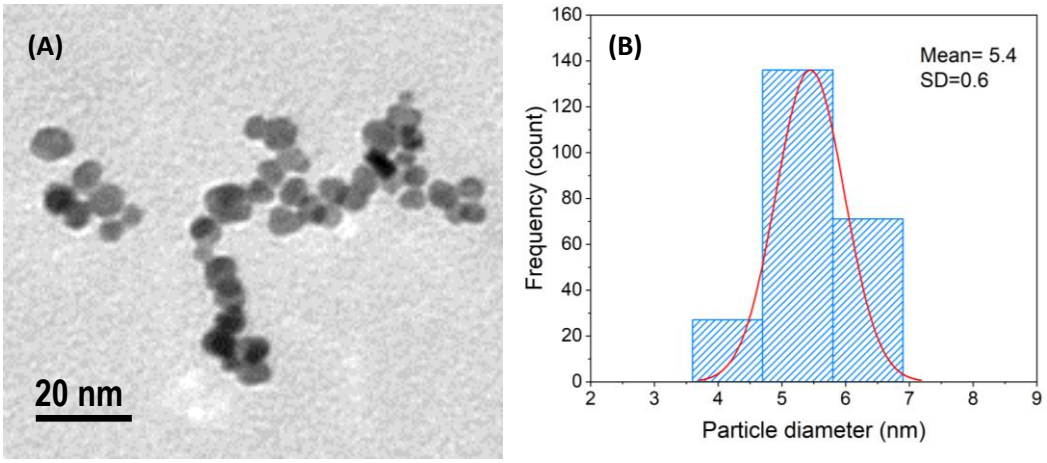

Figure 4.4 (A) Representative TEM micrograph and **(B)** size distribution analysis of spherical 5 nm PtNPs.

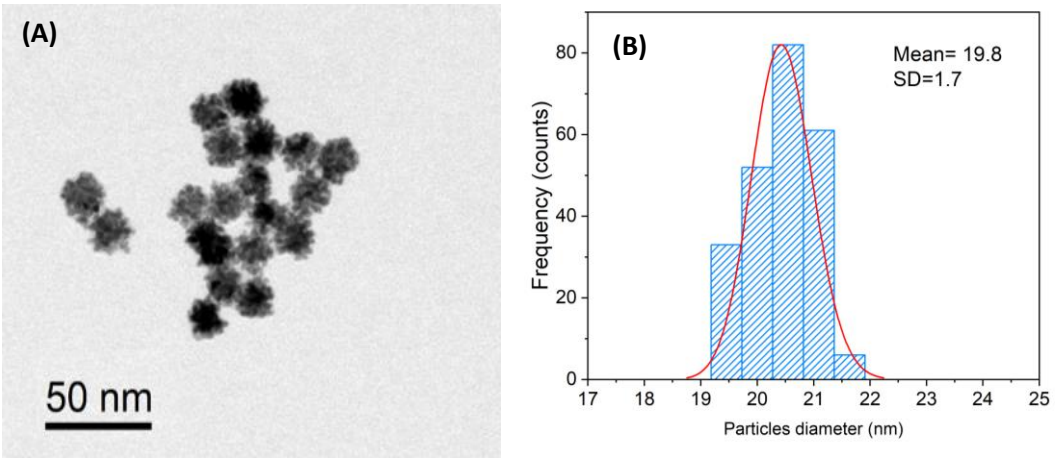

Figure 4.5 (A) Representative TEM micrograph and **(B)** size distribution analysis of flower-like 20 nm PtNPs.

The performance of the nanosensor is closely related to the ability to control the surface passivation with metallic mercury. Considering the first step of the sensing strategy as a heterogeneous nucleation, modulating the PtNPs shape and diameter, whole mercury shell can be obtained even in case of low Hg^{2+} concentrations. Our results show that 5 nm PtNPs allows a high yield amalgam formation which translates in higher sensitivity of the method. **Figure 4.6** shows the comparison between 5nm PtNPs and 20 nm PtNPs in terms of residual peroxidase-like activity after incubation with water sample containing Hg^{2+} 100 nM. 5 nm PtNPs report higher surface passivation, paired the analyte concentration the small slide surface favour the nucleation of the mercury ions, resulting in a lower Limit-Of-Detection.

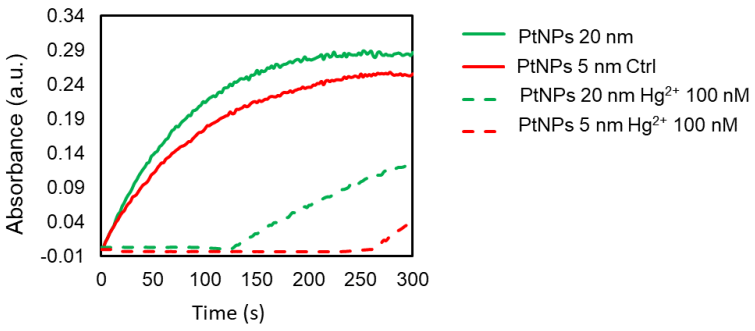

Figure 4.6 comparison of residual catalytic activity between spherical 5nm PtNPs and flower-like 20 nm PtNPs after incubation with Hg^{2+} 100 nM. The solid surface of spherical PtNPs allows quantitative nucleation of mercury ions.

4.3.2 Reducing agent optimization

Since the residual catalytic NP surface is inversely proportional to the Hg^{2+} content within the sample, a quantitative assessment can be achieved by modulating the reduction of mercury to the elemental form and the amalgam reaction. The method selectivity relies on the Hg^{2+} high Red-Ox potential (E°= 0.85) that makes it capable to react even in the presence of weak reducing agents. AA has been chosen to help the mercury reaction (E°= 0.39), whilst it cannot reduce the other cations naturally occurring in fresh water (K^+, Na^+, Ca^{2+}, Fe^{2+}, Cr^{3+} etc.), due to their lower redox potentials. However, AA concentration has been finely tuned, as it competes with TMB in the reaction with OH•, causing the delay of the TMB catalysed chromogenic reaction. We tested different concentrations of AA to obtain a suitable delay for ON/OFF colorimetric output of the sensor (see **Figure 4.7**).

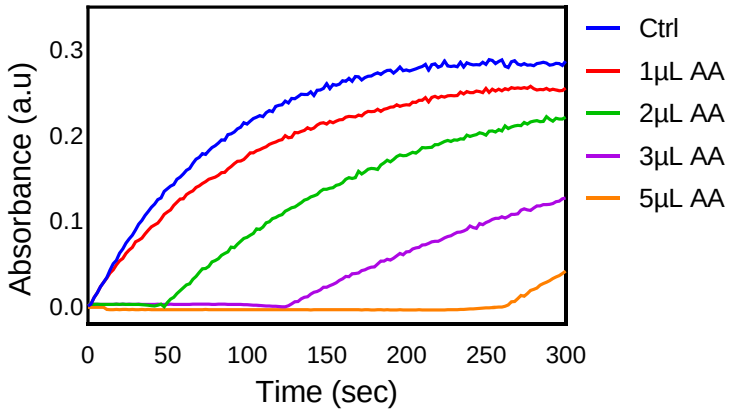

Figure 4.7 Tuning of the delay caused by increasing amounts of 5 mM AA solution.

Alternative reducing agents, namely oxalic acid and formic acid, have been tested with the aim to obtain a complete mercury reduction in short time. **Figure 4.8** shows promising preliminary data in the presence of oxalic acid. A 100 nM concentration of Hg^{2+} can be detected without any delay typical of the AA interference on the TMB oxidation.

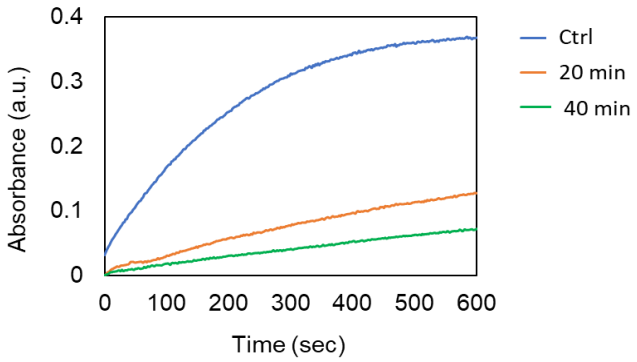

Figure 4.8 Reduction using Oxalic acid as reducing agent: in 20 min, a significant PtNPs surface passivation occurs in the presence of a 100 nM Hg^{2+} spiked sample. Moreover, any delay of the TMB oxidation was observed.

4.3.3 Incubation step optimization

To improve the sensitivity of the method, also the incubation time was characterized with the aim to determine the minimum time required for effective nucleation. Four mercury spiked water samples (25nM-100nM) were incubated with PtNPs and AA, and the residual peroxidase-like activity of the nanomaterial was evaluated at different time-points (see **Figure 4.9**).

Higher incubation times resulted in higher sensitivity of the sensor. Figure 7C shows that a sample containing 50 nM Hg^{2+} could be detected after 30 minutes of incubation, whilst 12 hours of incubations are needed for detecting a sample containing 25 nM Hg^{2+} (see **Figure 4.9 D**). The Limit-Of-Detection (LOD) for a fast incubation method (5 min) results to be 80 nM.

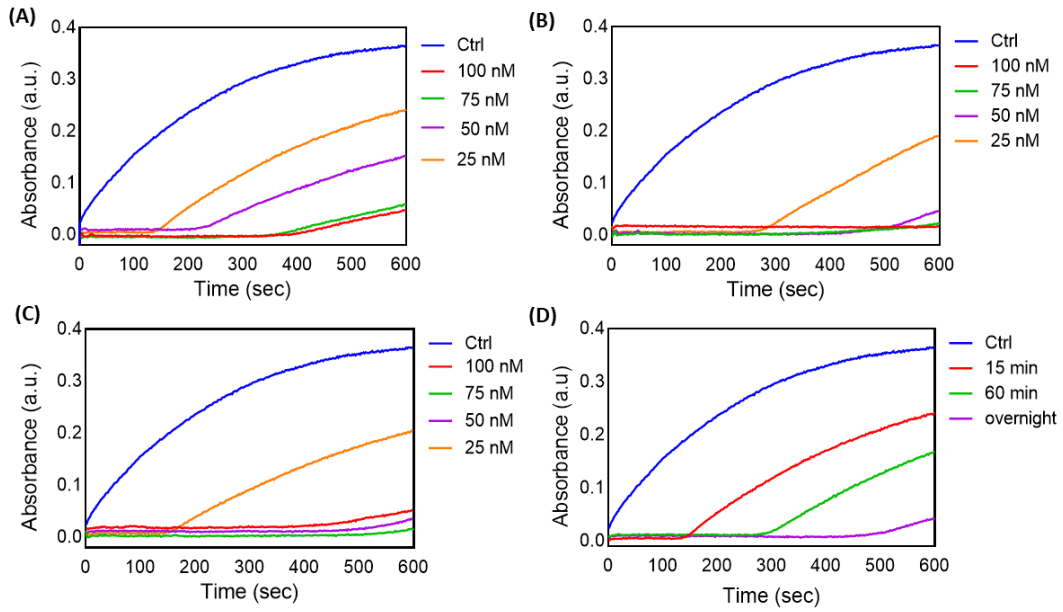

Figure 4.9 Peroxidase-like activity of PtNPs incubated with different concentrations of Hg^{2+} (100-75-50-25 nM). The TMB oxidation reaction was recorded after several incubation times: 5 min **(A)**, 15 min **(B)**, and 30 min **(C)**. Increasing the incubation time (>60 min), 25 nM Hg^{2+} can be detected with remarkable NP surface passivation **(D).**

4.3.4 Incubation step optimization

To characterize the amalgam formation during the nucleation step of the method, TEM images of 5 nm PtNPs were acquired before and after the reaction with Hg^{2+} and AA (**Figure 4.10 A, B**). NPs polydispersity increase points out the nucleation of metallic mercury on the particles surface. XPS analysis was performed on PtNPs after the incubation with water samples spiked up to 50 nM Hg^{2+} (PD 10,11) and 100 nM Hg^{2+} (PD12,13), confirming the efficiency of the reducing agent on the mercury amalgam formation **Figure 4.10 C**). Optimizing the nucleation reaction as well as the TMB oxidation, a LOD of 80 nM was obtained for the detection of Hg^{2+} in real tap water. In 5 minutes, the amalgam formation on PtNPs allows a perfect ON/OFF read out of the results in which the negative sample has a vivid blue colour while the positive sample remains colourless (see **Figure 4.10 D**).

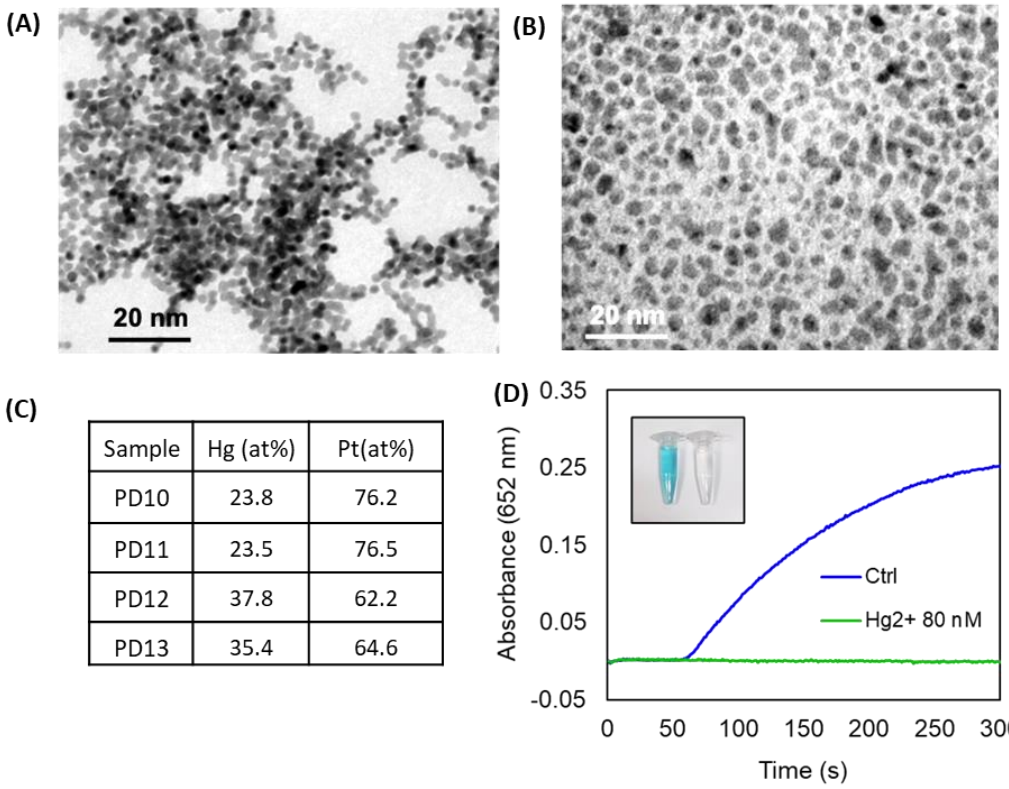

Sample	Hg (at%)	Pt(at%)
PD10	23.8	76.2
PD11	23.5	76.5
PD12	37.8	62.2
PD13	35.4	64.6

Figure 4.10 (A) TEM images of 5 nm PtNPs before **(A)** and after **(B)** 5 minutes of incubation with water sample containing 100 nM Hg^{2+}. **(C)** XPs results in terms of Hg (at%) and Pt (at%) for samples containing 50 nM Hg^{2+} (PD10,11) and 100 nM Hg^{2+} (PD12,13), respectively **(D).** Time-dependent absorbance signals at 652 nm of TMB after incubation with H_2O_2 and PtNPs for a negative (Ctrl) and positive (Hg^{2+} 80 nM) sample with remarkable colorimetric ON/OFF result.

In order to stabilize PtNPs in complex media, as sea water or food extracts, various strategies have been tested. To avoid the PtNPs precipitation during the assay, we adsorbed the nanomaterial on different particles as support. Commercial products, like AEROSIL® 150 (hydrophilic fumed silica) and 60 nm diameter Silica nanoparticles, are able to efficiently stabilize small nanoparticles in solution, proved dosing the catalytic activity, (see **Figure 4.11 A**, **B**). To validate this approach, the PtNPs catalytic activity was characterized before the NPs absorption on silica nanoparticles, as well as before and after the lyophilization procedure (see **Figure 4.11 C**). However, we observed a reduction in the method sensitivity in the presence of the nanosized support, due to the difficult of mercury ions to reach the particles.

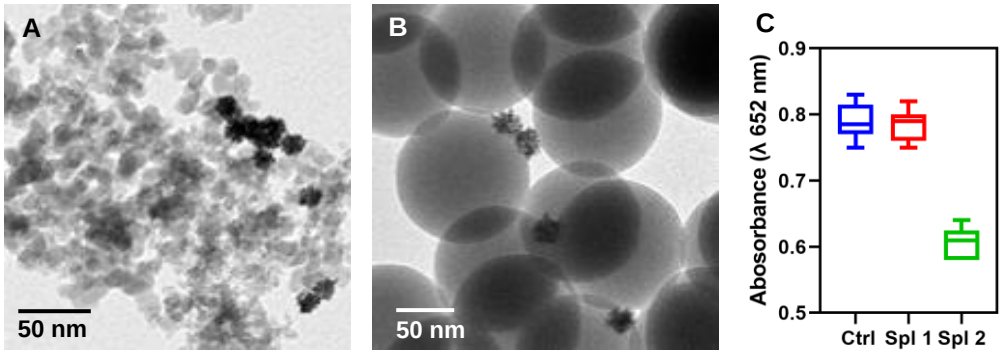

Figure 4.11 TEM images showing the results of PtNPs stabilization on different supports. **(A)** Lyophilized PtNPs supported on AREOSIL 150 after resuspension in water. **(B)** Silica NPs as support for 20 nm PtNPs. **(C)** Peroxidase-like activity comparison between citrate capped-PtNPs and PtNPs stabilized on Silica NPs as support, before (blue) and after (red) the lyophilization, and once resuspended (green).

An interesting approach to increase PtNPs stability involves the use of polymers, such as Polyvinylpyrrolidone (PVP) and Poly (acrylic acid). According to these data, we observed that PVP coated-PtNPs can be stored as lyophilized powder and directly resuspended during the assay (see **Figure 4.12**).

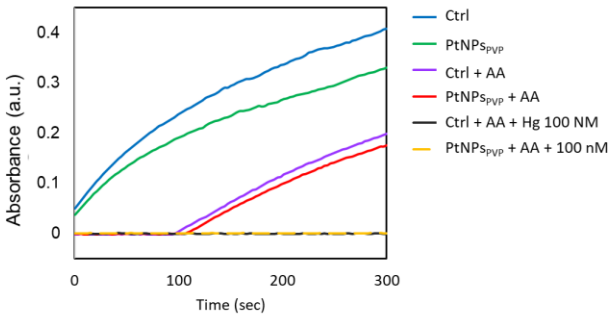

Figure 4.12 Comparison between citrate- and PVP-capped PtNPs: the polymer does not affect the nanoparticle surface reactivity allowing the same sensitivity of "naked" nanoparticles in the presence of a 100 nM Hg^{2+} spiked sample.

4.4 Conclusions

In this work, we explored the use of PtNPs as nanozymes in surface passivation-based colorimetric method for mercury ions detection in water samples. We reported easy and fast assay that in less than 10 minutes give out a remarkable colour change that allows the naked eye ON/OFF colorimetric assessment of mercury contaminations. This nanosensor shows some relevant optimizations compared to the other approaches previously published, as the use of stabilized PtNPs that enables the assessment of mercury contaminations in real samples. Moreover, tuning the incubation time and using different reducing agents, such as oxalic acid, the analytical utility of this method can be implemented. Considering the method features, this nanosensor can be easily transferred to solid based micro-Pads or lateral flow based devices for effective home testing solutions.

4.5 Bibliography

1. Liu, Y., Li, D. & Sun, S. Pt-based composite nanoparticles for magnetic, catalytic, and biomedical applications. *J. Mater. Chem.* **21**, 12579–12587 (2011).

2. Pedone, D., Moglianetti, M., De Luca, E., Bardi, G. & Pompa, P. P. Platinum nanoparticles in nanobiomedicine. *Chemical Society Reviews* **46**, 4951–4975 (2017).

3. Chen, A. & Holt-Hindle, P. Platinum-based nanostructured materials: Synthesis, properties, and applications. *Chem. Rev.* **110**, 3767–3804 (2010).

4. Zhang, Q. *et al.* Surfactant-Free Synthesis of Ultrafine Pt Nanoparticles on MoS2Nanosheets as Bifunctional Catalysts for the Hydrodeoxygenation of Bio-Oil. *Langmuir* **36**, 14710–14716 (2020).

5. Rizo, R. & Roldan Cuenya, B. Shape-Controlled Nanoparticles as Anodic Catalysts in Low-Temperature Fuel Cells. *ACS Energy Letters* **4**, 1484–1495 (2019).

6. Wang, H. & Lu, J. A Review on Particle Size Effect in <scp>Metal-Catalyzed</scp> Heterogeneous Reactions. *Chinese J. Chem.* **38**, 1422–1444 (2020).

7. Duan, S., Du, Z., Fan, H. & Wang, R. Nanostructure optimization of platinum-based nanomaterials for catalytic applications. *Nanomaterials* **8**, 949 (2018).

8. McNamara, K. & Tofail, S. A. M. Nanoparticles in biomedical applications. *Advances in Physics: X* **2**, 54–88 (2017).

9. Yang, Y. *et al.* Ultrasound assisted one-step synthesis of Au@Pt dendritic nanoparticles with enhanced NIR absorption for photothermal cancer therapy. *RSC Adv.* **9**, 28541–28547 (2019).

10. Samadi, A. *et al.* Platinum nanoparticles: A non-toxic, effective and thermally stable alternative plasmonic material for cancer therapy and bioengineering. *Nanoscale* **10**, 9097–9107 (2018).

11. Ayaz Ahmed, K. B., Raman, T. & Anbazhagan, V. Platinum nanoparticles inhibit bacteria proliferation and rescue zebrafish from bacterial infection. *RSC Adv.* **6**, 44415–44424 (2016).

12. Hamasaki, T. *et al.* Kinetic analysis of superoxide anion radical-scavenging and hydroxyl radical-scavenging activities of platinum nanoparticles. *Langmuir* **24**, 7354–7364 (2008).

13. Ji, H. *et al.* Bacterial Hyaluronidase Self-Triggered Prodrug Release for Chemo-Photothermal Synergistic Treatment of Bacterial Infection. *Small* **12**, 6200–6206 (2016).

14. Au, L. *et al.* A quantitative study on the photothermal effect of immuno gold nanocages targeted to breast cancer cells. *ACS Nano* **2**, 1645–1652 (2008).

15. Draz, M. S. *et al.* Virus detection using nanoparticles and deep neural network-enabled smartphone system. *Sci. Adv.* **6**, 5354–5370 (2020).

16. Manea, F., Houillon, F. B., Pasquato, L. & Scrimin, P. Nanozymes: Gold-nanoparticle-based transphosphorylation catalysts. *Angew. Chemie - Int. Ed.* **43**, 6165–6169 (2004).

17. Wang, X., Hu, Y. & Wei, H. Nanozymes in bionanotechnology: From sensing to therapeutics and beyond. *Inorg. Chem. Front.* **3**, 41–60 (2016).

18. Shin, H. Y., Park, T. J. & Kim, M. Il. Recent Research Trends and Future Prospects in Nanozymes. *J. Nanomater.* **2015**, (2015).

19. Wang, Q., Wei, H., Zhang, Z., Wang, E. & Dong, S. Nanozyme: An emerging alternative to natural enzyme for biosensing and immunoassay. *TrAC - Trends in Analytical Chemistry* **105**, 218–224 (2018).

20. Wei, H. & Wang, E. Nanomaterials with enzyme-like characteristics (nanozymes): Next-generation artificial enzymes. *Chem. Soc. Rev.* **42**, 6060–6093 (2013).

21. Wang, X., Guo, W., Hu, Y., Wu, J. & Wei, H. *Nanozymes: Next Wave of Artificial Enzymes*. (Springer Berlin Heidelberg, 2016). doi:10.1007/978-3-662-53068-9

22. Kajita, M. *et al.* Platinum nanoparticle is a useful scavenger of superoxide anion and hydrogen peroxide. *Free Radic. Res.* **41**, 615–626 (2007).

23. Cui, Y. *et al.* Polyethyleneimine-Stabilized Platinum Nanoparticles as Peroxidase Mimic for Colorimetric Detection of Glucose. *ACS Omega* **5**, 6800–6808 (2020).

24. Li, J. *et al.* Core-shell Fructus Broussonetia-like Au@Ag@Pt nanoparticles as highly efficient peroxidase mimetics for supersensitive resonance-enhanced Raman sensing. *Anal. Methods* **8**, 2097–2105 (2016).

25. Ye, H., Liu, Y., Chhabra, A., Lilla, E. & Xia, X. Polyvinylpyrrolidone (PVP)-capped Pt nanocubes with superior peroxidase-like activity. *ChemNanoMat* **3**, 33–38 (2017).

26. Moglianetti, M. *et al.* Platinum nanozymes recover cellular ROS homeostasis in an oxidative stress-mediated disease model. *Nanoscale* **8**, 3739–3752 (2016).

27. Chang, H. *et al.* Pt NPs and DNAzyme functionalized polymer nanospheres as triple signal amplification strategy for highly sensitive electrochemical immunosensor of tumour marker. *Biosens. Bioelectron.* **86**, 156–163 (2016).

28. Kwon, D. *et al.* Colorimetric detection of penicillin antibiotic residues in pork using hybrid magnetic nanoparticles and penicillin class-selective, antibody-functionalized platinum nanoparticles. *Anal. Methods* **7**, 7639–7645 (2015).

29. Gao, Z., Xu, M., Hou, L., Chen, G. & Tang, D. Irregular-shaped platinum nanoparticles as peroxidase mimics for highly efficient colorimetric immunoassay. *Anal. Chim. Acta* **776**, 79–86 (2013).

30. He, S.-B. *et al.* Choline and acetylcholine detection based on peroxidase-like activity and protein antifouling property of platinum nanoparticles in bovine serum albumin scaffold. *Biosens. Bioelectron.* **62**, 331–336 (2014).

31. Farina, M., Aschner, M. & Rocha, J. B. T. Oxidative stress in MeHg-induced neurotoxicity. *Toxicol. Appl. Pharmacol.* **256**, 405–417 (2011).

32. Cuenya, B. R. Metal nanoparticle catalysts beginning to shape-up. *Acc. Chem. Res.* **46**, 1682–1691 (2013).

33. Peng, Z. & Yang, H. Designer platinum nanoparticles: Control of shape, composition in alloy, nanostructure and electrocatalytic property. *Nano Today* **4**, 143–164 (2009).

34. Narayanan, R. & El-Sayed, M. A. Shape-dependent catalytic activity of platinum nanoparticles in colloidal solution. *Nano Lett.* **4**, 1343–1348 (2004).

35. Fan, J. *et al.* Direct evidence for catalase and peroxidase activities of ferritin-platinum nanoparticles. *Biomaterials* **32**, 1611–1618 (2011).

36. Malekzad, H., Sahandi Zangabad, P., Mirshekari, H., Karimi, M. & Hamblin, M. R. Noble metal nanoparticles in biosensors: Recent studies and applications. *Nanotechnology Reviews* **6**, 301–329 (2017).

37. Kim, M. Il *et al.* Highly efficient colorimetric detection of target cancer cells utilizing superior catalytic activity of graphene oxide-magnetic-platinum nanohybrids. *Nanoscale*

6, 1529–1536 (2014).

38. Palladino, P., Torrini, F., Scarano, S. & Minunni, M. 3,3’,5,5’-tetramethylbenzidine as multi-colorimetric indicator of chlorine in water in line with health guideline values. *Anal. Bioanal. Chem.* **412**, 7861–7869 (2020).

39. Josephy, P. D., Eling, T. & Mason, R. P. The horseradish peroxidase-catalyzed oxidation of 3,5,3’,5’-tetramethylbenzidine. Free radical and charge-transfer complex intermediates. *J. Biol. Chem.* **257**, 3669–3675 (1982).

40. Bönnemann, H. & Richards, R. M. Nanoscopic Metal Particles − Synthetic Methods and Potential Applications. *Eur. J. Inorg. Chem.* **2001**, 2455–2480 (2001).

41. Song, H., Kim, F., Connor, S., Somorjai, G. A. & Yang, P. Pt nanocrystals: Shape control and Langmuir-Blodgett monolayer formation. *J. Phys. Chem. B* **109**, 188–193 (2005).

42. Bigall, N. C. *et al.* Monodisperse platinum nanospheres with adjustable diameters from 10 to 100 nm: Synthesis and distinct optical properties. *Nano Lett.* **8**, 4588–4592 (2008).

43. Adil, S. F. *et al.* Biogenic synthesis of metallic nanoparticles and prospects toward green chemistry. *Dalt. Trans.* **44**, 9709–9717 (2015).

44. Hasan, A. *et al.* Nanozyme-based sensing platforms for detection of toxic mercury ions: An alternative approach to conventional methods. *Talanta* **215**, 120939 (2020).

45. Salonen, J. T. *et al.* Intake of mercury from fish, lipid peroxidation, and the risk of myocardial infarction and coronary, cardiovascular, and any death in Eastern Finnish men. *Circulation* **91**, 645–655 (1995).

46. Rizzetti, D. A. *et al.* Egg white hydrolysate promotes neuroprotection for neuropathic disorders induced by chronic exposure to low concentrations of mercury. *Brain Res.* **1646**, 482–489 (2016).

47. Habte, G. *et al.* Elemental profiling and geographical differentiation of Ethiopian coffee samples through inductively coupled plasma-optical emission spectroscopy (ICP-OES), ICP-mass spectrometry (ICP-MS) and direct mercury analyzer (DMA). *Food Chem.* **212**, 512–520 (2016).

48. Tchounwou, P. B., Yedjou, C. G., Patlolla, A. K. & Sutton, D. J. Heavy Metals Toxicity and the Environment. *EXS* **101**, 133–164 (2012).

49. Nutrition, C. for F. S. and A. Metals - Mercury and Methylmercury.

5 Conclusions

Point-Of-Care testing is strongly improving quality-of-life, providing new diagnostic solutions for both healthcare systems and environmental control. In this framework, this project has been centred on the development of three nanoparticles-based sensors for the easy and rapid assessment of analytes of biomedical and environmental interest, taking advantage of enzymatic and plasmonic nanoparticles properties.

The first aim of this work has been the development of a self-catalysed plasmonic platform for the methyl mercury detection in organic samples, such as human urine and food extracts. Mercury, as well as other heavy metal ions, is ranked in the top ten list of hazardous substances, due to its toxic effects on both human and environmental health. To date, the mercury assessment is sporadic, as the tests are laborious and expensive. The proposed nanosensor combine catalytic and plasmonic properties of gold nanoparticles to achieve fast organic mercury detection with high sensitivity. To the best of our knowledge, this technique represents the first easy-to-use platform for the detection of organic mercury in biological fluids and food extracts, as a marker of mercury intoxication and contaminations.

Furthermore, plasmonic properties applications are not limited to classical aggregation-based colorimetric methods. Gold nanoparticles size and shape can be finely manipulated in a new class of sensors that respond to external stimuli, as the analytes, leading to a colorimetric outcome.

Therefore, as second aim of this work, the surface reshaping process of gold multibranched nanoparticles has been exploited to develop a customizable method for glucose measurement in saliva. Combining the target enzymatic conversion and the gold nanoparticles reshaping in a boosted color change outcome, a new and effective nanobiosensor for the salivary glucose assessment, with micromolar sensitivity, has been developed. This nanoparticle-based

technology has been successfully transferred into an integrated μ-Pad and applied for the fast ad non-invasive salivary glucose assessment in real diabetic patient samples. The obtained results show that this innovative platform represents a valid alternative to the invasive, and eventually painful, blood tests.

In the last part of this work, I have reported an enzymatic method based on platinum nanoparticles for the measurement of the mercury content in water samples. The sensor relies on the reduce mercury amalgam formation on the particles surface and its subsequent colorimetric quantification, providing a simple and rapid (10 minutes) method for instrument-free water mercury assessment.

In conclusion, during my thesis work, I have explored the peculiar properties of gold and platinum nanoparticles to develop a set of nanobiosensors, in order to overcome the drawbacks of traditional diagnostic techniques. Providing solutions for real applications, these Point-Of-Care devices will be soon a market reality, as new approaches to portable diagnostics.

6 List of publications

- Citrate-Coated, Size-Tunable Octahedral Platinum Nanocrystals: A Novel Route for Advanced Electrocatalysts

  Mauro Moglianetti*, José Solla-Gullón*, Paolo Donati, Deborah Pedone, Doriana Debellis, Teresa Sibillano, Rosaria Brescia, Cinzia Giannini, Vicente Montiel, Juan M. Feliu, and Pier Paolo Pompa *ACS Appl. Mater. Interfaces 2018, 10, 48, 41608–41617*
  https://doi.org/10.1021/acsami.8b11774

- Nanocatalyst/Nanoplasmon-Enabled Detection of Organic Mercury: A One-Minute Visual Test

  P. Donati, M. Moglianetti, M. Veronesi, M. Prato, G. Tatulli, T. Bandiera, P. P. Pompa, Angew. Chem. Int. Ed. 2019, 58, 10285.
  https://doi.org/10.1002/anie.201905669

- Colorimetric Nanoplasmonics to Spot Hyperglycemia From Saliva

  Paolo Donati†, Tania Pomili†, Luca Boselli* and Pier P. Pompa*
  Front. Bioeng. Biotechnol., 07 December 2020
  https://doi.org/10.3389/fbioe.2020.601216

7 List of figures

8 Declaration

All the work in this thesis is my own. Wherever contributions of others are involved, every effort is made to indicate this clearly, with due reference to the literature. The work was done under the guidance of Dr. Pier Paolo Pompa at Center for Convergent Technologies of Istituto Italiano di Tecnologia.

Acknowledgement

I would like to express my gratitude to my mentor Pier Paolo Pompa for guiding and supporting me in these three years with patience and enthusiasm, encouraging me to be professional. A special thanks goes to all my colleagues. In particular, I need to express my gratitude to Deborah, Giuseppina and Tania for their efforts and their contributions on this thesis work. My deepest appreciation goes to Giulia and Valentina, with whom we started this journey, for the joy with which we worked we shared working together. I would also like to extend my thankfulness to Mauro, for the support and the illuminating opinions, we all need to be inspired sometimes. My deepest appreciation goes to Sara, for her support, her help and her patience.

My heartfelt thanks to my family, my parents Lucio and Paola and my sister, Laura. I wouldn't have made it on my own. They have always watched over me, giving me all the possible love and support.

Paolo Donati
February 14, 2021